

El Niño Diversity and its Impacts on East Asian Rainfall in the Future Climate

WANG, Peng

A Thesis Submitted in Partial Fulfillment
of the Requirements for the Degree of
Doctor of Philosophy
in
Earth and Atmospheric Sciences

The Chinese University of Hong Kong
September 2019

Thesis Assessment Committee

Professor LEE Shing Yip (Chair)

Professor TAM Chi Yung Francis (Thesis Supervisor)

Professor LAU Ngar Cheung Gabriel (Committee Member)

Dr. ZHOU Wen (External Examiner)

Abstract

The East Asian (EA) region, home to more than a billion people, is particularly vulnerable to hydrological extremes, due to its large population as well as rapid economic developments in recent decades. El Niño-Southern Oscillation (ENSO) is widely recognized as the most important driver of EA rainfall variations on the interannual timescale. This study investigates El Niño diversity and its impacts on EA rainfall in the present and future climate, using historical and representative concentration pathway 8.5 (RCP8.5) simulations from state-of-the-art models participating in phase 5 of the Coupled Model Intercomparison Project (CMIP5). Out of the 31 CMIP5 models examined, 17 of them are found to be able to well reproduce El Niño diversity. While all of the 17 models can give realistic eastern-Pacific (EP) El Niño-related Walker circulation anomalies, about one-third of them give erroneous central-Pacific (CP) El Niño-related anomalous Walker cells in the simulated environment. Further inspection reveals that these models tend to have strong cold biases of sea surface temperature (SST) over central-eastern Pacific, leading to a westward displacement of anomalous rising motion during CP El Niño. Overall, models with realistic Walker cell anomalies tend to simulate better El Niño's impact on EA low-level flow and rainfall, especially for CP El Niño.

Comparing the historical and RCP8.5 scenario simulations based on selected models which capture well both El Niño diversity and East Asian Summer Monsoon (EASM), the ENSO-related EA rainfall variability in the future climate is studied. Under global warming, EA rainfall anomalies due to two types of ENSO are projected to be intensified significantly in boreal winter at the peak of El Niño, and the ensuing summer. To better understand the underlying physical processes, moisture budget analyses are carried out. Change of El Niño-induced moisture flux convergence/divergence, which largely coincide with anomalous

rainfall changes, are dominated by the dynamic term (i.e. El Niño-induced circulation acting on time-mean moisture). A moister atmosphere under global warming tends to enhance the moisture flux, while weakened or strengthened El Niño-related circulation can play a negative or positive role in modulating moisture flux during different El Niño phases. Importantly, the effect due to mean moisture enhancement can offset (strengthen) the negative (positive) contribution of weaker (stronger) El Niño-related circulation, leading to the intensification of rainfall variations. Inspections of the individual models reveal no consensus on El Niño SSTA and its corresponding circulation changes in the future climate. However, low-level circulation changes are largely determined by the El Niño SSTA changes in terms of their intensity and location. In general, CP El Niño-related rainfall will be enhanced robustly under global warming, regardless of the change of CP-type SSTA for a particular model. For EP El Niño, its related rainfall also tends to be intensified, except for models in which EP-type SSTA is greatly weakened.

A series of atmospheric general circulation model (AGCM) experiments, with various states of the climatological SST, CO₂ concentration, as well as SSTA patterns, are carried out. Results based on these experiments also point to more variable El Niño-driven rainfall under global warming. However, due to the modulated mean background convection, the anomalous rainfall is displaced slightly eastward over the equatorial Pacific. Moisture budget analyses indicate that the intensification of rainfall anomalies and their pattern change can be mainly attributed to the perturbed anomalous circulation. In comparison, the role of a moister atmosphere background is less important, and it only acts to intensify the original general patterns of El Niño-related rainfall. It is noticed that the warmer background climate can also accelerate anomalous wind flow. The latter effect might arise from stronger circulation response under warmer basic states even with identical El Niño SST forcing.

Finally, atmospheric feedback, thermocline feedback, net heat flux feedback during ENSO, and their changes under global warming, are examined. It is noticed that the strength of atmospheric and thermocline feedbacks from individual models are modulated in the same way for two types of ENSO, but not the case for net heat flux feedback. In fact, models that show stronger (weaker) EP El Niño also tend to give stronger (weaker) CP El Niño in the future climate. The coherency between changes of EP and CP ENSO feedback strength might explain the aforementioned relationship between changes of EP and CP El Niño intensity.

摘要

伴隨著經濟和人口的快速增長，東亞地區極易受到極端降水的影響。厄爾尼諾事件的發生是東亞降水異常的重要驅動因子。本文利用參與CMIP5評估的31個氣候模式在和RCP8.5情境下的模擬數據，研究了全球變暖背景下兩類厄爾尼諾事件對東亞地區降水的影響。經驗證，具備模擬厄爾尼諾多樣性能力的17個模式可以較好的模擬出東部型厄爾尼諾所對應的Walker環流異常。由於模式氣候態海溫存在異常偏強的東太平洋冷舌型誤差，其中六個模式給出的中部型厄爾尼諾導致的Walker環流異常則表現出顯著的西移偏差。進壹步的研究表明，具備模擬兩類厄爾尼諾引起的異常Walker環流能力的壹組模式，其多模式平均的結果能夠較好的反映出兩類厄爾尼諾與東亞氣候變異的遙相關。對於另壹組模式，它所模擬的中部型厄爾尼諾與東亞異常環流降水的關係與觀測結果存在顯著偏差。

通過評估31個模式對東亞夏季風的模擬能力，6個模式能夠較好地模擬出歷史情境下兩類厄爾尼諾異常導致的東亞氣候變異和東亞夏季風的年際變異。基於對比未來和歷史情境下的多模式平均結果，由於兩類厄爾尼諾事件所導致的東亞冬夏降水異常在全球變暖的背景下將會顯著增強。水汽收支分析結果表明，未來厄爾尼諾相關的東亞降水異常主要由水汽動力傳輸項的變化所決定。由於氣候變暖所產生的更多水汽將會增加東亞地區的異常降水，而主要由厄爾尼諾海溫異常變化所驅動的環流異常變化在不同的季節呈現微弱的增強或者減弱的趨勢，但是平均水汽的增強可以抵消環流減弱的影響，並最終導致東亞降水異常的增強。對單個模式的分析表明：盡管兩類厄爾尼諾海溫異常在全球變暖背景下的變化具有較大的模式間誤差，但是其強度和位置的變化與對應東亞/西北太平洋環流異常的強度和位置變化顯著正相關。與此同時，單個模式的

結果進一步驗證了：儘管不同模式預估未來中部型厄爾尼諾可能變弱或者變強，其所引發的東亞降水異常都將顯著增強。同樣的結果也適用於東部型厄爾尼諾，除非其強度顯著地減弱。

為了進壹步探究全球變暖背景下氣候態背景及厄爾尼諾異常海溫擾動對降水的影響，本文利用CAM4設計了AGCM數值試驗。結果表明：未來兩類厄爾尼諾事件將會顯著引起熱帶降水異常的增強。氣候變暖背景下，環流異常的變化主要導致了厄爾尼諾降水的模態增強及其位置的變化，而平均水氣的增加只能增強厄爾尼諾降水的模態。氣候變暖不僅為背景場提供了更多的水汽，還可能導致了環流異常對兩類厄爾尼諾海溫強迫的非線性響應，進而影響熱帶地區的降水。

通過對兩類厄爾尼諾事件未來變化的探究發現，模擬出未來增強（減弱）的東部型厄爾尼諾事件的模式傾向於模擬出增強（減弱）的中部型厄爾尼諾事件。兩類厄爾尼諾異常中心位置的變化也表現出壹定的協同性。與兩類ENSO事件相關的大氣海洋反饋過程在全球變暖背景下的協同變化，可能解釋了這壹現象。

Acknowledgement

I would like to take this opportunity to acknowledge my supervisor Professor Tam Chi-Yung Francis, for his generous guidance, support, motivation and endless patience. Professor Tam not only led me to the deep of atmospheric science and shared his academic knowledge, but also enlightened me with new ideas and inspired me to become an independent explorer. I really appreciate his great effort during my Ph.D. study, and this work cannot be completed without his advice and support.

More widely, I would also like to thank everyone at EASC who has taught me and helped me during the past three years. I will cherish all the days with you guys in Hong Kong. My sincere thanks also go to Professor Lee Shing Yip, Professor Lau Ngar Cheung Gabriel, and Professor Zhou Wen for reviewing this thesis. I am also grateful for the valuable suggestions from Dr. Xu Kang when I started this work. The numerical experiments carried out in this study were supported by Professor Yang Song and his Ph.D. student Ren Qiaoling; I would like to acknowledge their efforts on chapter 5.

Finally, I should thank my parents and my fiancee Wang Lin for their abiding love and support throughout, for their encouragement when I was at the low point of my life, for their eternal drive to help me reach my dream.

Table of Contents

Abstract	i
摘要.....	iv
Acknowledgement.....	vi
Table of Contents	vii
List of Figures	x
List of Tables.....	xxi
1 Introduction.....	1
1.1 Present-day ENSO and its impacts based on observations and models	1
1.1.1 ENSO and its Diversity.....	2
1.1.2 ENSO dynamics	3
1.2 East Asian summer monsoon (EASM) variability	8
1.2.1 ENSO-EA rainfall teleconnection	8
1.2.2 ENSO, EASM and their teleconnection in CMIP5 models.....	10
1.3 Future ENSO and its impacts	12
1.3.1 ENSO and its diversity under global warming.....	12
1.3.2 EASM under global warming.....	13
1.3.3 ENSO-EA rainfall teleconnection under global warming.....	16
1.4 Research questions and thesis outline.....	17
2 Data and Methodology.....	19

vii

2.1 Observational and model datasets	19
2.2 Analysis methods	20
2.2.1 Selection of El Niño events.....	20
2.2.2 EASM interannual variability evaluation.....	22
2.2.3 Diagnosing future change of El Niño-related EA rainfall anomalies	23
2.2.4 AGCM experiments.....	25
2.2.5 Ocean-atmosphere feedbacks during ENSO	25
3 El Niño-EA Climate Teleconnection and its Diversity in CMIP5 Models	
	30
3.1 Evaluation of CMIP5 models	30
3.1.1 El Niño diversity and its related overturning circulation	30
3.1.2 El Niño-related SST evolution	40
3.2 El Niño-EA monsoon teleconnection and its diversity	45
3.3 Role of tropical basic state on El Niño-EA monsoon teleconnection	53
3.4 Brief summary.....	58
4 El Niño-EA Climate Teleconnection Under Global Warming.....	60
4.1 Evaluation of EASM in CMIP5 models.....	60
4.2 Future changes of El Niño-EA rainfall teleconnection.....	68
4.3 Moisture budget analyses.....	81
4.4 Brief summary.....	93
5 El Niño-Related Precipitation Under Global Warming Based on AGCM Experiments	95

5.1 AGCM experiment design.....	95
5.2 Results.....	102
5.2.1 Comparison between Control_future and Control_present simulations	102
5.2.2 Future changes of El Niño-related rainfall in AGCM runs	105
5.2.3 Moisture budget analyses.....	111
5.3 Brief summary.....	119
6 El Niño Changes Under Global Warming: Role of Ocean-Atmosphere Feedback.....	120
6.1 Relationship between EP and CP El Niño changes	120
6.2 El Niño-related ocean-atmosphere feedback changes in the future climate..	122
7 Conclusion and Discussion.....	135
7.1 Performance of CMIP5 models in simulating present-day El Niño-EA rainfall teleconnection and its diversity.....	135
7.2 El Niño-EA rainfall teleconnection and its diversity in a warmer climate....	137
7.3 Physical processes responsible for the two types of El Niño-related rainfall changes under global warming.....	139
7.4 Modulation of two types of El Niño due to global warming.....	144
Appendix	I
Bibliography.....	VII

List of Figures

Figure 1.1 First and second leading modes (empirical orthogonal functions) of SST variability corresponding to (a) EP and (b) CP El Niño in the tropical Pacific based on observations taken from Xu et al (2017).....	3
Figure 1.2 Schematic diagrams representing the tropical Pacific and Walker circulation under (a) neutral, (b) EP El Niño and (c) CP El Niño conditions. Warmer and cooler sea surface temperatures are described by red and blue shading (See text in Section 1.1.2 for more details).	7
Figure 1.3 Schematic diagram illustrating the main ways that human activity influences monsoon rainfall as the climate warms (see text in section 1.2.2 for more details). From Christensen et al. (2013).....	15
Figure 2.1 Multi-model ensemble (MME) mean of tropical Pacific SST anomalies associated with (a, c) EP and (b, d) CP El Niño (units: K) calculated from (a, b) the historical runs during the 1950-1999 period, and (c, d) RCP8.5 runs during the 2050-2099 period based on 17 selected CMIP5 models. SST maps (units: K) corresponding to EP and CP El Niño are computed by regressing SST anomalies onto the EP and CP El Niño-related principal components, respectively. From Xu et al. (2017).	22
Figure 3.1 EOF patterns of the interannual SST anomalies (see scale bar at bottom; units: K) corresponding to EP El Niño based on observations and each of the 17 selected CMIP5 coupled models. Patterns are computed by regressing SST anomalies onto the corresponding principal components.	31
Figure 3.2 EOF patterns of the interannual SST anomalies (see scale bar at bottom; units: K) corresponding to CP El Niño based on observations and each of the 17 selected CMIP5	

coupled models. Patterns are computed by regressing SST anomalies onto the corresponding principal components. 32

Figure 3.3 Composite of 5°N–5°S NDJFM averaged zonal divergent wind and pressure velocity (vectors; see scale arrow at bottom right) for EP El Niño based on observations and each of the 17 selected CMIP5 coupled models. Shadings denote anomalous pressure velocity (see scale bar at bottom; units: Pa/s), which is multiplied by a factor of -100 for clarity. 34

Figure 3.4 Same as **Figure 3.3**, but for CP El Niño. 35

Figure 3.5 Scatter plot of longitudinal locations of the centroid of ascending motion associated with CP and EP El Niño overturning circulation, for observations and the 17 selected CMIP5 models, as well as their probability distribution function based on kernel density estimation for CP (top inset) and EP (right inset) El Niño. The vertical dashed line indicates the 130°E longitude demarcating the two model groups. See text for details. 37

Figure 3.6 (a, c) Same as **Figure 3.3**, but for MME mean based on models in (a) group A and (c) group B. (b, d) Same as **Figure 3.4**, but for MME mean based on models in (b) group A and (d) group B. Only vectors passing the 90% significance level are plotted. 40

Figure 3.7 Composite SSTA (shading; see scale bar at bottom in units of K) during (a, b, c) JJA (0), (d, e, f) SON (0), (g, h, i) DJF (1), (j, k, l) MAM (1), and (m, n, o) JJA (1), for EP El Niño events based on (a, d, g, j, m) observations, MME mean of models in (b, e, h, k, n) group A and (c, f, i, l, o) group B. Black dots indicate signals passing the 95% significance level..... 43

Figure 3.8 Same as **Figure 3.7**, but for CP El Niño events..... 44

Figure 3.9 Composite precipitation (shading; see scale bar at bottom in units of mm/day) and 850-hPa wind (vectors denoting signals passing the 90% significance level; see scale

arrow at bottom right in units of m/s) anomalies during (a, b, c) JJA (0), (d, e, f) SON (0), (g, h, i) DJF (1), (j, k, l) MAM (1), and (m, n, o) JJA (1) for EP El Niño events based on (a, d, g, j, m) observations, MME mean of models in (b, e, h, k, n) group A and (c, f, i, l, o) group B. White dots indicate precipitation anomalies passing the 90% significance level.....	47
Figure 3.10 Same as Figure 3.9 , but for CP El Niño events.....	50
Figure 3.11 Group A minus group B difference of composite SST (shading; see scale bar at bottom in units of K), 850-hPa stream function (solid and dashed contours denoting positive and negative values, respectively, passing the 95% significance level, with interval of $0.5 \times 10^6 \text{ s}^{-1}$) and rotational wind (vectors; see scale arrow at bottom right in units of m/s) anomalies during the (a) EP and (b) CP El Niño mature phase in DJF(1). Wind vector difference with magnitude smaller than 0.3 m/s is not shown.	52
Figure 3.12 2°N – 2°S NDJFM averaged SST (units: K) climatology over the equatorial Pacific from observations (black line), and MME average based on models in group A (red line) and group B (blue line). Light pink (blue) shadings indicate 0.8 standard deviations from the group A (B) models.....	53
Figure 3.13 The (a) observed and (b, c) MME mean NDJFM climatology of 0° – 10°N averaged zonal divergent wind and pressure velocity (vectors; see scale arrow at bottom right in units of m/s) based on the models in (b) group A, (c) group B and (d) their differences. Shadings denote pressure velocity (units: Ps/s) which is multiplied by a factor of -100 for clarity. Only signals passing the 95% significance level are shown in (d).	56
Figure 3.14 Scatterplots of the NDJFM climatological mean SST (units: $^\circ\text{C}$) over the equatorial Pacific cold tongue (2°S – 2°N , 180° – 120°W) versus locations of the centroid	

of ascending motion associated with (a) EP and (b) CP El Niño-related overturning circulation. Orange (Green) markers indicate the models from group A (B)..... 57

Figure 4.1 Climatology (1979-2014) of the JJA mean (a) precipitation and (b) 850-hPa wind. (c) Regression of the JJA mean precipitation (shading; see scale bar at bottom in units of mm/day) and 850-hPa wind (vectors; see scale arrow at top right in units of m/s) onto the negative JJA mean EASM index. NCEP/NCAR reanalysis and GPCP data are used. See text for details..... 62

Figure 4.2 Taylor diagrams of (a) JJA climatology and (b) interannual variability of precipitation (red circles) and 850-hPa zonal wind (blue circles) for historical runs from 31 CMIP5 models (see **Table 2.1**). Model results are calculated for the region of 0°–50°N, 100°E–140°E, based on the period of 1949-2000. Regression maps of the precipitation and 850-hPa zonal wind onto the EASM index are used to represent the interannual variability of EASM in models..... 65

Figure 4.3 Same as **Figure 4.1**, but for the MME mean based on the selected CMIP5 models. 65

Figure 4.4 0°–20°N DJF averaged (a) EP and (b) CP El Niño-related stream function anomalies (units: $10^6 \text{ m}^2 \text{ s}^{-1}$) over the region (70°E–180°E) based on the nine selected models' historical simulations. 67

Figure 4.5 Composite stream function (shading; see scale bar at bottom in units of $10^6 \text{ m}^2 \text{ s}^{-1}$) anomalies based on (a), (b) observations, (c), (d) MME mean of models in group A and (e), (f) group B during DJF (1) for (a, c, e) EP and (b, d, f) CP El Niño. White dots indicate stream function anomalies passing the 90% significance level..... 67

Figure 4.6 Composite precipitation (shading; see scale bar at bottom in units of mm/day) and 850-hPa wind (vectors denoting signals passing the 90% significance level; see scale arrow at bottom right in units of m/s) anomalies during (a), (b) JJA (0), (c), (d) SON (0),

(e), (f) DJF (1), (g), (h) MAM (1), and (i), (j) JJA (1) for (a, c, e, g, i) EP and (b, d, f, h, j) CP El Niño based on the MME mean from group A-1 models' historical simulations. White dots indicate precipitation anomalies passing the 90% significance level. Red rectangle represents the region for calculating area-integrated absolute value of rainfall anomalies..... 70

Figure 4.7 Same as **Figure 4.6**, but from group A-1 models' RCP 8.5 scenario simulations.

..... 71

Figure 4.8 Same as **Figure 4.6**, but the differences between group A-1 models' RCP 8.5 scenario and historical simulations. Black dots indicate precipitation differences passing the 90% significance level..... 72

Figure 4.9 (a, b) Five points running mean of 5° N–5°S DJF averaged SSTA (units: K) and (c, d) 0°–20°N DJF averaged stream function anomalies (units: $10^6 \text{m}^2 \text{s}^{-1}$) from the composite maps of (a, c) EP and (b, d) CP El Niño events in the 9 selected models.... 75

Figure 4.10 Scatter plots of (a, b) El Niño-related SSTA differences (units: K) and stream function differences (units: $10^6 \text{ m}^2 \text{s}^{-1}$); (c, d) El Niño-related warming location changes (units: °) and stream function location changes between RCP 8.5 scenario and historical outputs, for (a, c) EP and (b, d) CP El Niño, in group A-1 (markers in orange) and B-1 (markers in green). The blue dots indicate the MME mean based on all the nine selected models. 76

Figure 4.11 Bar charts of the (a) EP El Niño-related and (b) CP El Niño-related spatial integrated absolute values of rainfall anomalies over the region of (0°–30°N, 100°E–160°E) during the whole seasonal cycle based on (green bar) RCP 8.5 scenario simulations, (blue bar) historical simulations and (yellow bar) their differences. The fractional changes are denoted on top of the yellow bar (see text for more details). 78

Figure 4.12 Scatter plots of El Niño-related SSTA intensity changes (units: °C) and anomalous rainfall spatial variation changes (units: mm/day) for (a) EP and (b) CP El Niño, based on RCP 8.5 scenario and historical simulations from models in group A-1 (markers in orange) and B-1 (markers in green). The blue dots indicate the MME mean based on all the nine selected models.....	80
Figure 4.13 Composite vertically integrated moisture convergence contributing to the anomalous rainfall (shading; see scale bar at bottom in units of mm/day) and the corresponding moisture flux transport (vectors; see scale arrow at bottom right in units of $\text{kg m}^{-1} \text{s}^{-1}$) anomalies during (a), (b) JJA (0), (c), (d) SON (0), (e), (f) DJF (1), (g), (h) MAM (1), and (i), (j) JJA (1) for (a, c, e, g, i) EP and (b, d, f, h, j) CP El Niño based on the MME mean from group A-1 models' historical simulations. White dots indicate moisture convergence anomalies passing the 90% significance level.....	82
Figure 4.14 Same as Figure 4.13 , but for RCP 8.5 scenario.	83
Figure 4.15 Same as Figure 4.13 , but for moisture convergence and moisture flux transport due to dynamic effect.	84
Figure 4.16 Same as Figure 4.15 , but for RCP 8.5 scenario.	85
Figure 4.17 Same as Figure 4.13 , but for moisture convergence and moisture flux transport due to thermodynamic effect.	86
Figure 4.18 Same as Figure 4.17 , but for RCP 8.5 scenario.	87
Figure 4.19 The future changes of (a) EP and (b) CP El Niño-related spatially integrated total moisture flux convergence (red bar), dynamic term (light blue bar), thermodynamic term (blue bar) and rainfall anomalies (green bar) which are projected onto P' (units: mm/day) during the whole cycle of El Niño events. Note that $\phi(\cdot) = \nabla \cdot \int_{p_s}^{p_t} (\cdot) dp$ is defined in Appendix for simplicity.	90

Figure 4.20 The future changes of (a) EP and (b) CP El Niño-related dynamic effect of moisture flux convergence due to changes of circulation anomalies (Dynamic_Divergence Term, red bar) and mean moisture (Dynamic_Advection Term, blue bar) which are projected onto \hat{P}'_H (units: mm/day) during the seasonal cycle of El Niño. See more details in Appendix for dynamic term decomposition.....	91
Figure 4.21 The future changes of (a, c, e, g, i) EP and (b, d, f, h, j) CP El Niño-related SSTA (units: °C) based on the differences between composite EP and CP El Niño-related SSTA from RCP 8.5 scenario and historical simulations. Black dots indicate SSTA changes passing the 90% significance level.....	92
Figure 5.1 (a, b) Original CO ₂ concentration and TSI for F_AMIP component set in CAM4, respectively. (c, d) Revised constant CO ₂ concentration and TSI in accordant with fixed SST climatology for present-day simulations, respectively. (e) Future projected CO ₂ concentration based on RCP 8.5 scenario. (f) Revised CO ₂ concentration for future time simulations.....	98
Figure 5.2 Future changes of climatological SST (units: °C) based on RCP 8.5 scenario and historical simulations from group A-1 models. See text for more details.....	99
Figure 5.3 Monthly evolution of SSTA during the 2-year life cycle of EP El Niño (units: °C), based on historical runs from group A-1 models, prepared for the AGCM experiments.....	100
Figure 5.4 Same as Figure 5.3 , except for the RCP 8.5 scenario.....	100
Figure 5.5 Same as Figure 5.3 , except for CP El Niño	101
Figure 5.6 Same as Figure 5.5 , except for the RCP 8.5 scenario.....	101
Figure 5.7 Differences of monthly surface temperature (units: °C) between Control_future and Control_present simulations. White crosses indicate the differences passing 90% significance level.....	103

Figure 5.8 Same as Figure 5.7 , but for monthly total vertically integrated precipitable water (units: kg/m ²).	103
Figure 5.9 Same as Figure 5.7 , but for 850 hPa wind (see scale arrow at the top in units of m/s).....	104
Figure 5.10 Same as Figure 5.7 , but for precipitation (units: mm/day).	104
Figure 5.11 Ensemble mean of anomalous precipitation (shading; see scale bar at bottom in units of mm/day) and 850-hPa stream function (solid and dashed contours denoting positive and negative values, respectively, with interval of $0.5 \times 10^6 \text{ s}^{-1}$) during the DJF(1) of (a) EP and (b) CP El Niño based on Exp1. White crosses indicate precipitation anomalies passing the 90% significance level.....	108
Figure 5.12 (a, b) Same as Figure 5.11 , but based on Exp3. (c, d) Same as Figure 5.11 , but for differences between Exp3 and Exp1.....	109
Figure 5.13 Same as Figure 5.12 , but (a, b) for Exp2 and (c, d) for differences between Exp2 and Exp1	109
Figure 5.14 Same as Figure 5.12 , but (a, b) for Exp4 and (c, d) for differences between Exp4 and Exp3.....	110
Figure 5.15 Same as Figure 5.12 , but (a, b) for Exp4 and (c, d) for differences between Exp4 and Exp1.....	110
Figure 5.16 Ensemble mean of vertically integrated moisture flux convergence (negative values correspond to moisture convergence) contributing to the anomalous rainfall (shading; see scale bar at bottom in units of mm/day) and the corresponding moisture flux transport (vectors; see scale arrow at top left in units of $\text{kg m}^{-1} \text{ s}^{-1}$) anomalies during DJF (1) of (a, c, e, g) EP and (b, d, f, h) CP El Niño based on the (a, b) Exp1, (c, d) (e, f) Exp3 and (g, h) Exp4. White crosses indicate moisture convergence anomalies passing the 90% significance level.....	114

Figure 5.17 Same as Figure 5.16, but for moisture flux and its convergence due to dynamic term..... 115

Figure 5.18 Same as Figure 5.16, but for moisture flux and its convergence due to thermodynamic term. 116

Figure 5.19 Differences of vertically integrated moisture flux convergence (shading; negative values correspond to moisture convergence; see scale bar at bottom in units of mm/day) and the corresponding moisture flux transport (vectors; see scale arrow at top left in units of $\text{kg m}^{-1} \text{s}^{-1}$) anomalies between Exp4 and Exp1 for (a, c, e, g) EP and (b, d, f, h) CP El Niño. (a, b) for total moisture transport changes: $\frac{1}{g\rho_w} \delta(\phi(q\vec{V})')$; (c, d) for dynamic term changes: $\frac{1}{g\rho_w} \delta(\phi(q'\vec{V}_c))$; (e, f) for dynamic_divergence term: $\frac{1}{g\rho_w} \phi(q_{cH} \delta(\vec{V}'))$; (g, h) for dynamic_advection term: $\frac{1}{g\rho_w} \phi(\vec{V}_F' \delta(q_c))$; Here H and F correspond to Exp1 and Exp4, respectively. White crosses indicate differences passing the 90% significance level. 117

Figure 5.20 Same as **Figure 5.19**, but for differences between Exp2 and Exp1..... 118

Figure 6.1 Scatter plots of EP and CP El Niño-related (a) SSTA magnitude differences (units: $^{\circ}\text{C}$); (b) SSTA location changes (units: $^{\circ}$) between RCP 8.5 scenario and historical outputs in group A-1 (markers in orange) and B-1 (markers in green) models. The blue dots indicate the MME mean based on all the nine selected models. 121

Figure 6.2 (a, b) Observed sensitivity maps of zonal wind stress anomalies (units: 10^{-3}N/m^2) responses to (a) EP ENSO index (unit: $^{\circ}\text{C}$) and (b) CP ENSO index (unit: $^{\circ}\text{C}$); (c, d) Same as (a, b) but for net heat flux anomalies (units: Wm^{-2}) and ENSO index; (e, f) Same as (a, b) but for thermocline depth anomalies (units: m) (see text for more details). Black dots denote the regression coefficients exceeding 95% confidence level..... 124

- Figure 6.3** Sensitivity maps of zonal wind stress anomalies (units: 10^{-3}N/m^2) responses to (a-i) EP ENSO index (unit: $^{\circ}\text{C}$) and (j-r) CP ENSO index (unit: $^{\circ}\text{C}$) in 9 models from historical outputs (see text for more details). White dots denote the regression coefficients exceeding 95% confidence level..... 128
- Figure 6.4** Same as **Figure 6.3**, but from the RCP8.5 scenario outputs. 128
- Figure 6.5** Sensitivity maps of net heat flux anomalies (units: W/m^2) responses to (a-i) EP ENSO index (unit: $^{\circ}\text{C}$) and (j-r) CP ENSO index (unit: $^{\circ}\text{C}$) in 9 models from historical outputs. Black dots denote the regression coefficients exceeding 95% confidence level. 129
- Figure 6.6** Same as **Figure 6.5**, but from the RCP8.5 scenario outputs. 129
- Figure 6.7** Sensitivity maps of thermocline depth anomalies (units: m) responses to (a-i) EP ENSO index (unit: $^{\circ}\text{C}$) and (j-r) CP ENSO index (unit: $^{\circ}\text{C}$) in 9 models from historical outputs. Black dots denote the regression coefficients exceeding 95% confidence level. 130
- Figure 6.8** Same as **Figure 6.7**, but from the RCP8.5 scenario outputs. 130
- Figure 6.9** Scatter plots of EP and CP ENSO-related (a) atmospheric feedback changes (units: $10^{-3}\text{Nm}^{-2}\text{K}^{-1}$), (b) heat flux feedback changes (units: $\text{Wm}^{-2}\text{^{\circ}C}^{-1}$) and thermocline feedback changes ($\text{m}^{\circ}\text{C}^{-1}$) (see text for more details) in group A-1 (markers in orange) and B-1 (markers in green). The blue dots indicate the MME mean based on all the nine selected models. 133
- Figure 6.10** Bar charts of the rescaled (a) EP ENSO-related and (b) CP ENSO-related atmospheric feedback (green bar), net heat flux feedback (blue bar) and thermocline feedback (yellow bar) changes based on the nine selected models. The red line indicates the future changes of EP and CP El Niño SSTA (units: $^{\circ}\text{C}$). Numbers in the brackets indicate the correlations between feedback and SSTA changes. Note that the

atmospheric feedback changes and thermocline feedback changes (net heat flux feedback changes) are divided by their corresponding maximum (minimum) value among these nine models for rescaling. 134

Figure 7.1 Stream function anomalies (shading; see scale bar at bottom in units of $10^6 \text{ m}^2 \text{ s}^{-1}$) based on the (a, b) MME mean of coupled models in group A-1 and (c, d) AGCM simulations in Exp4 during DJF(1) for (a, c) EP and (b, d) CP El Niño. Note that the EP and CP El Niño SSTA in Exp4 is identical with the MME mean of corresponding SSTA based on group A-1 models. 143

List of Tables

Table 2.1 Description of the 31 CMIP5 coupled models analysed in this study. The 17 models capable of capturing El Niño diversity Xu et al. (2017) are marked in bold and italic fonts; the 9 models, among this group of 17 models, that are also skillful in simulating EASM variability, are marked in red. See text for details.	28
Table 3.1 A list of 17 models which are capable in simulating El Niño diversity in terms of two groups.	39
Table 3.2 Spatial pattern correlation between observed and model simulated precipitation anomalies for EP and CP El Niño, based on MME averages from models in group A and group B. Pattern correlation is calculated over the region of 0°–40°N,100°E–180°E ..	51
Table 5.1 Design of ten sets of AGCM experiments.	97
Table 6.1 The longitude ranges of x (see equations 6.1, 6.2 and 6.3) for different ocean-atmosphere feedbacks in terms of EP and CP ENSO.	133
Table 7.1 Design of three additional sets of AGCM experiments. 0.8 and 1.5 indicate that the El Niño-related SSTA are reduced and enlarged by 0.8 and 1.5 times, respectively. ..	142

1 Introduction

The El Niño-Southern Oscillation (ENSO) is the most important tropical interannual climate phenomenon (Rasmusson and Carpenter 1982), exerting substantial impacts on global climate, marine and terrestrial ecosystems, fisheries and human activities (Timmermann et al. 2018). A conceptual transition from the canonical ENSO to ENSO diversity has been proposed, accounting for its spatio-temporal complexity and varying climatic impacts (Timmermann et al. 2018). Under global warming, ENSO will continue to be the dominant mode of interannual climate variability, and its associated precipitation changes are likely to be modified under global warming (Intergovernmental Panel on Climate Change 2014). However, there is no conclusive answer on the compelling outstanding question: how ENSO characteristics will respond to climate change. ENSO is one of the major factors influencing the rainfall variations over East Asia; hydrological extremes in this region are often driven by fluctuations of ENSO state. It has been projected that East Asian (EA) rainfall tend to become more intense and more variable due to the increased moisture availability in the atmosphere under global warming. Given the tight relationship between ENSO and EA rainfall, it is important to further understand how climate change might modulate the ENSO-EA climate teleconnection, its diversity and underlying physical processes. Notwithstanding large uncertainties in future ENSO projections, a few studies have pointed to vigorous ENSO-induced rainfall variations over the tropics in the future climate which shed light on this study. Here we propose to investigate the El Niño-EA rainfall teleconnection and its diversity under global warming, by diagnosing CMIP5 model outputs under different climatic scenarios and carrying out additional AGCM experiments. The abovementioned studies will greatly facilitate a better understanding of ENSO impacts in a warmer climate.

1.1 Present-day ENSO and its impacts based on observations and models

1.1.1 ENSO and its Diversity

El Niño-Southern Oscillation (ENSO), a coupled ocean-atmosphere phenomenon, is the dominant mode of tropical interannual variability (Wang et al. 2017a). Substantial efforts have been paid to understand and predict the dynamics, physical properties, evolution and climate impacts of ENSO. The oceanic component of ENSO is characterized by a quasi-periodic and asymmetric transformation of warm (El Niño) and cold (La Niña) sea surface temperature anomalies (SSTA) in the central-eastern Pacific. The ENSO lifecycle is known to be phase-locked with the seasonal cycle; El Niño events usually start in boreal spring, grow during the summer and autumn, reach their maximum intensity in winter and decay rapidly during spring (Wang et al. 2017a; Timmermann et al. 2018). Due to the distinct geographical patterns of the SSTA, El Niño events manifest robust diversity. The canonical type, referred to as eastern-Pacific (EP) El Niño, is characterized by maximum warming in the eastern equatorial Pacific. For central-Pacific (CP) El Niño, also known as El Niño Modoki or dateline El Niño, it exhibits more pronounced warming near the dateline and cooling over the far eastern and western Pacific (Ashok et al. 2007; Kao and Yu 2009; Kug et al. 2009; Sohn et al. 2016). To characterize the interannual variability of tropical Pacific SSTA, the leading empirical orthogonal functions (EOF) of variability (see **Figure 1.1**) are commonly used to identify EP and CP El Niño (Xu et al. 2017; Timmermann et al. 2018). The EP El Niño SSTA pattern, which explains the majority of the variance, dominates the Pacific SST variability on the interannual timescale compared with CP El Niño. The magnitude of CP El Niño is weaker than EP El Niño in terms of the warming anomalies. Note that positive SSTA for CP El Niño also extend into the subtropical latitudes, especially in the Northern Hemisphere (**Figure 1.1b**). It is also reported that the cold phase of ENSO, namely La Niña, is relatively weaker than El Niño, exhibiting near-absence of diversity (Wang et al. 2017a; Timmermann et al. 2018).

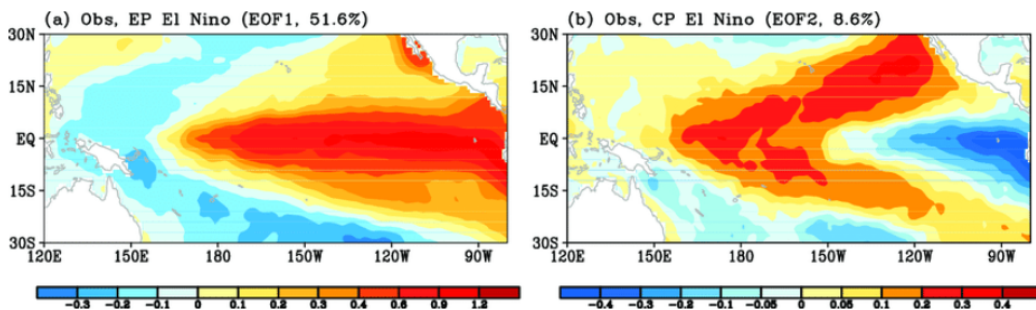


Figure 1.1 First and second leading modes (empirical orthogonal functions) of SST variability corresponding to (a) EP and (b) CP El Niño in the tropical Pacific based on observations taken from Xu et al (2017).

1.1.2 ENSO dynamics

To understand El Niño changes under greenhouse warming, the dynamics of ENSO should be considered first. A schematic diagram, highlighting the critical physical processes involved in neutral and El Niño state, is depicted in **Figure 1.2**. ENSO phenomenon can arise spontaneously from the coupled ocean-atmosphere system and can be triggered by stochastic forcing (Wang and Ni 2018). The Bjerknes feedback, describing the interaction between ocean and atmosphere, is the essential positive feedback for the evolution of ENSO phenomenon (Wang and Ni 2018). In the mean state of tropical Pacific, the low-level easterlies associated with the Walker circulation, are driven and maintained by the zonal gradient of the equatorial SST, with relatively warmer (cooler) seawater in the western (eastern) Pacific. The surface water near the eastern Pacific is warmed and advected into the western Pacific and Maritime Continent (the so-called Pacific warm pool region) by low-level trade wind. Meanwhile, the upwelling of cold water and poleward Ekman transport of surface water in the eastern Pacific merit a cold condition over this region (the so-called cold

tongue region). The west-east SST gradient can further strengthen the Walker circulation and enhance the low-level easterly, forming a positive ocean-atmosphere feedback (**Figure 1.2a**). According to the abovementioned Bjerknes feedback, initial anomalous warming over the equatorial eastern Pacific tends to reduce the zonal SST gradient and hence induce a weaker Walker circulation over the Pacific. The equatorial low-level winds can be weakened, which in turn reinforce the reduced upwelling, resulting in further warming of the surface ocean. The equatorial eastern Pacific, with the anomalously warmer water, gives rise to the canonical El Niño condition relative to the neutral state. In this case, the warm pool region extends eastward into the central Pacific accompanying the slowdown of the westward equatorial surface current. Correspondingly, the strongest convection and Walker circulation are displaced eastward. In general, the positive Bjerknes feedback also operates during El Niño events, in the equatorial central-eastern Pacific (**Figure 1.2b**). The abovementioned mechanisms are also responsible for the formation of CP El Niño. However, the rising motion of CP El Niño-related Walker circulation and its corresponding convections are more concentrated in the central Pacific compared with those of traditional EP El Niño (**Figure 1.2c**).

In addition, the thermocline feedback can also modulate the amplitude of ENSO. Thermocline is a region of strong vertical temperature gradient between the warm mixed layer and cool deep ocean. Eastward-propagating oceanic internal wave (i.e. equatorial Kelvin wave) plays an important role in displacing the thermocline between warm surface water and cold subsurface water. Westerly anomalies over the western Pacific generate downwelling Kelvin waves, which deepen the thermocline in the eastern Pacific and reduce the efficiency of climatological upwelling (Timmermann et al. 2018). Neelin et al. (1998) also pointed out that the slope of thermocline is related to the surface wind stress; a deeper thermocline is located east of the SSTA and further, inhibits the upwelling of cold water. As

shown in **Figure 1.2a**, the thermocline, in a neutral state, slopes downwards from east to west, in accordant with the location of warm pool and cold tongue regions. During EP El Niño, the thermocline deepens in the eastern Pacific with reduced upwelling, hence favoring the accumulation of surface warm water (**Figure 1.2b**); for CP El Niño, the thermocline is deeper underneath the central Pacific where the warm anomalies can be stacked near the surface (**Figure 1.2c**).

The main damping mechanism associated with ENSO is the heat flux feedback; it is a negative atmospheric feedback, linking the net heat flux anomaly and SSTA. Increased convection associated with the warm SSTA lead to the formation of cumulonimbus, reducing the incoming shortwave radiation. Such shortwave radiation change, in turn, plays a dominant role in damping El Niño. Other processes, including the longwave radiation feedback, latent heat flux feedback, and sensible heat flux feedback, together with the shortwave radiation feedback can weaken surface heating. In addition, the warm surface water can be advected to the subtropics, but in a much slower rate compared with processes related to Bjerknes and thermocline feedback. Such poleward transport can also terminate an El Niño event or even initiate the cold phase of ENSO.

While both EP and CP El Niño involve the abovementioned physical processes during their evolution, recent studies have argued that the CP El Niño-related dynamics are different from canonical El Niño in several respects. The zonal advective feedback which emphasizes the zonal advection of mean SST by El Niño-related anomalous zonal current favors the evolution of CP El Niño, while the thermocline feedback favors the EP-type El Niño (Kug et al. 2009). Besides, many studies proposed that the subtropical forcing is a crucial factor in generating CP El Niño (Kao and Yu 2009; Yu et al. 2010; Yu and Kim 2013, 2011, 2010a). In particular, SSTA generated off the coast of Baja California can propagate southwestward to the equatorial Pacific and induce the local ocean-atmosphere interaction with enhanced

zonal advective feedback, triggering the formation of CP El Niño (Yang et al. 2018). This view highlights the effect outside the tropical Pacific for CP El Niño, while physical processes for conventional El Niño are completely confined within the tropical Pacific. In addition, westerly wind bursts, by generating eastward equatorial surface currents and downwelling Kelvin waves, can also account for the existence of the CP El Niño and the irregularity of conventional El Niño (Lian et al. 2014; Chen et al. 2015a). The flattening of the equatorial Pacific thermocline might induce the displacement of the upwelling zone (shift from the tropical eastern Pacific to the central Pacific) which further result in more occurrences of the CP El Niño (Ashok et al. 2007). Also indicated in Chung and Li (2013) and Hu et al. (2016) is the fact that the latent heat flux feedback plays a more efficient damping role in EP El Niño, while it is rather small and negligible in CP El Niño.

To summarize, EP El Niño events tend to involve basin-scale equatorial wind anomalies, a strong relaxation of the zonal tilt of the equatorial thermocline, a prominent role for the thermocline and large eastward shifts of tropical Pacific convection. By contrast, CP El Niño tends to involve more local wind feedbacks, a stronger role for the zonal advective feedback, with little reduction in the zonal tilt of the thermocline and weak shifts of convection (Timmermann et al. 2018). In addition, ENSO diversity may also be triggered by extratropical atmospheric forcing. Overall, the generation mechanism for CP El Niño has yet to be fully understood (Wang and Ni 2018).

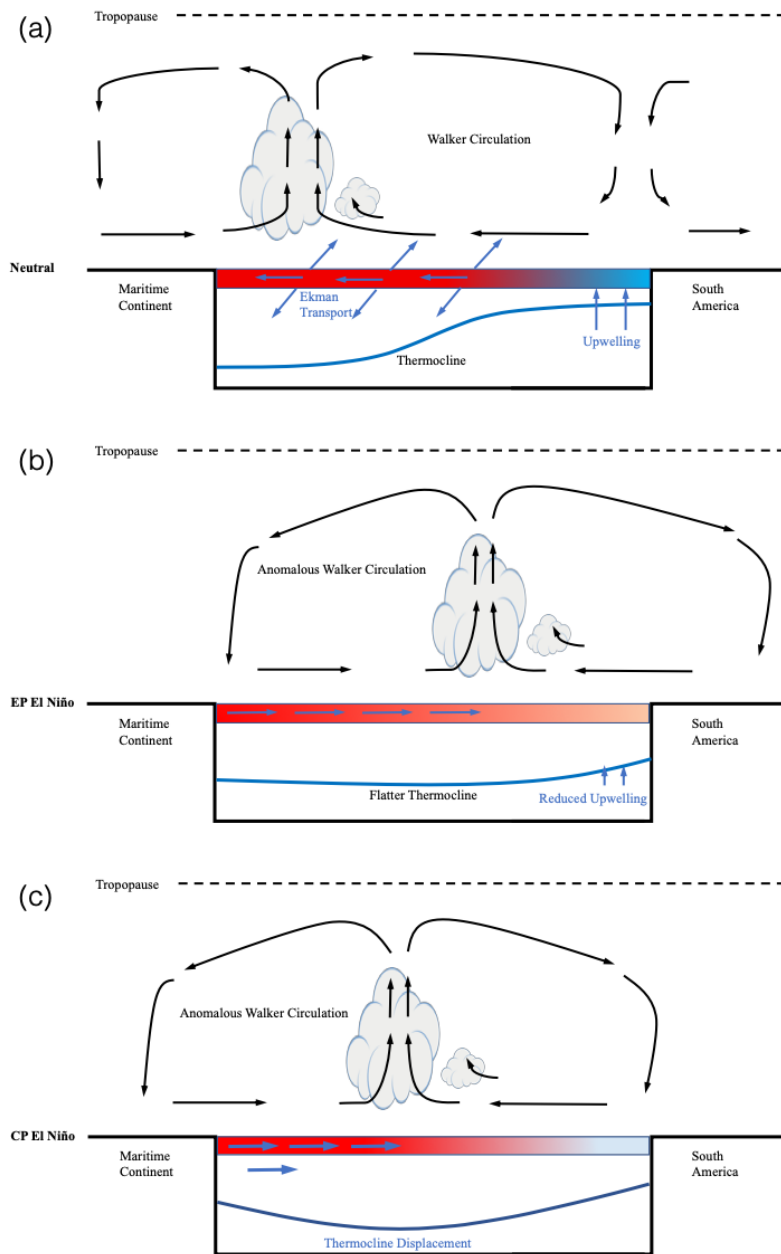


Figure 1.2 Schematic diagrams representing the tropical Pacific and Walker circulation under (a) neutral, (b) EP El Niño and (c) CP El Niño conditions. Warmer and cooler sea surface temperatures are described by red and blue shading (See text in Section 1.1.2 for more details).

1.2 East Asian summer monsoon (EASM) variability

The East Asian monsoon is characterized by a distinct seasonal reversal of monsoon flow, which is driven by the temperature contrast between the Pacific Ocean and East Asian continent (Ha et al. 2012). The summer monsoon over the EA region, known as the EASM, is the major contributor to EA rainfall. As has been studied vigorously, the EASM is an important climate system affecting more than one billion people (Ding and L. 2005). The EASM exhibits large interannual variability which is largely modulated by the ENSO phenomenon, which can induce severe droughts and floods in the EA region. The interannual variability of EASM is one of the major concern in this study, and thus the characteristics of the EASM variability on the interannual timescale should be addressed first. Wang et al. (2008) depicted the dominant mode of EASM interannual variability by performing multivariate empirical orthogonal function (MV-EOF). The principal component of the leading mode is highly correlated with the EASM index proposed by Wang and Fan (1999). The EASM interannual variability features an anomalous anticyclone and tri-pole rainfall pattern over the EA region, accompanying suppressed rainfall over the western north Pacific (WNP) and enhanced rainfall over the Meiyu/Baiu/Changma region and maritime continent.

1.2.1 ENSO-EA rainfall teleconnection

ENSO affects the climate in different regions via different teleconnection patterns (Yang et al. 2018), and is a major driver of the Asian monsoon (Webster et al. 1998) on the interannual timescale. Due to different air-sea coupled processes that occur during the El Niño lifecycle, the response of the EA climate also evolves in time (Feng et al. 2014). In boreal summer when canonical El Niño develops, the anomalous low-level cyclone over the WNP can influence the EASM (Wu et al. 2003). From boreal fall and onward, the anomalous Philippine Sea anticyclone (Wang et al. 2000), which is coupled with in-situ SST (Lau and

Nath 2003), can exert significant impacts on the EA climate till spring. In the following summer after the peak phase of El Niño, rainfall in WNP tends to be weakened, whereas a strengthened Meiyu rainband is found covering central China and Japan (Chang et al. 2000; Wu and Wang 2000).

The above teleconnection picture, however, needs to be modified to accommodate for ENSO diversity. The climate impacts of CP El Niño are distinct from those of canonical El Niño (Kumar et al. 2006; Yu et al. 2012, 2015; Chen et al. 2013; Xu et al. 2013, 2018), presumably due to their very different SST and diabatic heating patterns. For instance, in the developing boreal summer, the influence of CP El Niño on EASM is more evident than that due to the EP-type, whereas the reverse is true in the following summer season during the ENSO cycle (Yuan and Yang 2012). The two El Niño flavors can also lead to opposite rainfall impacts in some Asian regions due to the different longitudinal positions of their related circulation anomalies over the South China Sea (SCS)/Philippines Sea (Weng et al. 2009; Feng et al. 2010, 2011; Feng and Li 2011; Zhang et al. 2011).

To explain such El Niño-EA rainfall teleconnection, a Gill-type response mechanism can be used. Basically, a pair of Rossby waves can be excited to the west of the anomalous heating during El Niño events. The cyclonic circulation anomalies tend to enhance the mean trade winds and hence amplify the evaporation from the ocean, resulting in a cold SSTA west of the El Niño-related SSTA. The cold SSTA can further induce a second Gill-type response with an anticyclonic circulation anomaly west of the cold SSTA. The east flank of this anticyclone can maintain a cold SSTA through evaporation, forming a positive wind-SST-evaporation feedback which guarantees a persistent WNP anticyclone till the summer season when El Niño SSTA has disappeared (Wang et al. 2000). In addition, the Indian ocean capacitor mechanism is proposed to explain the delayed effect of El Niño in modulating EASM. During EP El Niño, the Indian Ocean (IO) exhibits a basin-wide warming when El

Niño peaks and the warming signal persists to the ensuing summer. An atmospheric Kelvin wave, in response to IO warming, is found to propagate and extend eastward into the western Pacific area. Surface friction induces surface divergence and suppresses deep convection in the subtropical WNP (Xie et al. 2009). The suppressed convection can also excite a Rossby wave train propagating northward towards Japan known as the Pacific-Japan (PJ) pattern (Nitta 1987), thus influencing the mid-latitude EA locations in summer.

1.2.2 ENSO, EASM and their teleconnection in CMIP5 models

Numerical modeling is one of the approaches to improve understanding of various climate phenomena, and is also an indispensable tool for projecting future climate change under global warming. Given the importance of ENSO in driving global climate variability, it is imperative to assess the performance of numerical models in capturing ENSO as well as its influence on EASM. Over forty state-of-the-art coupled models, developed by a number of international modeling centers in the fifth phase of the Coupled Model Intercomparison Project (CMIP5), provided simulations of the climate state based on pre-industrial, present-day and various future scenarios. Model diagnosis, validation, and intercomparison based on these simulations enable the communities to improve climate predictability, and more specifically, tackle climate change-related issues. Sperber *et al.* (2013) showed that models from CMIP5 can give realistic EASM, based on the multi-model ensemble (MME) average. Song and Zhou (2013) evaluated the atmospheric general circulation models (AGCM) and pointed out that the climatology and interannual variability of EASM can also be well reproduced. The important role of air-sea coupling in simulations of EASM climatology and interannual variability was further emphasized by Song and Zhou (2014). However, there are still biases regarding the EASM simulations (Sperber *et al.* 2013), which might due to internal variability of the climate system, inter-model spread and scenario uncertainty (Hawkins and Sutton 2009). Also noteworthy is the fact that the Meiyu rainband is

commonly underestimated or even missed (Sperber et al. 2013; Song and Zhou 2014). In general, the CMIP5 models are capable of reproducing the EASM climatology and interannual variability notwithstanding inter-model spreads.

CMIP5 models' capability in simulating ENSO phenomenon has been improved compared to CMIP3, regarding the ENSO amplitude, life cycle, seasonal phase locking and SSTA location (Bellenger et al. 2014). Meanwhile, comparing CMIP5 with its predecessor, it is seen that models' fidelity in simulating ENSO diversity has also improved (Kim and Yu 2012; Kug et al. 2012; Xu et al. 2014). Xu et al. (2017) evaluated 31 CMIP5 models and found that more than half of them can capture well both El Niño flavors. There is also considerable progress in reproducing the ENSO-EA rainfall relationship in the model environments (Flato et al. 2013; Gong et al. 2015; Wu and Zhou 2016; Kim et al. 2017; Feng et al. 2018; Song and Zhou 2013, 2014). To accurately simulate the interannual variability of EASM, air-sea interaction (Wu and Zhou 2016; Song and Zhou 2014), Indian Ocean warming (Wu and Zhou 2016) and SSTA associated with ENSO (Jiang et al. 2017) in CGCMs are stressed. Despite these advances, hitherto relatively few studies focus on the linkage between two types of El Niño and the EA/WNP climate in CMIP5 models. In addition, CMIP5 models exhibit systematic biases in simulating the pattern, strength, and evolution of ENSO SSTA. They can be related to biases in mean state and ENSO feedbacks, which in turn arise from deficiencies in clouds, atmospheric convection and oceanic mixing in these models (Bayr et al. 2018; Timmermann et al. 2018). Taschetto *et al.* (2014) pointed out that biases in ENSO-related SST are related to the unrealistic westward displacement and enhancement of the western Pacific wind stress. Ferrett and Collins (2019) and also An et al. (2017) reported that the inter-model variations of El Niño in terms of its amplitude and location strongly depend on the model-simulated ocean-atmosphere feedbacks. The skill of CMIP5 models in simulating ENSO-related rainfall can also be influenced by the mean state biases. Jiang et al. (2017)

emphasized the climatological SST plays a critical role in simulating a reasonable ENSO-WNP relationship during the ENSO decaying phase. Feng *et al.* (2018) showed that unrealistic SST climatology is responsible for model biases in the anomalous EASM state during the decay phase of CP El Niño. Li et al. (2019) proposed that models with excessive westward extension of Pacific cold tongue tend to displace the El Niño-related SSTA westward, and hence giving an underestimated WNP circulation and rainfall anomalies in post-El Niño summer. Thus, the model-simulated mean Pacific SST plays a critical role in ENSO-EA rainfall teleconnection.

1.3 Future ENSO and its impacts

1.3.1 ENSO and its diversity under global warming

CMIP5 models are commonly used to project the future changes of ENSO, including its intensity, spatial pattern and its related teleconnections (Stevenson 2012; Ham and Kug 2011; Kim and Yu 2012; Kug *et al.* 2010; Huang and Xie 2015; Roy *et al.* 2017; Todd *et al.* 2018; Tedeschi and Collins 2017; Bellenger *et al.* 2014). Based on the latest Intergovernmental Panel for Climate Change Fifth Assessment Report (IPCC AR5), ENSO will continue to be the dominant model of the interannual climate variability, and its associated precipitation changes are likely to be modified under global warming (Intergovernmental Panel on Climate Change 2014). Given the societal and environmental relevance of ENSO, its intensity and frequency under global warming are much concerned. Robust changes including increased variability of EP El Niño and frequency increase of extreme ENSO events are projected (Cai *et al.* 2015a,b, 2018). However, neither observations nor climate models provide a conclusive answer on whether ENSO is going to be strengthened or weakened in response to increasing greenhouse gases (GHGs) (Collins *et al.* 2010). The climate mean state changes under global warming can modulate the ENSO intensity by affecting its related feedback processes (Chen 12

et al. 2015b). In a warmer climate, the changes in the mean climate include a shoaled and less tilted thermocline, weaker zonal currents, and weaker upwelling (Vecchi and Soden 2007a). On one hand, the shoaling and sharpening of the thermocline and the increased thermal stratification tend to enhance ENSO variability. On the other hand, the weakened Walker circulation and strengthened atmospheric damping effect due to warmer mean SST are expected to attenuate ENSO amplitudes (Wang et al. 2017a). These opposing effects might account for the inconsistency of the projected ENSO amplitude (Power et al. 2013; Chen et al. 2015b; Wang et al. 2017a; Stevenson 2012). Regarding the ENSO frequency under global warming, it is rather challenging since the projected ENSO frequency reveals large inter-model inconsistency (Timmerman et al. 1999; Collins 2000; Guilyardi et al. 2012; Xu et al. 2017).

How ENSO diversity will be modified in a warmer climate is another important concern. Based on the selected models which simulate El Niño diversity realistically, Kim and Yu (2012) pointed out that the CP El Niño will be strengthened and become more frequent but uncertainties exist for EP El Niño. Taschetto et al. (2014), however, argued that the CMIP5 models show no enhancement of the ratio between CP and EP El Niño from historical and RCP8.5 scenario runs. In particular, a recent study by Xu et al. (2017) pointed to weaker EP El Niño SSTA, while no robust change of CP El Niño SSTA was projected as inferred from 17 CMIP5 models that well capture both El Niño flavors. Besides, the CP-EP El Niño frequency ratio has a large inter-model spread (Xu et al. 2017). Therefore, how EP and CP El Niño will be modified by global warming remains uncertain.

1.3.2 EASM under global warming

East Asia is vulnerable to extreme rainfall, and it is necessary to have a comprehensive acknowledgement on how EA rainfall will be changed in a warmer climate. **Figure 1.3** gives the schematic processes of how global warming affecting future monsoon. The land-sea 13

temperature contrast increases as the land surface warms faster than the ocean surface. Future monsoonal rainfall changes result from the moisture flux convergence and evaporation, with the former generally larger than the latter (Endo and Kitoh 2014). Under global warming, the global mean specific humidity will increase according to the Clausius-Clapeyron rate of 7% K⁻¹ (Mitchell et al. 1987). At the same time, the tropical circulation will weaken significantly with the increase of GHGs (Vecchi and Soden 2007; Gastineau and Soden 2009). Thus, there is a competition between the thermodynamic (i.e. more abundant moisture) and dynamic (i.e. reduced circulation strength) effects in governing changes of the mean monsoonal precipitation (Ueda et al. 2006; Hsu et al. 2012, 2013). From a global perspective, the moisture flux convergence over the monsoon regions increases as the moistening effect dominates over the weakened circulation effect, hence leading to enhanced monsoonal rainfall. Note that changes in aerosols and land use can also affect solar radiation absorption which further influences the land-ocean thermal contrast. Aerosols can also modify the rainfall by influencing cloud formation (Kitoh 2016). With a focus on EA region, it is noteworthy that the circulation of EASM will be even stronger in the future climate (Endo and Kitoh 2014; Kitoh 2016). Thus, the EASM is projected to become more intense and to affect larger areas (Endo and Kitoh 2014). It was also indicated in Lee and Wang (2012) and Wang et al. (2014) that the time mean EASM is expected to strengthen significantly due to the slightly stronger EASM circulation and more water vapor evaporated under global warming. In addition, a lengthened monsoon season might be projected in the future climate (Kitoh 2016). To better delineate the future change of rainfall, its responses to global warming can be thought of as a combination of thermodynamic component due to moisture increase with no circulation change and dynamic component due to circulation change with no moisture change (Xie et al. 2015). Previous studies have proposed several mechanisms in explaining the precipitation changes under global warming. The rich-get-richer hypothesis

(Held and Soden 2006; Chou et al. 2009), associated with thermodynamic increases in moisture availability and moisture transport, would lead to wet (dry) regions becoming wetter (drier) in the absence of compensating circulation changes in both observations and model simulations. The SST pattern changes were highlighted in warmer-get-wetter mechanism given by Xie et al. (2010), suggesting that SST plays a critical role in shaping the future precipitation in the tropics. To summarize, the thermodynamic component gives rise to the rich-get-richer effect but overestimated due to the compensation by tropical circulation slowdown (Chadwick et al. 2013). SST warming pattern leads to circulation change so that the warmer-get-wetter effect is part of the dynamic effect Xie et al. (2015). Multiple mechanisms, acting differently in different regions, should be combined together to explain the global and regional responses of precipitation variations to a warmer climate.

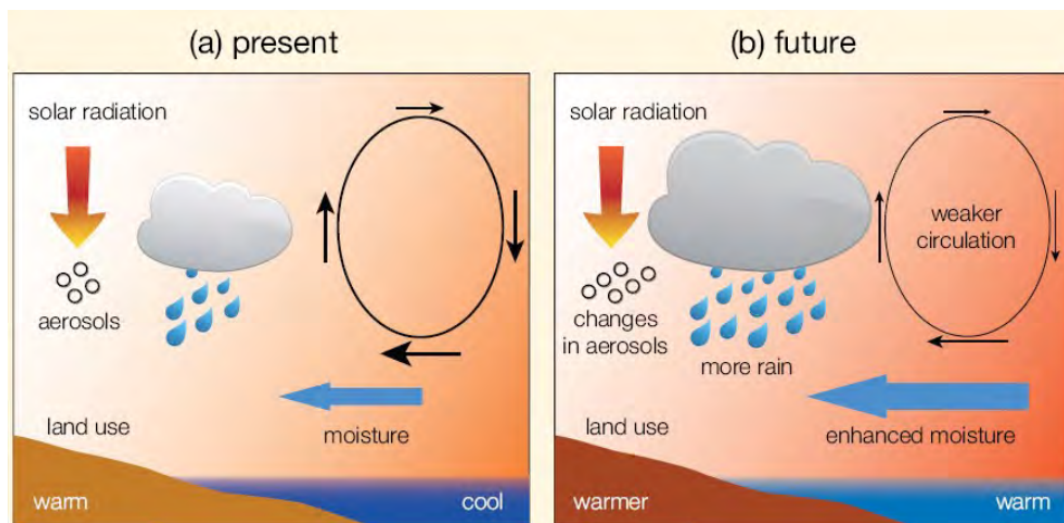


Figure 1.3 Schematic diagram illustrating the main ways that human activity influences monsoon rainfall as the climate warms (see text in section 1.2.2 for more details). From Christensen et al. (2013).

1.3.3 ENSO-EA rainfall teleconnection under global warming

The above descriptions address the plausible changes of ENSO and EASM in the future climate. Regarding their future teleconnection, there exist uncertainties on how it might be changed under global warming (Collins et al. 2010; Tedeschi and Collins 2015; Perry et al. 2017; Todd et al. 2017; Yeh et al. 2018). Notwithstanding the lack of agreement in projected changes of ENSO variability, studies by Seager et al. (2010), Power et al. (2013), Watanabe et al. (2014), Bonfils et al. (2015) and Xu et al. (2017) all pointed to more vigorous ENSO-induced precipitation variations over the tropics. Also, recent studies have shed substantial light on the potential physical processes that control the ENSO teleconnections. Many models show that basic state in the tropical Pacific reveals an El Niño-like ocean warming pattern in response to global warming. The increase in mean-state moisture content associated with surface warming favors more convections and enhance the thermodynamic effect, strengthening the ENSO-related rainfall anomalies over central-eastern Pacific (Huang and Xie 2015), although the weakened atmospheric circulation under global warming may partially offset the rainfall anomalies. Moreover, the El Niño-like warming pattern may induce an eastward shift of the convections which further modifies the ENSO-driven teleconnections (Zhou et al. 2014). Some studies also pointed out that ENSO-driven precipitation anomalies are inherently nonlinear and sensitive to ENSO SSTA patterns and amplitudes (Stevenson et al. 2012; Yeh et al. 2018; Bonfils et al. 2015). Furthermore, ENSO SSTA changes can induce magnitude change of ENSO-related circulations, modulating the ENSO-driven teleconnections through dynamic effect (Tedeschi and Collins 2016). The aforementioned enhancement of ENSO-related tropical Pacific precipitation anomalies may also cause changes in remote regions (Watanabe et al. 2014b). It is projected that the impacts of ENSO on Asian monsoonal rainfall will operate in the same sense or even become stronger under climate change (Turner and Annamalai 2012; Wang et al. 2014). However, no

significant modulation of ENSO on Asian monsoon is found during developing boreal summer by separating the forced and unforced component (Li and Ting 2015). Thus, it is still challenging to investigate how the impacts of ENSO on EA climate might be changed in the future.

1.4 Research questions and thesis outline

As discussed in this chapter, the present-day ENSO-EA rainfall teleconnection in models is inadequate due to the lack of study on its diversity. Additionally, the responses of ENSO and EA rainfall to global warming are quite uncertain due to large inter-model biases, but relatively robust enhancement of ENSO-induced rainfall in the future climate makes it possible to investigate the ENSO-EA rainfall teleconnection under global warming. Consequently, improving our understanding of present and future El Niño-EA rainfall teleconnection with a focus on its diversity is the aim of this thesis.

To lead the analyses in this thesis, four research questions are proposed, forming the basis of chapter 3-6, respectively.

- 1) What are the performances of CMIP5 models in simulating present-day El Niño-EA rainfall teleconnection and its diversity?
- 2) What are the El Niño-EA rainfall teleconnection and its diversity in a warmer climate?
- 3) What physical processes are responsible for the two types of El Niño-related rainfall changes under global warming?
- 4) How global warming modify the two types of El Niño as inferred from individual model studies?

To answer the first question, El Niño-EASM teleconnection and its diversity are explored in great depth in chapter 3. The skillful models are selected based on their capabilities in capturing El Niño diversity and its corresponding overturning circulation. Then, the El Niño-

EASM teleconnection reproduced by skillful and unskillful models is evaluated and compared. Also, possible physical mechanism explaining the contrasting performances of models are investigated. Chapter 3 is heavily based on Wang et al. (2019, submitted to Climate Dynamics).

Chapter 4 extends the analysis from the present-day to future climate by comparing the RCP8.5 scenario and historical outputs in particular models to answer the second question. In order to give the “best” El Niño-EASM teleconnection under both scenarios, the models which can well capture El Niño diversity and EASM variability simultaneously, are obtained for analyzing the future change of El Niño-EASM teleconnection. Further diagnostic studies are conducted to elucidate how dynamic and thermodynamic effects might influence the circulation and hydrological responses over the EA region during two types of El Niño.

The third question and the diagnostic analyses motivate a modeling study to dig deeper into the underlying physical processes dominating future ENSO-related rainfall changes. The multi-model averaged historical and future-projected climatological mean SST, and the corresponding El Niño-related SSTA from different epochs, are archived. These archived SST conditions will be used as lower-boundary forcing in various numerical experiments using AGCM. These AGCM experiments will allow us to better understand the roles of perturbed El Niño forcing and a warmer background climate in modulating the EA hydrological response to two types of El Niño.

Question 4 and chapter 6 are initiated by the fact that future changes of El Niño and its diversity are rather important for projecting El Niño-related rainfall. Thus, the future changes in two types of El Niño and the underlying ocean-atmosphere feedbacks are investigated for individual models. Detailed data and methodology used in this thesis are introduced in chapter 2. Finally, chapter 7 presents the conclusions and discussions of this thesis.

2 Data and Methodology

2.1 Observational and model datasets

As mentioned in Chapter 1, this thesis seeks to address how El Niño-EA rainfall teleconnection might be modified under a warmer background climate. Firstly, two types of El Niño events, EA rainfall variations and their teleconnection based on observations were investigated. To study the ENSO related circulation, monthly mean upper air variables taken from the National Centers for Environmental Prediction/National Center for Atmospheric Research (NCEP/NCAR; Kalnay et al. 1996) were used. The reanalysis data are available at a $2.5^\circ \times 2.5^\circ$ horizontal resolution, with 17 vertical pressure levels from 1000 to 10hPa. In addition, $2.5^\circ \times 2.5^\circ$ precipitation data from the Global Precipitation Climatology Project (GPCP; Huffman et al. 2009) and monthly mean sea surface temperature (SST) from the Hadley Centre Global Sea Ice and Sea Surface Temperature (HadISST version 1.1) analysis with $1^\circ \times 1^\circ$ horizontal resolution (Rayner et al. 2003) were also considered. The analysis period was from 1979 to 2014. To investigate the ENSO-related ocean-atmospheric feedbacks in observations, 1980-2010 monthly subsurface ocean temperature and wind stress based on the Simple Ocean Data Assimilation (SODA, version 2.2.4) were used (Carton and Giese 2008). This dataset covers the global ocean with a uniform horizontal resolution of $0.5^\circ \times 0.5^\circ$ and 40 vertical layers with a 10-meter vertical resolution near the surface. Total downward heat flux at the ocean surface from the National Centers for Environmental Prediction Global Ocean Data Assimilation System (GODAS) product was utilized with $0.333^\circ \times 1^\circ$ horizontal resolution, covering the period of 1980 to 2010 (Behringer and Xue 2004). Then, the performance of state-of-the-art climate models in capturing El Niño diversity, EA rainfall variability, their teleconnection, and ENSO-related ocean-atmosphere

feedback were assessed by comparing them with their observational counterparts. Here, monthly mean atmospheric and oceanic variables in historical (RCP 8.5 scenario) simulations covering the period of 1949-2002 (2050-2099) from 31 CMIP5 models (Taylor et al. 2012) were obtained and examined; brief information about the model experiments can be found in Table 2.1 (see also <http://www-pcmdi.llnl.gov>). Both natural and anthropogenic forcing in the twentieth century were prescribed in the historical simulations, and in the RCP8.5 experiments, anomalous radiative forcing leading to 8.5 W/m^2 by 2100 (equivalent to 1370 ppm of CO₂) representing a high emission scenario was imposed (Xu et al. 2017). The CMIP5 models' ability in reproducing El Niño and its diversity has been rigorously inspected by Xu et al. (2017); 17 (see models in bold in Table 2.1) out of 31 models were identified to give good skills in capturing both EP and CP El Niño SST variability. Since very few models contain multiple realizations in their historical and RCP 8.5 scenario experiments, only the first realization (r1i1p1) from each model was adopted in this thesis. All model outputs were first interpolated onto the same spatial grid as observations before carrying out the analyses.

2.2 Analysis methods

2.2.1 Selection of El Niño events

Two types of El Niño can be defined by various methodologies. Niño index (e.g. Niño3 and EMI index which are SSTA averaged over the particular region) and empirical orthogonal function (EOF) are most commonly used to identify ENSO events. To select the two types of El Niño events in observations and model data, EOF analysis was considered to be more suitable than Niño index. On one hand, EP and CP El Niño events selected by EOF leading modes are independent. However, EP and CP El Niño events identified by Niño index based on CMIP5 models might not be distinctive, if the corresponding indices are significantly correlated. On the other hand, Niño index represents SST variabilities at fixed locations; this

approach assumes that CMIP5 models tend to simulate ENSO-related SSTA as in the observations. However, the spatial patterns of ENSO-related SSTA differ greatly among CMIP5 models, particularly when considering CP El Niño (Cai et al. 2018). The abovementioned indicates that Niño index might not be applicable to define two types of El Niño in CMIP5 models.

In this study, the SST fields were first detrended and bandpass filtered to retain variations with periods longer than 3 months and less than 9 years. Following the same processes as in Xu et al. (2017), empirical orthogonal function (EOF) analyses for the monthly mean SST over the domain of 30°S-30°N, 120°E-80°W were carried out. For each of the 17 models capable of simulating El Niño diversity, EOFs representing EP and CP El Niño SST patterns were then selected and compared with observations. It was found that the leading EOF from all models corresponds to the EP El Niño SST pattern; simulated CP El Niño pattern can be ascertained by comparing either the second or the third leading EOF with the observed CP El Niño-related EOF mode using pattern correlation. Finally, EP and CP El Niño events from either observations or model simulations under historical and RCP 8.5 scenario were identified whenever the November-to-March (NDJFM) mean EP (CP) index, which is the principal component of EOF modes corresponding to EP (CP) El Niño, is greater than one (0.7) standard deviation (see **Figure 2.1** for more details about the two types of El Niño simulated by CMIP5 models).

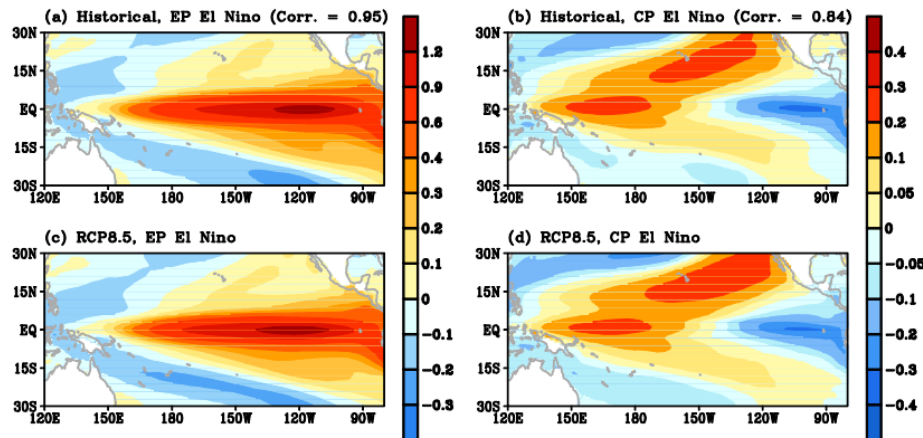


Figure 2.1 Multi-model ensemble (MME) mean of tropical Pacific SST anomalies associated with (a, c) EP and (b, d) CP El Niño (units: K) calculated from (a, b) the historical runs during the 1950–1999 period, and (c, d) RCP8.5 runs during the 2050–2099 period based on 17 selected CMIP5 models. SST maps (units: K) corresponding to EP and CP El Niño are computed by regressing SST anomalies onto the EP and CP El Niño-related principal components, respectively. From Xu et al. (2017).

2.2.2 EASM interannual variability evaluation

Following Sperber et al. (2013), the realism of the EASM interannual variability in all the 31 CMIP5 models (see Table 2.1) was also assessed. This was achieved by regressing the June–July–August (JJA) mean precipitation and 850-hPa wind onto the negative of the JJA mean of the WNP monsoon index proposed by Wang and Fan (1999) (hereafter referred to as the EASM index). This EASM index, defined as the 850-hPa zonal wind (U850) in 22.5–32.5°N, 110–140°E minus U850 in 5–15°N, 90–130°E, captures well the relevant patterns of anomalous tropical and subtropical rainfall, and is related to the anomalous low-level anticyclonic vorticity in the EA-WNP monsoonal region (Wang et al. 2008). The model-simulated regression maps were compared to their observational counterpart by calculating

the pattern correlation coefficient and root mean square error. This way, models which well capture the EASM and its variability can be identified (see text in section 4.1 for more details). Therefore, from the pool of 17 aforementioned models capable of simulating two types of El Niño, models that can reproduce both El Niño diversity and EASM variability can be found.

2.2.3 Diagnosing future change of El Niño-related EA rainfall anomalies

To investigate the EP and CP El Niño-related circulation anomalies, composite analyses based on meteorological variables averaged over identified El Niño events were used. For model simulations, the multi-model ensemble (MME) mean of composite maps was computed by taking their simple average with equal weighting. Significance of composite maps of variables is statistically assessed using the two-tailed Student's t-test. For the MME results, the degree of freedom in t-test refers to the number of El Niño events by aggregating the times of El Niño occurrence from all the models which are used to calculate MME mean to enlarge the sample size.

Moisture budget analysis was also used to delineate the underlying physical processes modulating the future impacts of El Niño on EA/WNP rainfall. The moisture budget is expressed as follows, showing the relationship between precipitation P, vertically integrated moisture flux transport \vec{Q} and evaporation from the surface E:

$$P = -\nabla \cdot \vec{Q} + E \quad (2.1)$$

The first term on RHS, i.e. the convergence of vertically integrated moisture flux \vec{Q} (in units of mm/day) is given by:

$$-\nabla \cdot \vec{Q} = -\frac{1}{g\rho_w} \nabla \cdot \int_{p_s}^{p_t} (q \vec{V}) dp \quad (2.2)$$

where q is specific humidity, \vec{V} horizontal wind, g acceleration due to gravity, ρ_w is the density of water, p_s is surface pressure and p_t equals to 300 hPa. $-\nabla \cdot \vec{Q} > 0$ denotes the convergence of moisture flux, and $-\nabla \cdot \vec{Q} < 0$ represents the divergence of moisture flux. Thus, the moisture budget equation for the anomalous circulation during El Niño events can be written as:

$$P' = -\nabla \cdot \vec{Q}' + E' = -\frac{1}{g\rho_w} \nabla \cdot \int_{p_s}^{p_t} (q \vec{V})' dp + E' \quad (2.3)$$

where prime denotes the anomalies during El Niño events. Here, we define a map \hat{P}' (which is the sign of P') as follows:

$$\hat{P}' = \begin{cases} 1, & \text{if } P' > 0 \\ 0, & \text{if } P' = 0 \\ -1, & \text{if } P' < 0 \end{cases} \quad (2.4)$$

Multiplying equation 2.3 by \hat{P}' :

$$P' \hat{P}' = \left(-\frac{1}{g\rho_w} \nabla \cdot \int_{p_s}^{p_t} (q \vec{V})' dp \right) \hat{P}' + E' \hat{P}' \quad (2.5)$$

where $P' \hat{P}' = |P'|$ is the absolute value of the anomalous precipitation. Considering the spatial variation of the anomalous precipitation over a particular domain, area integration gives:

$$\iint P' \hat{P}' dx dy = \iint |P'| dx dy = \iint \left(-\frac{1}{g\rho_w} \nabla \cdot \int_{p_s}^{p_t} (q \vec{V})' dp \right) \hat{P}' dx dy + \iint E' \hat{P}' dx dy \quad (2.6)$$

Therefore, LHS is the area integrated value of $|P'|$, which is a measure of the magnitude of El Niño-related rainfall anomalies. More importantly, the temporal and spatial variation of El Niño-induced rainfall is mainly driven by the anomalous moisture flux transport. To better understand how future El Niño-related rainfall will be modified, the importance of the dynamical (i.e. $\frac{1}{g\rho_w} \nabla \cdot \int_{p_s}^{p_t} (q_c \vec{V}') dp$, where q_c is the specific humidity climatology) and thermodynamical (i.e. $\frac{1}{g\rho_w} \nabla \cdot \int_{p_s}^{p_t} (q' \vec{V}_c) dp$, where \vec{V}_c is the horizontal wind climatology) terms on the moisture flux were analyzed by decomposing $-\nabla \cdot \vec{Q}'$. Additionally, changes of

each of the dynamic and thermodynamic effects due to global warming can be further decomposed into two terms (Seager et al. 2010; Wang et al. 2017b). More details of the moisture budget decomposition are given in the Appendix.

2.2.4 AGCM experiments

To gain a deeper understanding of how modified El Niño-related SSTA and a warmer climate might influence El Niño teleconnection and rainfall anomalies, further experiments, using an atmospheric general circulation model (AGCM), were carried out. For this purpose, the Community Atmosphere Model version 4 (CAM4) in Community Earth System Model (CESM) version 1.2.2 with a horizontal resolution of $1.9^\circ \times 2.5^\circ$ and 26 vertical levels was employed. The CAM4 has been improved from many aspects compared with its earlier version CAM3. Deep convection is parameterized according to the Zhang and McFarlane (1995) scheme with enhancements to improve the moist physical representations. In particular, the modification of convective available potential energy (CAPE) and convective momentum transports (CMT) in the deep convection scheme lead to significant improvements in the phase, amplitude and pattern of the modeled El Niño. The calculation of cloud fraction has also been modified to give better radiation forcing and surface temperature. For the dynamical core, the finite volume (FV) scheme is used (Neale et al. 2010). In general, CAM4 is widely recognized as capable of capturing ENSO impacts on the EA climate (Tan et al. 2016; Chen et al. 2013; Meehl et al. 2012; Xu et al. 2018). For the control runs and El Niño impact simulations, the component set F_AMIP was adopted, in which the AGCM was forced by prescribed monthly SST. Chapter 5 gives more details about the model experiment design.

2.2.5 Ocean-atmosphere feedbacks during ENSO

Major atmospheric and oceanic feedbacks during El Niño have been measured by linearly regressing related variables in a number of ENSO studies (Jin et al. 2006; Philip and van Oldenborgh 2006; Lloyd et al. 2009; Zheng et al. 2014). In this thesis, atmospheric dynamic feedback, thermodynamical heat flux feedback and oceanic thermocline feedback were quantified for each individual model, in order to better understand the physical mechanisms relating future changes of two types of El Niño. As introduced in Chapter 1, according to the Bjerknes feedback an initial positive SST anomaly in the equatorial eastern Pacific serves to weaken the east-west SST gradient, resulting in decreased trade wind and weakened Walker circulation over the tropical Pacific. The weaker trade wind will further suppress upwelling in the eastern Pacific, leading to even weaker SST gradient and forming a positive feedback process. Here, the sensitivity of surface zonal wind stress anomalies responses to SSTA, representing the atmospheric feedback, can be modeled by:

$$\tau'_x = \mu T' \quad (2.7)$$

In response to a positive (negative) SST anomaly (T'), the zonal surface stress anomaly (τ'_x) will be westerly (easterly). The atmospheric feedback parameter (μ) can represent the sensitivity between these two variables

The main damping mechanism associated with ENSO is the heat release or uptake for the ocean surface, which is a negative atmospheric feedback. The thermodynamical heat flux feedback links the net heat flux anomaly (NH') with the SSTA (T') by sensitivity parameter α as follow:

$$NH' = \alpha T' \quad (2.8)$$

NH' consists of the downward net shortwave heat flux anomalies (SW'), net longwave heat flux anomalies (LW'), sensible heat flux anomalies (SH') and latent heat flux anomalies (LH'). Thus, the above equation can be expressed as:

$$SW' + LW' + SH' + LH' = \alpha_{sw}T' + \alpha_{Lw}T' + \alpha_{Sh}T' + \alpha_{Lh}T' \quad (2.9)$$

Negative (Positive) heat flux feedback parameters ($\alpha, \alpha_{sw}, \alpha_{Lw}, \alpha_{SH}, \alpha_{LH}$) indicate that the ocean surface release (absorb) the heat flux into (from) the atmosphere during El Niño events.

For the thermocline feedback, it can reinforce SSTA growth and plays an important role in ENSO growth as well as phase transition. The tilting of tropical Pacific thermocline depth is tightly correlated with the surface SSTA. Here, the linear regression of the thermocline depth (20°C isotherm, denoted by Z20) and surface SSTA is used to describe the thermocline feedback as:

$$Z20' = \kappa T' \quad (2.10)$$

where κ is the thermocline feedback parameter. Future changes of the aforementioned ocean-atmosphere feedbacks for both types of ENSO were obtained by contrasting the feedback parameters based on historical and RCP 8.5 scenario simulations from each model (see Chapter 6 for more details).

Table 2.1 Description of the 31 CMIP5 coupled models analysed in this study. The 17 models capable of capturing El Niño diversity Xu et al. (2017) are marked in bold and italic fonts; the 9 models, among this group of 17 models, that are also skillful in simulating EASM variability, are marked in red. See text for details.

Model No.	Acronym	Modeling Group (or Center)	AGCM resolution (Lon × Lat, Vertical)	OGCM resolution (Lon × Lat, Vertical)
1	<i>ACCESS1-0</i>	Commonwealth Scientific and Industrial Research Organization (CSIRO) and Bureau of Meteorology (BOM), Australia	192 × 144, L38	360 × 300, L50
2	<i>ACCESS1-3</i>	CSIRO and BOM, Australia	192 × 144, L38	360 × 300, L50
3	bcc-csm1-1	Beijing Climate Center (BCC), China Meteorological Administration (CMA), China	128 × 64, L26	360 × 232, L40
4	<i>bcc-csm1-1-m</i>	BCC, CMA, China	320 × 160, L26	360 × 232, L40
5	CanESM2	Canadian Centre for Climate Modelling and Analysis (CCCma)	128 × 64, L35	256 × 192, L40
6	<i>CCSM4</i>	National Center for Atmospheric Research (NCAR), USA	288 × 192, L26	384 × 320, L60
7	<i>CESMI-BGC</i>	NCAR, USA	288 × 192, L26	384 × 320, L60
8	<i>CESMI-CAM5</i>	NCAR, USA	288 × 192, L26	384 × 320, L60
9	<i>CMCC-CM</i>	Centro Euro-Mediterraneo sui Cambiamenti Climatici (CMCC), Italy	480 × 240, L31	182 × 149, L31
10	CMCC-CMS	CMCC, Italy	192 × 96, L95	182 × 149, L31
11	<i>CNRM-CM5</i>	Centre National de Recherches Météorologiques/Centre Européen de Recherche et Formation Avancée en Calcul Scientifique, France	256 × 128, L31	362 × 292, L42
12	CSIRO-Mk3-6-0	CSIRO in collaboration with Queensland Climate Change Centre of Excellence (QCCCE), Australia	192 × 96, L18	192 × 189, L31
13	<i>FIO-ESM</i>	The First Institute of Oceanography, SOA, China	128 × 64, L26	320 × 384, L40

14	GFDL-CM3	NOAA/Geophysical Fluid Dynamics Laboratory (GFDL), USA	144× 90, L48	360 × 200, L50
15	GFDL-ESM2G	NOAA/GFDL, USA	144× 90, L24	360 × 210, L63
16	GFDL-ESM2M	NOAA/GFDL, USA	144× 90, L24	360 × 200, L50
17	GISS-E2-H	National Aeronautics and Space Administration (NASA) Goddard Institute for Space Studies (GISS), USA	144× 89, L40	144 × 90, L26
18	GISS-E2-R	NASA GISS, USA	144× 89, L40	144 × 90, L32
19	HadGEM2-AO	National Institute of Meteorological Research/Korea Meteorological Administration, Korea	192 × 144, L38	360× 216, L40
20	HadGEM2-CC	Met Office Hadley Centre, United Kingdom	192 × 144, L38	360× 216, L40
21	HadGEM2-ES	Met Office Hadley Centre, United Kingdom	192 × 144, L38	360× 216, L40
22	inmcm4	Institute for Numerical Mathematics (INM), Russia	180× 120, L21	360× 340, L40
23	IPSL-CM5A-LR	Institut Pierre-Simon Laplace (IPSL), France	96 × 96, L39	182× 149, L31
24	IPSL-CM5A-MR	IPSL, France	144 × 143, L39	182× 149, L31
25	IPSL-CM5B-LR	IPSL, France	96 × 96, L39	182× 149, L31
26	MIROC5	Atmosphere and Ocean Research Institute (The University of Tokyo), National Institute for Environmental Studies, and Japan Agency for Marine-Earth Science and Technology, Japan	256 × 128, L40	256 × 224, L50
27	MPI-ESM-LR	Max Planck Institute for Meteorology (MPI-M), Germany	192 × 96, L47	256 × 220, L40
28	MPI-ESM-MR	MPI-M, Germany	192 × 96, L47	802 × 404, L40
29	MRI-CGCM3	Meteorological Research Institute (MRI), Japan	320 × 160, L48	368 × 360, L51
30	NorESM1-M	Norwegian Climate Centre (NCC), Norway	144× 96, L26	384 × 320, L53
31	NorESM1-ME	NCC, Norway	144× 96, L26	384 × 320, L53

3 El Niño-EA Climate Teleconnection and its Diversity in CMIP5 Models

In this chapter, the performance of CMIP5 models in simulating the El Niño-related EA rainfall and the corresponding circulation anomalies was investigated. For EP El Niño, its related SSTA, Walker circulation and teleconnection can be reasonably reproduced; while for CP El Niño, the corresponding counterparts display an erroneous westward shift. The underlying mechanism responsible for models' biases in simulating El Niño diversity and its corresponding teleconnection was stressed.

3.1 Evaluation of CMIP5 models

3.1.1 El Niño diversity and its related overturning circulation

Based on the method as introduced in section 2.2.1, two types of El Niño in both observations and CMIP5 models was inspected by applying EOF analyses. **Figure 3.1** and **Figure 3.2** show the observed and 17 model-generated EOF patterns of SSTA corresponding to EP and CP El Niño, respectively. Consistent with the Figure 2 given by Xu et al. (2017), it can be seen that EP El Niño SST is well reproduced by all selected models, with anomalous warming in the central-eastern Pacific and cooling in the western Pacific (see **Figure 3.1**). The simulation results are largely consistent among models, albeit with some variations in terms of its magnitude as well as its westward extent. For CP El Niño, large inter-model variations in the SSTA pattern exist (see **Figure 3.2**). From observations, it is characterized by positive (negative) anomalies in the central (eastern) equatorial Pacific. Inspection of SST patterns from models reveals that most of them have their warming centers shifted westward, with some even centered in the western Pacific (e.g. ACCESS1-0, GFDL-ESM2G and MPI-

ESM-LR). Additionally, the magnitude of the CP El Niño-related SSTA varies greatly among models. Comparing **Figure 3.1** and **Figure 3.2**, it is obvious that the tongue-shaped warming pattern corresponding to conventional El Niño is highly consistent among these 17 models, while the cold-warm-cold SSTA pattern over the Pacific for CP El Niño is rather inconsistent. Overall, there is robust inter-model consistency in EP El Niño, but much less so in CP El Niño SSTA in the simulated environments.

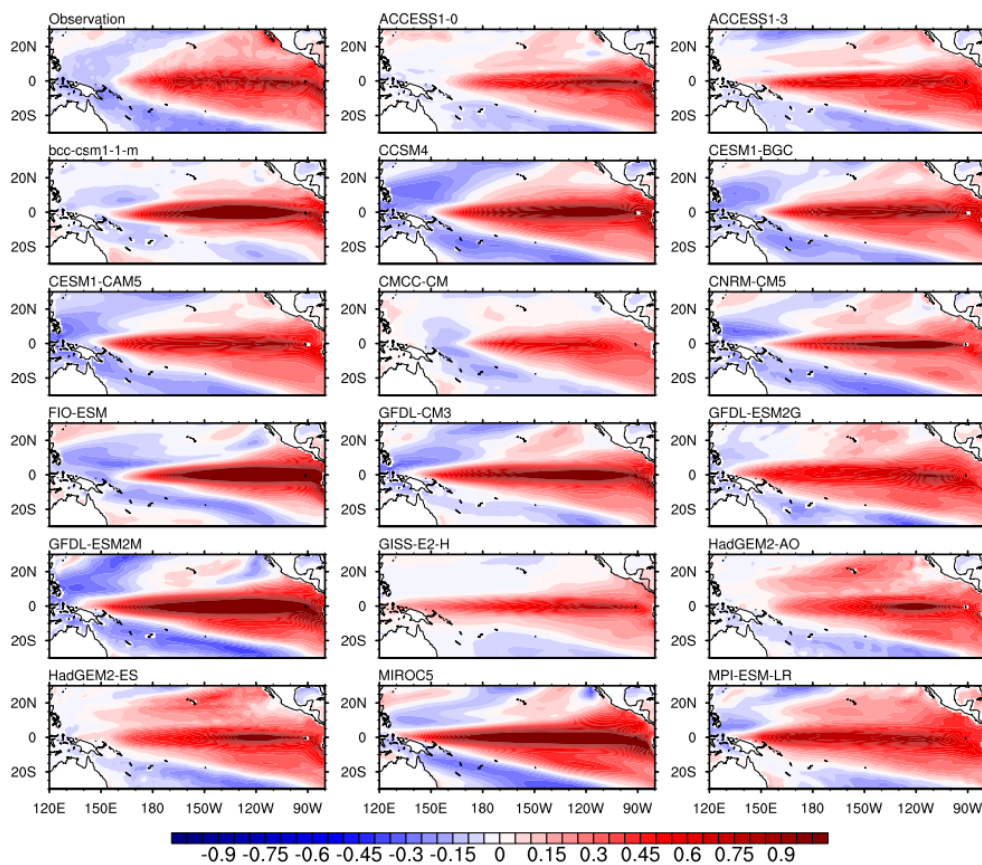


Figure 3.1 EOF patterns of the interannual SST anomalies (see scale bar at bottom; units: K) corresponding to EP El Niño based on observations and each of the 17 selected CMIP5 coupled models. Patterns are computed by regressing SST anomalies onto the corresponding principal components.

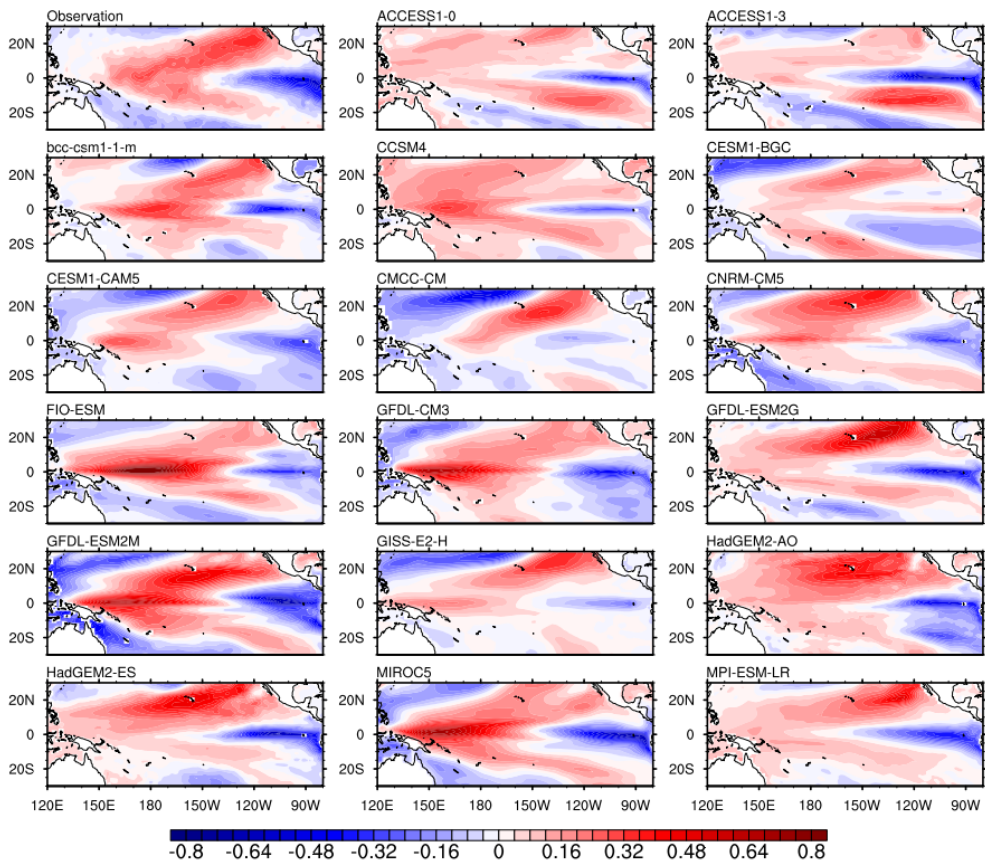


Figure 3.2 EOF patterns of the interannual SST anomalies (see scale bar at bottom; units: K) corresponding to CP El Niño based on observations and each of the 17 selected CMIP5 coupled models. Patterns are computed by regressing SST anomalies onto the corresponding principal components.

After evaluating models' fidelity in capturing different types of El Niño, we now assess their performance in reproducing the related overturning circulation. **Figure 3.3** and **Figure 3.4** give the observed and model simulated NDJFM composites of anomalous vertical and divergent zonal wind components, averaged over 5°N to 5°S, during EP and CP El Niño respectively. From observations, the anomalous Walker circulation during EP El Niño can be seen, which is characterized by a single overturning cell structure over the equatorial Pacific, with ascending motion over the central-eastern Pacific and descent near 120°E (see top left in 32

Figure 3.3). Compared with observations, it can be seen that all models can capture the broad features of such an overturning structure, even though the location and magnitude of the strongest rising and sinking might be different (see **Figure 3.3**). For CP El Niño, the anomalous overturning circulation takes the form of rising from 150°E to 140°W, flanked by sinking west of 130°E and also east of 160°W (see top left **Figure 3.4**). However, its representation in different model environments exhibits large variations (**Figure 3.4**). For some models (e.g. bcc-csm1-1-m, FIO-ESM, GFDL-CM3, GFDL-ESM2M and MIROC5), the location of the rising branch is well captured, whereas for others (e.g. ACCESS1-0, ACCESS1-3, GFDL-ESM2G and MPI-ESM-LR) it is markedly displaced to the west. In fact, further inspection suggests that models with more realistic CP El Niño SSTA tend to better capture the location of the anomalous rising over the equatorial Pacific (compare **Figure 3.2** and **Figure 3.4**). In contrast, models with westward shifted SSTA pattern tend to simulate the overturning circulation more poorly during CP El Niño.

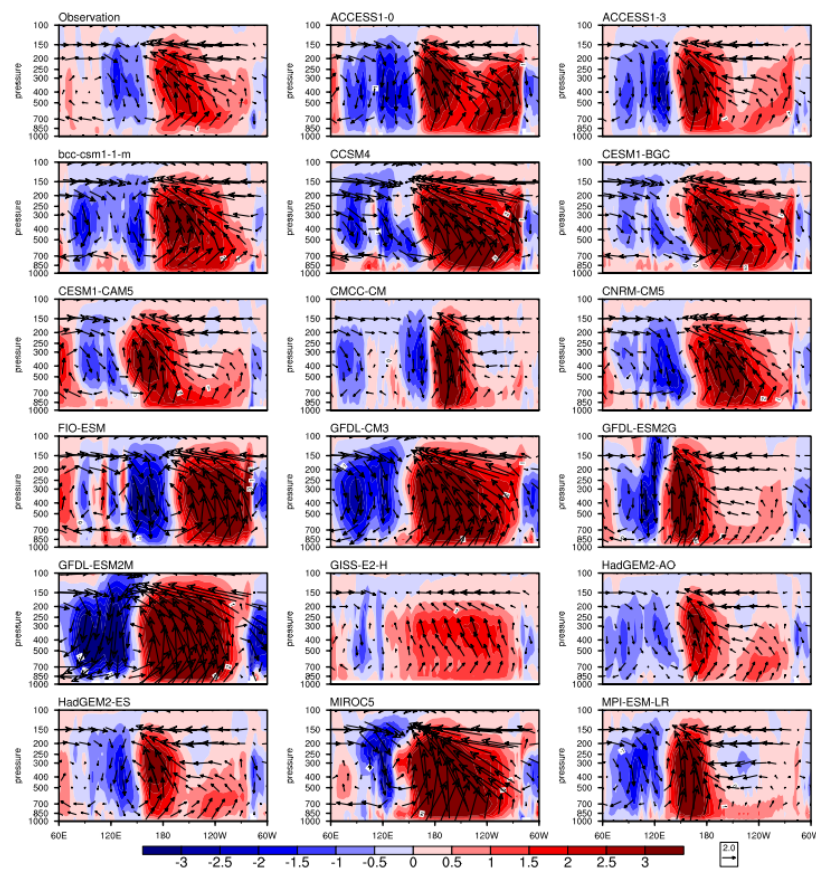


Figure 3.3 Composite of 5°N – 5°S NDJFM averaged zonal divergent wind and pressure velocity (vectors; see scale arrow at bottom right) for EP El Niño based on observations and each of the 17 selected CMIP5 coupled models. Shadings denote anomalous pressure velocity (see scale bar at bottom; units: Pa/s), which is multiplied by a factor of -100 for clarity.

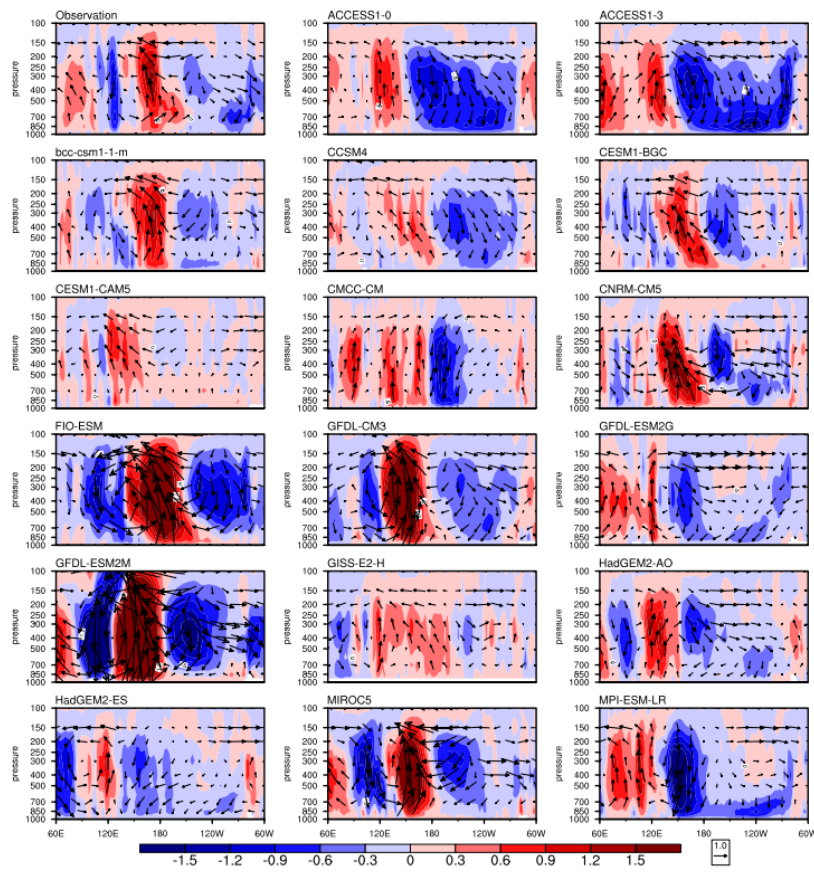


Figure 3.4 Same as **Figure 3.3**, but for CP El Niño.

To better depict the overturning circulation structure during two types of El Niño, and its variation among models, the longitudinal position of the rising motion center was computed, based on the centroid of the pressure velocity:

$$\bar{x} = \frac{\int \omega(x)x dx}{\int \omega(x) dx} \quad (3.1)$$

where $\omega(x)$ denotes the 1000-100hPa and 5°N-5°S averaged composite pressure velocity anomalies and x denotes the longitude. The zonal integration was calculated over 150°E–90°W (100°E–150°W) for EP (CP) El Niño. **Figure 3.5** shows the EP vs CP El Niño-related locations of the rising motion determined this way, from observations and model simulations. It is obvious that locations of EP El Niño-related rising branch from most models clustered

around that from observations. For CP El Niño, the rising branch locations are more scattered; moreover, most models give ascending motion which is displaced to the west compared to the observed. The above is thus consistent with the previously discussed characteristics of model-simulated overturning circulation that the EP El Niño-related Walker circulation anomalies are well captured while the CP El Niño-related counterparts have large inter-model variations (see **Figure 3.3** and **Figure 3.4**). Also shown in **Figure 3.5** is the probability distribution function of the rising branch locations in models, based on kernel density estimation (see Appendix for details) of \bar{x} . Results show that, for EP El Niño-related overturning, there is a uni-modal distribution with a peak at ~ 150 to 155°W , coinciding with the observed value of \bar{x} (see **Figure 3.5**). For CP El Niño, however, a bi-modal shape can be seen, with one peak at $\sim 120^{\circ}\text{E}$ and another near 150°E .

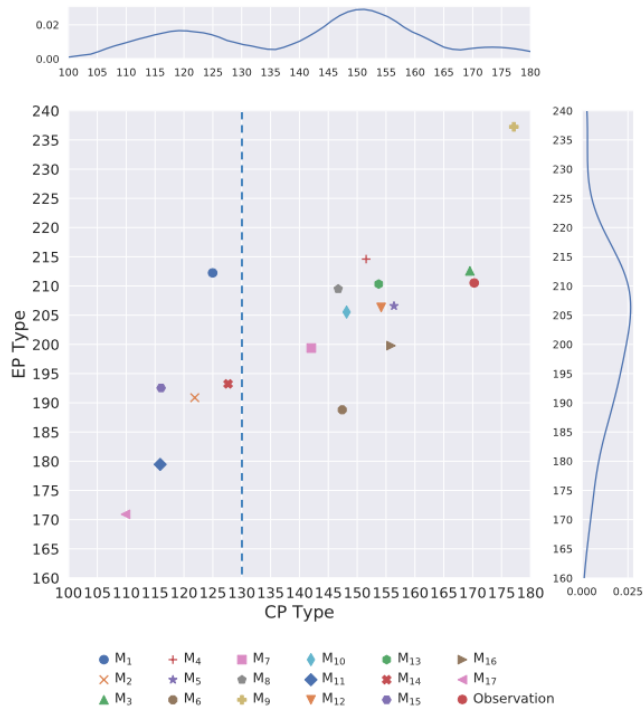


Figure 3.5 Scatter plot of longitudinal locations of the centroid of ascending motion associated with CP and EP El Niño overturning circulation, for observations and the 17 selected CMIP5 models, as well as their probability distribution function based on kernel density estimation for CP (top inset) and EP (right inset) El Niño. The vertical dashed line indicates the 130°E longitude demarcating the two model groups. See text for details.

The above suggests that the 17 selected models can be stratified into two groups. In particular, 11 out of 17 models tend to give more reasonable overturning circulation with the rising centers located east of 130°E during CP El Niño. Hereafter this set of models will be referred to as group A; the model names are listed in **Table 3.1**. The rest is seen to give rising centers west of 130°E during CP El Niño, indicating that their simulated overturning circulation features are very different from observations. These models (also listed in **Table 3.1**) will be referred to as group B. It is also noteworthy that the locations of model-simulated EP and CP El Niño rising center are positively correlated, meaning that models which give

westward (eastward) shifted EP El Niño-related rising branch location tend to give westward (eastward) shifted CP El Niño-related counterpart. **Figure 3.6** gives the composite overturning circulation anomalies for two types of El Niño during NDJFM, averaged over models in group A and B separately. For models in group A, the anomalous Walker circulation during EP (CP) El Niño give a single (double) cell structure (**Figure 3.6a** and **6b**), bearing close resemblance to observations. However, note that while models in group B give anomalous Walker circulation during EP El Niño that resembles the observed (**Figure 3.6c**), their CP El Niño-related overturning circulation exhibits anomalous descending (ascending) motion over the central eastern (western) Pacific (**Figure 3.6d**). In other words, their circulation features during CP El Niño are unrealistic. In the remaining part of this chapter, the 17 selected models will be separated into two groups, and their El Niño-EA climate teleconnection will be examined separately.

Table 3.1 A list of 17 models which are capable in simulating El Niño diversity in terms of two groups.

Model	
<i>Group A</i>	<i>Group B</i>
bcc-csm1-1-m (M3)	ACCESS1-0 (M1)
CCSM4 (M4)	ACCESS1-3 (M2)
CESM1-BGC (M5)	GFDL-ESM2G (M11)
CESM1-CAM5 (M6)	HadGEM2-AO (M14)
CMCC-CM (M7)	HadGEM2-ES (M15)
CNRM-CM5 (M8)	MPI-ESM-LR (M17)
FIO-ESM (M9)	
GFDL-CM3 (M10)	
GFDL-ESM2M (M12)	
GISS-E2-H (M13)	
MIROC5 (M16)	

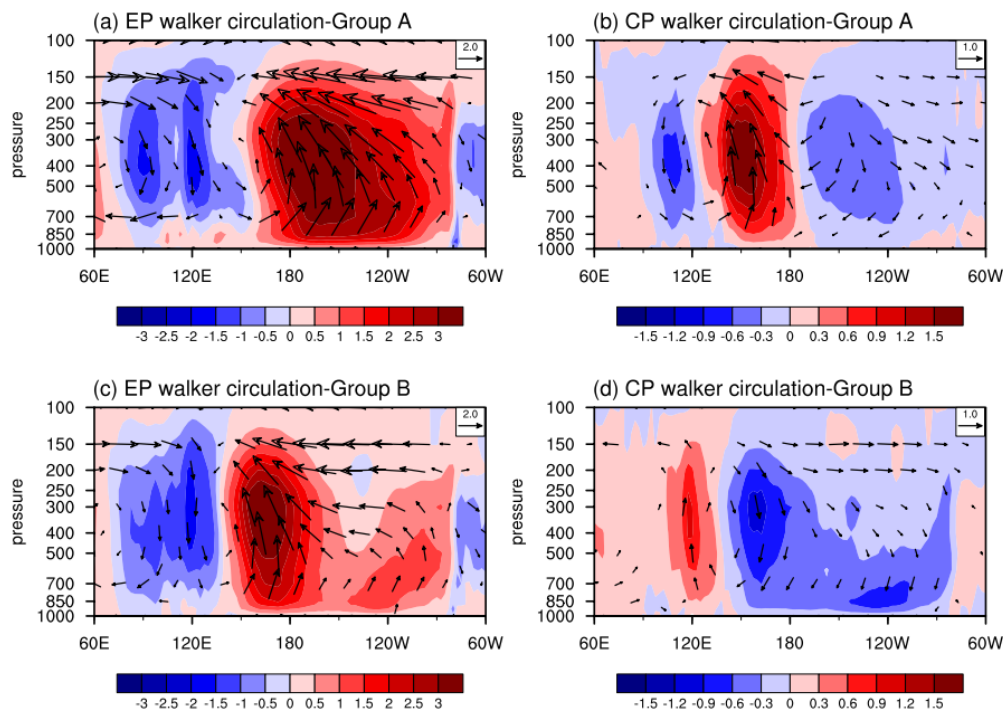


Figure 3.6 (a, c) Same as **Figure 3.3**, but for MME mean based on models in (a) group A and (c) group B. (b, d) Same as **Figure 3.4**, but for MME mean based on models in (b) group A and (d) group B. Only vectors passing the 90% significance level are plotted.

3.1.2 El Niño-related SST evolution

To unveil the connection between the El Niño-related large-scale circulation and their accompanying oceanic changes, composite SSTA during the ENSO cycle, i.e. SSTA averaged over the developing boreal summer (JJA(0)), the September-to-November period (SON(0)), December-to-February period (DJF(1)), March-to-May period (MAM(1)), and the decaying summer (JJA(1)) from observations, group A and group B MME mean are given in **Figure 3.7** and **Figure 3.8**, respectively. During EP El Niño, warmer-than-normal SST is found to persist in the eastern equatorial Pacific from the developing to decaying boreal summer (see left column of **Figure 3.7**). At the same time, there is a horse-shoe shaped colder-than-normal SST pattern centered at the western Pacific (Trenberth and Stepaniak

2001) from JJA(0) to around MAM(1). SST cooling is also found starting from SON(0), while warming is present over the SCS, East China Sea and the tropical Indian Ocean (see left column of **Figure 3.7**). Compared with these observed SSTA patterns, it can be seen that both group A and group B models can reasonably reproduce the EP El Niño SSTA evolution in their simulated environments (see middle and right columns of **Figure 3.7**). In particular, prominent features such as the growth and decay of the warm eastern Pacific signal, SSTA patterns over the north Pacific, Indian Ocean and in the marginal seas adjoining western Pacific during the EP El Niño cycle are captured by both sets of models.

We now inspect models' performance in simulating the SSTA evolution during CP El Niño. From observations, there is significant warming over the equatorial central Pacific in the developing phase of CP El Niño in JJA(0); such positive SSTA appears to be connected to signals further north in the subtropical north Pacific (Yu and Kim 2010b, 2011). Negative SSTA are also seen over the far eastern Pacific, as well as in the western Pacific extending into SCS. Part of these cooling signals become significant in the ensuing seasons of SON(0) and DJF(1), while the central Pacific warming persists throughout the whole CP El Niño cycle till JJA(1) (see left column of **Figure 3.8**). Comparing the MME mean from the two groups with observations, group A models can capture well both the SSTA pattern and its temporal evolution. For instance, the aforementioned tri-pole SSTA and the persistent central Pacific warming during CP El Niño are well represented in the group A MME mean (see middle column of **Figure 3.8**). However, in group B, there is a clear westward shift of the position of equatorial Pacific warming; positive SSTA is present over the central-western Pacific, while negative SSTA over the eastern Pacific is too strong and expands westward, such that there is oceanic cooling close to the dateline (see right column of **Figure 3.8**). Accompanying such a westward shift of the broad-scale Pacific SSTA, cooling signal to the far west is now confined to SCS and appears only in DJF(1).

In summary, while both group A and group B models can reproduce the SSTA evolution during EP El Niño, only models from group A can realistically simulate CP El Niño SSTA. For group B models, during CP El Niño there is excessive extension of negative SSTA towards the central Pacific. Meanwhile, warmer-than-normal SST is found over the western Pacific and the Philippines. The above oceanic changes from group B models are markedly different from observations, which show warmer (colder) -than-normal SST over the central (western) Pacific (see **Figure 3.8**). This suggests that the erroneous CP El Niño-related Walker circulation previously discussed can be attributed to SSTA biases in these models; accompanying the intense negative SSTA, sinking motion over the eastern Pacific extends too far to the west, while rising motion is collocated with positive SSTA in the western Pacific in group B models. The possible implication of these biases on the simulated EASM changes during ENSO will be assessed in the next section.

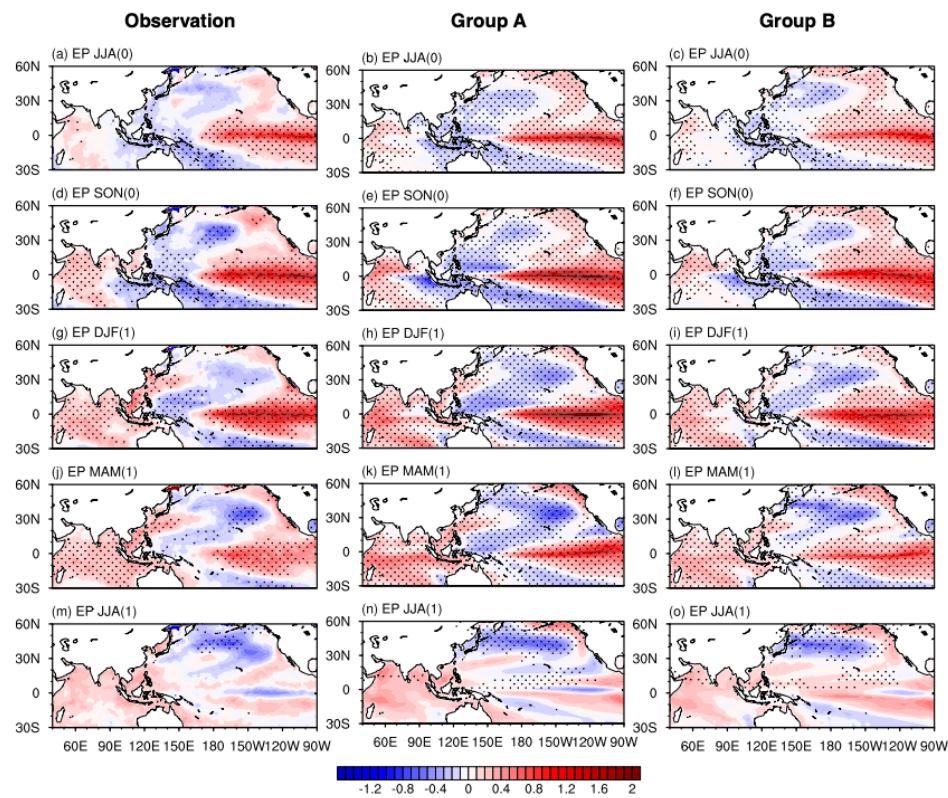


Figure 3.7 Composite SSTA (shading; see scale bar at bottom in units of K) during (a, b, c) JJA (0), (d, e, f) SON (0), (g, h, i) DJF (1), (j, k, l) MAM (1), and (m, n, o) JJA (1), for EP El Niño events based on (a, d, g, j, m) observations, MME mean of models in (b, e, h, k, n) group A and (c, f, i, l, o) group B. Black dots indicate signals passing the 95% significance level.

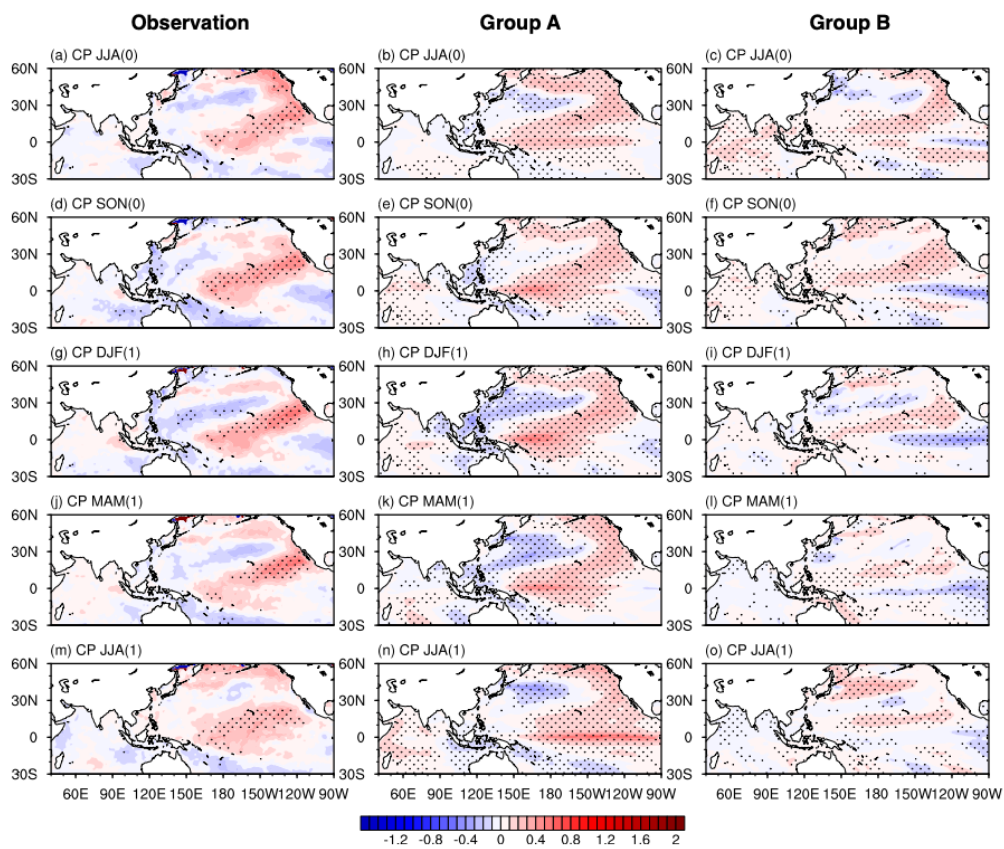


Figure 3.8 Same as **Figure 3.7**, but for CP El Niño events.

3.2 El Niño-EA monsoon teleconnection and its diversity

Diverse EA monsoon anomalies can be driven by the two types of El Niño events during their life cycle. **Figure 3.9** and **Figure 3.10** show the anomalous precipitation and 850-hPa wind composites for two types of El Niño events based on observations (see left columns of figures). In JJA(0) during the EP El Niño cycle, warmer-than-normal SST can cover a broad equatorial region from the eastern to the central Pacific (see **Figure 3.7a**). Consistent with this is significantly enhanced precipitation near the dateline, while there is significant drying further west over equatorial WNP and eastern Indian Ocean. Accompanying the anomalous convection are low-level westerly wind anomalies in the deep tropical WNP, and an anticyclone over the eastern Indian Ocean/Indo-China region (**Figure 3.9a**). The latter is consistent with a Gill-type response in the low levels to suppressed diabatic heating over WNP/SCS. In SON(0), the magnitude and also the geographical coverage of suppressed rainfall west of about 150°E are found to increase as EP El Niño develops (**Figure 3.9d**). During DJF(1) and MAM(1), the circulation response over WNP is characterized by the formation and persistence of the Philippine Sea anticyclone (Wang et al. 2001). Significant low-level anticyclonic flow over the far western Pacific, with suppressed precipitation over a broad region covering the Philippines and SCS, can be clearly seen (**Figure 3.9g** and **3.9j**). The related southwesterly wind branch also brings abundant moisture to the eastern coastal China, leading to enhanced rainfall there in these seasons when EP El Niño occurs. At the same time, the tropical Indian Ocean becomes anomalously warm (see **Figure 3.7g** and **3.7j**). The tropical Indian Ocean warming gives rise to EP El Niño's impact on the EA climate as late as JJA(1), by generating an atmospheric Kelvin wave response and a related anomalous high over WNP (Xie et al. 2009). Through such an "Indian Ocean capacitor" effect, the dry signal which passing the 90% significance level over the Philippines is sustained, while the

EASM rainfall is enhanced as a result of anomalous low-level southwesterlies to westerlies (**Figure 3.9m**).

During the CP El Niño cycle, there are significant wetter-than-normal conditions over WNP in JJA(0), accompanied by an anomalous low-level cyclone in the vicinity (**Figure 3.10a**). In the subsequent seasons of SON(0), DJF(1) and MAM(1), rainfall is suppressed over the Philippines, SCS and part of Indo-China (**Figure 3.10d, 3.10g** and **3.10j**). However, compared with its counterpart during EP El Niño, such a dry zone has a relatively small geographical extent. Consistent with warming in the central Pacific from SON(0) to MAM(1) (**Figure 3.7d, 3.7g** and **3.7j**), significant anomalous westerlies over the equatorial western-central Pacific are seen in DJF(1) and MAM(1), suggesting a sustained Gill-type response (**Figure 3.10g** and **3.10j**). In JJA(1), the dry signal recedes to locations south of 10°N (**Figure 3.10m**). Throughout this CP El Niño cycle, there is persistent surplus rainfall near the equator around 150°E and to the east, accompanying anomalous westerlies in accordance with the Gill-type response. The latter feature is also different from EP El Niño, during which rainfall anomaly at the same central-to-eastern Pacific location changes its sign from positive to negative. It is also noteworthy that the significance level for CP El Niño-related rainfall and low-level wind is lower than that for EP El Niño.

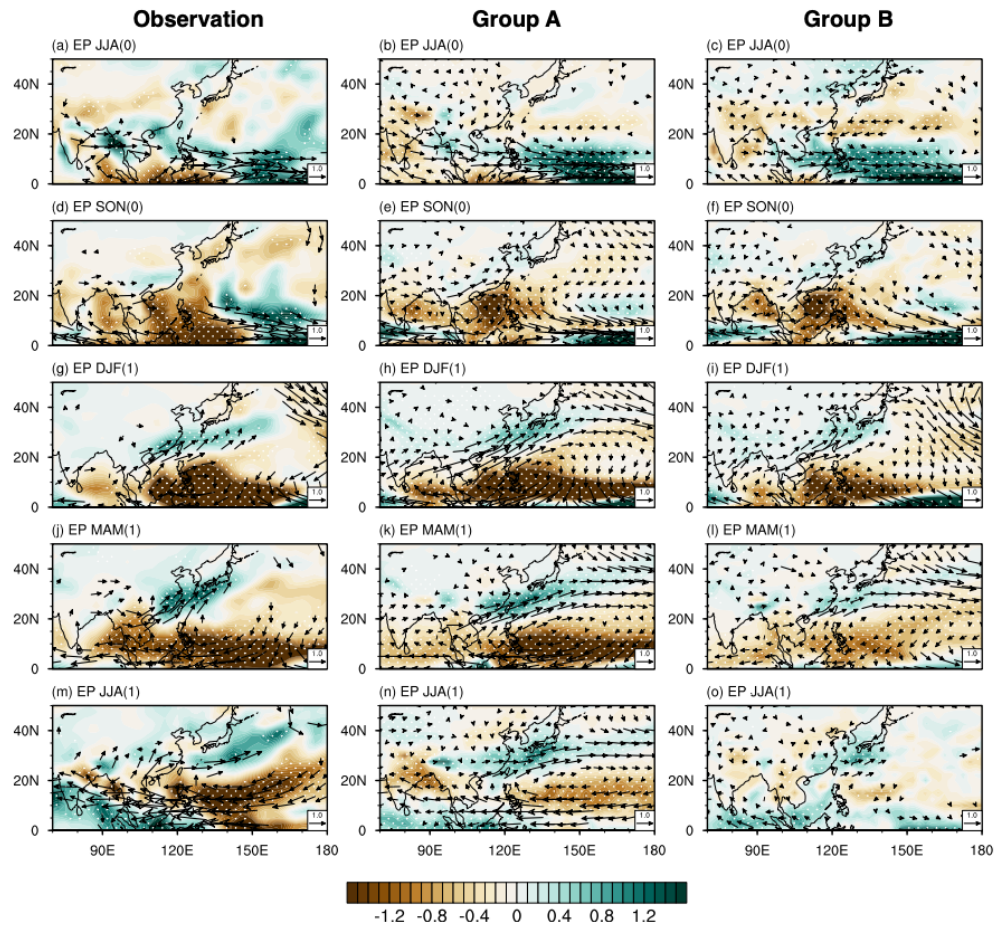


Figure 3.9 Composite precipitation (shading; see scale bar at bottom in units of mm/day) and 850-hPa wind (vectors denoting signals passing the 90% significance level; see scale arrow at bottom right in units of m/s) anomalies during (a, b, c) JJA (0), (d, e, f) SON (0), (g, h, i) DJF (1), (j, k, l) MAM (1), and (m, n, o) JJA (1) for EP El Niño events based on (a, d, g, j, m) observations, MME mean of models in (b, e, h, k, n) group A and (c, f, i, l, o) group B. White dots indicate precipitation anomalies passing the 90% significance level.

The middle and right columns of **Figure 3.9** and **Figure 3.10** also depict the same set of variable composites based on the MME mean from group A and group B, respectively. Compared with observations, it is noticed that both groups of models can well capture the anomalous precipitation and 850-hPa wind during the entire EP El Niño cycle. In particular,

significantly suppressed (surplus) precipitation over WNP and SCS (the eastern coastal China) and the accompanying Philippine Sea anticyclone can be seen. Additionally, the tropical Indian Ocean warming and the enhancement of EASM during JJA(1) are also reproduced by both sets of models. It is also noteworthy that EP El Niño-related circulation anomalies in group A are stronger than those in group B models, which is consistent with the different EP El Niño SSTA magnitude in the two groups of models (see middle and right columns of **Figure 3.7**). During CP El Niño, group A models can also simulate the associated precipitation and low-level wind anomalies. For instance, the surplus rainfall accompanying cyclonic low-level circulation near 150°N as well as dry conditions with northerly over SCS from SON(0) to MAM(1) are reasonably captured with high significance level (see **Figure 3.10e, 3.10h** and **3.10k**). However, the group B MME mean composites reveal large bias relative to observations (see right column of **Figure 3.10**). In this set of models, positive rainfall anomalies over the equatorial central Pacific tend to extend farther west, such that the SCS region now become wetter-than-normal. At the same time, there is cyclonic low-level wind response in the vicinity, which is remarkably different from observations. In addition, the significant signals cover a smaller region bases on group B models. To further evaluate the performance of two model groups, spatial correlation between observed and model simulated precipitation over the region of 0°–40°N, 100°E–180°E is computed, throughout the entire cycle of two types of El Niño (see **Table 3.2**). Overall, the spatial correlations for EP El Niño from JJA(0) to JJA(1) are relatively high (larger than 0.5), with the exception of JJA(1) for group B (with correlation of ~0.12). In addition, the spatial correlations based on group A models are higher than the counterparts based on group B models. For CP El Niño, spatial correlation is high for group A, but not for group B. The latter gives negative values during JJA(0), SON(0) and DJF(1), while those for MAM(1) and JJA(1) are also low (less than ~0.1). To better understand how the contrasting SSTA patterns affect the El Niño-related

teleconnection, **Figure 3.11** shows the differences between group A and group B model composite SST, 850hPa stream function and rotational wind anomalies DJF(1) for two types of El Niño. The positive (negative) SSTA difference over the central-eastern (western) Pacific (i.e. stronger SSTA warming during EP El Niño in group A), favors stronger low-level cyclonic (anticyclonic) circulation anomalies near 150°W (WNP). In particular, anomalous cyclones are excited west of the enhanced warming. Further to the west, a similar (but anticyclonic) circulation response west of the cold SSTA can also be found (**Figure 3.11a**). Such a Rossby wave response can bring more moisture to the eastern coastal China and inhibit the convections over SCS and WNP, leading to markedly stronger EP El Niño-driven rainfall anomalies based on the MME mean of group A models compared with those given by group B models (**Figure 3.9**). For CP El Niño, the SSTA difference gives a central Pacific warming signal, with significant low-level cyclonic circulation in WNP, which gives rise to a better CP El Niño-related teleconnection in group A compared to group B models (**Figure 3.11b**).

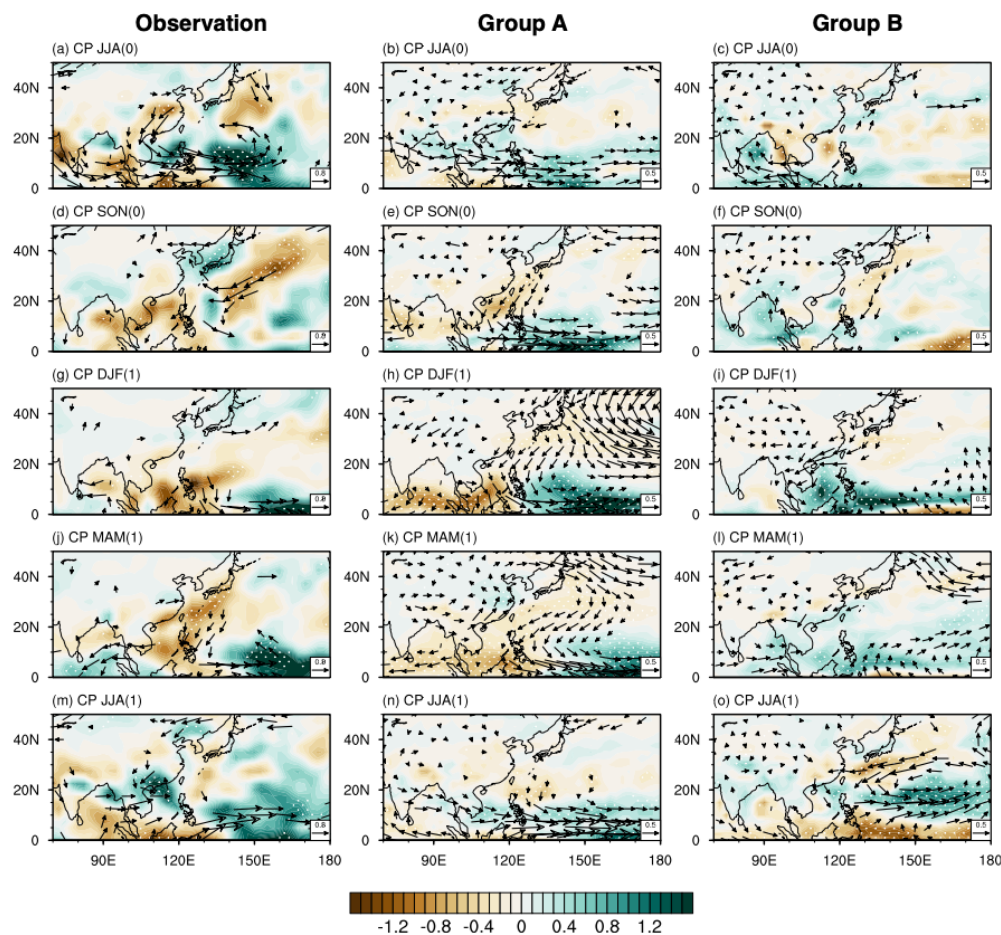


Figure 3.10 Same as **Figure 3.9**, but for CP El Niño events.

Table 3.2 Spatial pattern correlation between observed and model simulated precipitation anomalies for EP and CP El Niño, based on MME averages from models in group A and group B. Pattern correlation is calculated over the region of 0°–40°N, 100°E–180°E.

EP El Niño			CP El Niño		
Season	Group A	Group B	Season	Group A	Group B
JJA (0)	0.798	0.541	JJA (0)	0.506	-0.203
SON (0)	0.695	0.564	SON (0)	0.168	-0.213
DJF (1)	0.811	0.521	DJF (1)	0.540	-0.360
MAM (1)	0.895	0.676	MAM (1)	0.762	0.100
JJA (1)	0.681	0.120	JJA (1)	0.626	0.111

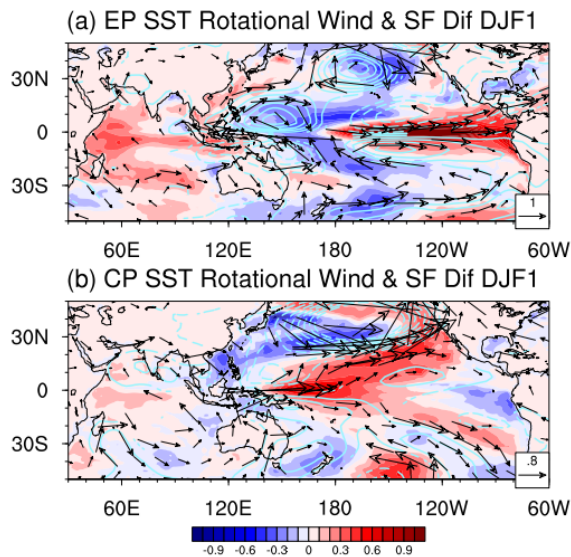


Figure 3.11 Group A minus group B difference of composite SST (shading; see scale bar at bottom in units of K), 850-hPa stream function (solid and dashed contours denoting positive and negative values, respectively, passing the 95% significance level, with interval of $0.5 \times 10^6 s^{-1}$) and rotational wind (vectors; see scale arrow at bottom right in units of m/s) anomalies during the (a) EP and (b) CP El Niño mature phase in DJF(1). Wind vector difference with magnitude smaller than 0.3 m/s is not shown.

To summarize, even though both group of models can well capture the impact of EP El Niño on the EA climate, only group A can realistically reproduce the teleconnection effect during CP El Niño. This also reflects different model groups' performance in capturing the anomalous overturning circulation and SST during two types of El Niño. Due to the westward extension of warm SSTA and rising motion over central-western Pacific in group B models, wetter-than-normal conditions are found over the far western Pacific/SCS area when CP El Niño occurs. In contrast, the ENSO-related anomalous circulation is well simulated in group A, consistent with the well captured SSTA. All these highlight the crucial role of ENSO-related SST in determining the El Niño-EASM teleconnection.

3.3 Role of tropical basic state on El Niño-EA monsoon teleconnection

To unveil the possible role of the basic state on models' performance in simulating El Niño diversity and its impacts, **Figure 3.12** compares the NDJFM climatological SST along the equatorial Pacific from observations, group A and group B models. Many previous studies indicate that most coupled general circulation models suffer from a cold SST bias and excessive westward extension of the equatorial Pacific cold tongue (Dai, 2006; Zheng *et al.*, 2012; Li and Xie, 2012, 2014). It can be seen that both group A and B give mean Pacific SST cooler than the observed, but with group B having a more severe cold tongue bias and a stronger westward intrusion. (In fact the mean SST in group B is severely lower than that from group A, with a difference of 0.8 standard deviation; see **Figure 3.12**).

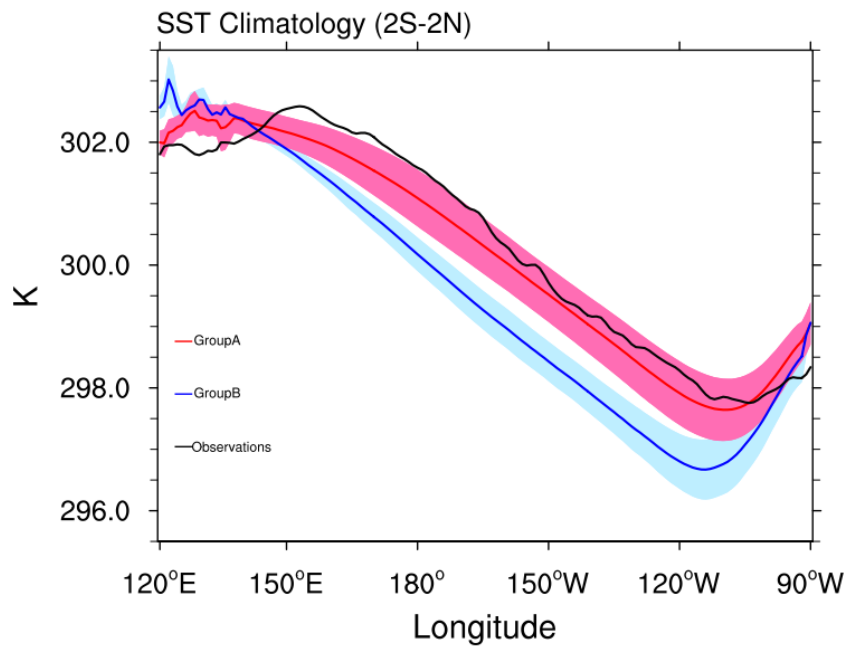


Figure 3.12 2° N– 2° S NDJFM averaged SST (units: K) climatology over the equatorial Pacific from observations (black line), and MME average based on models in group A (red line) and group B (blue line). Light pink (blue) shadings indicate 0.8 standard deviations

from the group A (B) models.

The climatological Walker circulations over the same NDJFM season for observations and the two groups of models as well as their difference, are depicted in **Figure 3.13**. The climatological Walker circulation patterns from both groups resemble the observed, albeit with different magnitudes. Their difference is characterized by significant descending (ascending) motion over the eastern (western) equatorial Pacific. This implies that the mean Walker circulation simulated by group B models is stronger than that from group A. In fact, there is also slightly stronger zonal SST gradient at the equator from group B, which is consistent with the stronger easterlies and in accordance with the Bjerknes feedback. In addition, the location of ascending-descending transition of the MME mean Walker circulation based on group B models seems to be shifted westward relative to that based on group A models (**Figure 3.13**), consistent with the fact that equatorial cold tongue bias can lead to a westward shifted position of the rising branch of Walker circulation (Bayr et al. 2019, 2018). **Figure 3.14** gives the model simulated rising motion centers (same as those shown in **Figure 3.5**) for EP and CP El Niño vs. the climatological NDJFM mean SST over the equatorial eastern Pacific. It can be seen that the longitudinal location of the anomalous rising branch is positively correlated with the mean SST state of models, regardless of the El Niño flavor. This supports our interpretation that the mean oceanic state plays a strong role in determining the anomalous Walker cell, and hence the teleconnection during El Niño. In fact, there is a hint that the position of the CP El Niño-related ascending center is more sensitive to the basic state (see slopes of the best-fit curves), in accordant with the higher sensitivity of CP-type SSTA shifting in response to mean oceanic state (Xie and Jin 2018); for group B models with cooler mean SST, the ascending branches are even more displaced to the west of WNP. Given much weaker intensity of CP El Niño, its related SSTA and Walker circulation anomalies might be more sensitive to the mean state of Pacific SST compared with that for

EP El Niño. It is also likely that group B's basic state can facilitate more upwelling of cold water over equatorial eastern Pacific due to stronger anomalous surface easterlies and therefore intense westward surface currents in the eastern Pacific (Samanta et al. 2018; Santoso et al. 2013), leading to westward advection of cold surface water and more westward-extended negative SSTA during CP El Niño. As a result, the CP-type SST warming is not found until farther west over the central-western Pacific in group B models. To summarize, the mean state of SST can strongly influence the ocean-atmosphere coupling processes which are in line with the concept of Bjerknes feedback. Cold tongue bias thus tends to be associated with stronger westward zonal current, which also give rise to a westward shift of El Niño-related SSTA (Xie and Jin 2018).

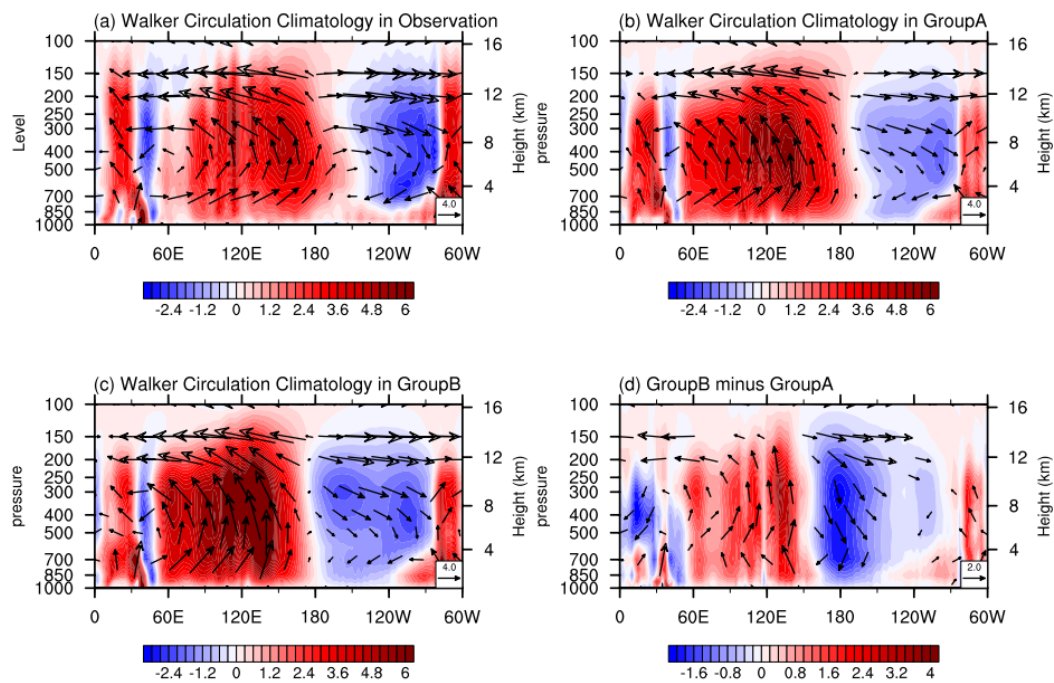


Figure 3.13 The (a) observed and (b, c) MME mean NDJFM climatology of 0° - 10° N averaged zonal divergent wind and pressure velocity (vectors; see scale arrow at bottom right in units of m/s) based on the models in (b) group A, (c) group B and (d) their differences. Shadings denote pressure velocity (units: Ps/s) which is multiplied by a factor of -100 for clarity. Only signals passing the 95% significance level are shown in (d).

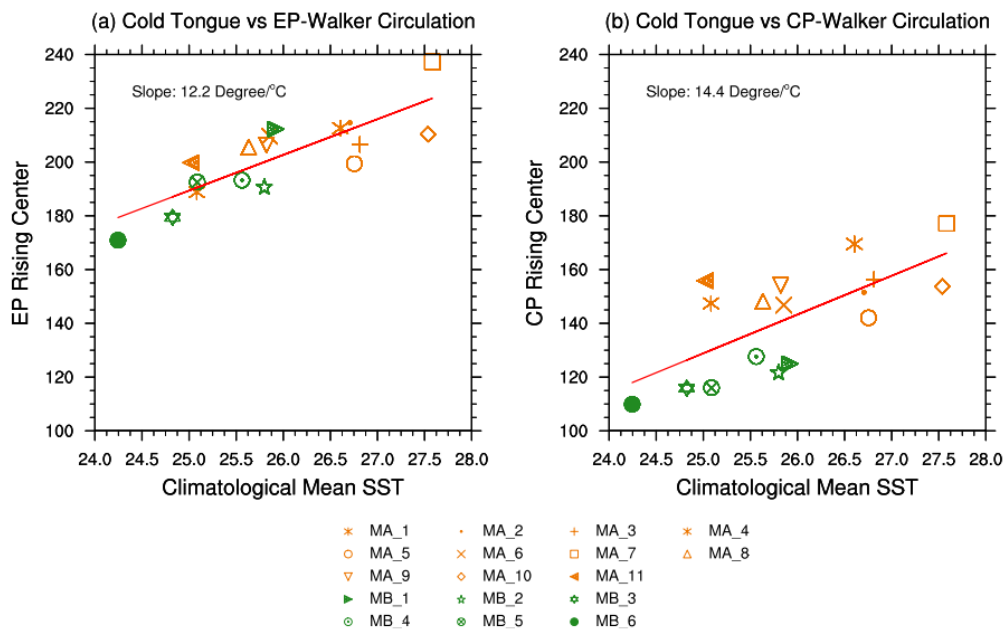


Figure 3.14 Scatterplots of the NDJFM climatological mean SST (units: $^{\circ}$ C) over the equatorial Pacific cold tongue (2° S– 2° N, 180° – 120° W) versus locations of the centroid of ascending motion associated with (a) EP and (b) CP El Niño-related overturning circulation. Orange (Green) markers indicate the models from group A (B).

3.4 Brief summary

We have investigated the performance of CMIP5 models in capturing the teleconnection between two types of El Niño and EA rainfall. By evaluating models' capability of simulating El Niño SST patterns and their related Walker circulation anomalies, it was found that while all of the 17 selected models can represent the EP El Niño-related anomalous atmospheric circulation with robust inter-model consistency of EP-type SSTA, some model members can give large biases in the same circulation elements when CP El Niño occurs due to lower skills in simulating CP-type SSTA. In particular, 11 out of 17 models (referred to as group A) can faithfully reproduce the Walker cell anomalies for both types of El Niño. For the remaining 6 models (referred to as group B), there is erroneous rising motion/upper-level divergence in the equatorial western Pacific related to CP El Niño. Further inspection showed that group A models can reproduce the observed CP-type cold-warm-cold SSTA pattern. On the other hand, in group B the eastern Pacific cold SSTA are too strong, and the adjacent warm oceanic signals cover the western Pacific (instead of the central Pacific as in observations). Such a westward shift of the CP-type SSTA explains the unrealistic upward motion at about 120°E in group B, which is to the west of the observed rising branch of the anomalous Walker cells. Thus, the SSTA plays a critical role in determining El Niño-related overturning atmospheric circulation in these models.

The model-simulated anomalous precipitation and low-level winds during two types of El Niño were further examined, focusing on the EA region during boreal summer. For both sets of models, suppressed (surplus) precipitation anomalies are found further west over equatorial WNP and eastern Indian Ocean (near the dateline) in JJA(0) during EP El Niño. With the formation and persistence of the Philippine Sea anticyclone, dryer (wetter)-than normal conditions over the Philippines and SCS (eastern coastal China) are well captured in

models during the EP El Niño mature phase and its ensuing seasons. The “Indian Ocean capacitor” effect in JJA(1) which gives rise to enhanced EASM rainfall is also reproduced. However, CP El Niño-related dryer (wetter)-than-normal conditions over SCS (at $\sim 150^{\circ}\text{N}$) from DJF(1) to JJA(1) can only be seen in group A. The other set of models tends to give cyclonic circulation in the low levels and surplus rainfall over SCS, which are unrealistic due to distinct location of Gill-type responses. Thus group A models can capture the EA circulation anomalies during both types of El Niño, while group B can reasonably reproduce impacts of EP El Niño, but not for CP El Niño.

Overall, results in this chapter highlight the challenge of simulating the El Niño-EASM teleconnection and its diversity in state-of-the-art coupled models. Even for models which can capture two types of El Niño variability, there is no guarantee that the impact of ENSO on the EA climate is reasonably represented. It was further demonstrated that CP El Niño and its teleconnection is very sensitive to the eastern Pacific cold tongue bias. Compared to group A, the colder mean SST and stronger Walker circulation over the eastern Pacific in group B might be conducive to even colder SSTA during CP El Niño, due to stronger local Bjerknes feedback. This might be the reason why there is a westward shift of CP El Niño-related SSTA, resulting in unrealistic WNP teleconnection and EASM circulation in group B models. More importantly, some of the CMIP5 models show high skill in capturing the El Niño-EA climate teleconnection and its diversity during the El Niño life cycle, and hence providing a basis for further inspections on their future changes which will be stressed in Chapter 4.

4 El Niño-EA Climate Teleconnection Under Global Warming

In Chapter 3, the performance of 17 models (see *Table 3.1*) in simulating the El Niño-Indo Pacific teleconnection was evaluated based on their historical runs. Under the influence of global warming, the teleconnection patterns might be modified. This chapter seeks to address the question of how El Niño-induced rainfall anomalies will be changed in a warmer climate and the underlying physical mechanisms. In particular, the MME mean teleconnection in the future climate under the RCP 8.5 scenario will be compared with that based on historical simulations. Moisture budget analyses will also be carried out, in order to further separate the effects due to perturbations of El Niño-related circulation anomalies and changes of the background moisture in the atmosphere.

4.1 Evaluation of EASM in CMIP5 models

Previously, it has been shown that the MME mean based on group A models can capture the El Niño-EA rainfall teleconnection (see Chapter 3). These models were selected mainly rely on their simulations of El Niño diversity and the related anomalous Walker circulation. To further focus on the El Niño-related EA rainfall variability, EASM and its variability in these models were evaluated. **Figure 4.1** shows the observed climatological mean precipitation and 850-hPa wind over the Indo-Pacific region for the JJA season. During boreal summer, the time-mean low-level Asian monsoon circulation is characterized by cross-equatorial wind over the western Indian Ocean, prevalent westerlies/southwesterlies from the Indian subcontinent to East Asia, and cyclonic flow features over the Bay of Bengal and SCS. At the same time, heavy monsoon rainfall is found over India, the foothills of the Himalayas,

Indochina, WNP and the EA Meiyu regions. To depict the recurrent circulation patterns associated with the EASM variability on the interannual time scale, regression of rainfall and 850-hPa wind onto the EASM index (see Chapter 2 for details) are computed (see **Figure 4.1c**). It can be seen that when EASM is strong, an anomalous low-level anticyclone is centered over the far western WNP. Consistent with positive moisture advection by its southwesterly wind branch, wetter-than-normal conditions to the west and northwest of the anticyclone are found, i.e. over the Yangtze River Valley, Korea peninsular and south of Japan. On the other hand, rainfall is suppressed over SCS, WNP and part of Vietnam; these locations are either close to the center of the anticyclone or experiencing reduced monsoon westerlies in the low levels (i.e. with anomalous easterly winds). The above is consistent with the well-known anti-correlation between EA and WNP summertime precipitation on the interannual timescale, which in turn is closely related to the east-west positioning of the subtropical high in this region (see Wang *et al.*, 2008).

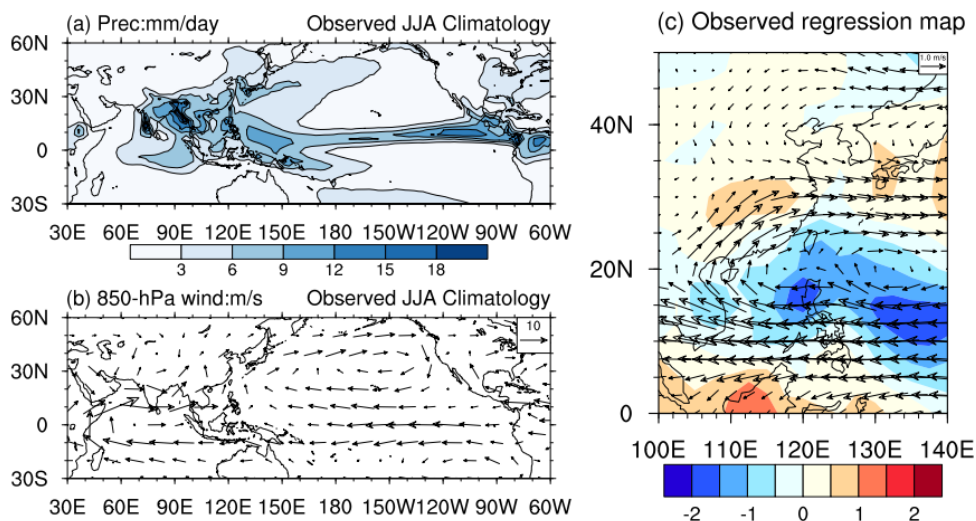


Figure 4.1 Climatology (1979-2014) of the JJA mean (a) precipitation and (b) 850-hPa wind.

(c) Regression of the JJA mean precipitation (shading; see scale bar at bottom in units of mm/day) and 850-hPa wind (vectors; see scale arrow at top right in units of m/s) onto the negative JJA mean EASM index. NCEP/NCAR reanalysis and GPCP data are used. See text for details.

To assess CMIP5 models' performance in capturing the EASM climatology and interannual variability, the same time averages and regression coefficients were computed using meteorological variables from simulations. Results are presented in **Figure 4.2** using Taylor diagrams (Taylor 2001a) (see more details about the interpretation of Taylor diagram in Appendix). Both the patterns as well as the magnitudes of the climatological precipitation and 850-hPa zonal wind from models compare well with their observational counterparts. In particular, the pattern correlation for both variables are within the range of 0.7 to 0.9 or higher, while the majority of values for the root mean square error (RMSE) which is normalized by the standard deviation of the corresponding observed field, is from 0.25 to about 1.0 (see **Figure 4.2a**). On the other hand, the pattern correlation (normalized RMSE) tends to be low (large) for the anomalous precipitation associated with EASM variability for many models (**Figure 4.2b**). Inspection of individual model's results revealed that the main bias lies in the erroneous location and/or magnitude of the anomalous rainfall pattern over the EA/WNP region (figures not shown). Thus, in spite of the reasonable time mean monsoon circulation in the simulated environments, models still have difficulties in capturing realistic interannually varying features of EASM.

The above results can be used to select models which can capture both the time mean and interannual variations of the EASM circulation. In particular, models are chosen whenever the following criteria are all satisfied: (i) the pattern correlation between simulated and observed JJA mean precipitation (U850) is above 0.90 (0.70); (ii) normalized RMSE of JJA mean precipitation and U850 is lower than 1.00; (iii) the regression pattern of precipitation (U850) onto the EASM index from simulations, and that based on observations, are correlated at a value of 0.60 (0.85) or above; (iv) normalized RMSE of the precipitation (U850) regression map is below 1.20 (0.75). Applying these criteria, out of those 17 models considered in Chapter 3, nine models are found to be able to represent both ENSO diversity

as well as EASM variability in their historical runs. They are ACCESS1-0 (M_1), ACCESS1-3 (M_2), bcc-csm1-1-m (M_3), CCSM4 (M_4), CESM1-BGC (M_5), CESM1-CAM5 (M_6), CNRM-CM5 (M_7), FIO-ESM (M_8) and HadGEM2-ES (M_9). Note that in this chapter, these models are named as M_1-M_9 (which is different from the labels of M1-M17 used in Chapter 3). **Figure 4.3** shows the MME mean, based on these nine models, of low-level wind and precipitation in JJA over the Indo-Pacific region, as well as the anomalous circulation related to EASM variations. The climatological boreal summer precipitation (**Figure 4.3a**) and low-level wind (**Figure 4.3b**) are seen to be reasonably captured in the MME average. Rainfall over the subtropical WNP region (the EA Meiyu region), however, is overestimated (underestimated) by the models. This seems to be a feature commonly found in model-simulated EASM (Sperber et al. 2013). Models also tend to be anomalously dry at the equator west of the dateline, associated with a split ITCZ (Wittenberg et al., 2006; Li and Xie, 2014). Regarding the EASM interannual variability, the MME mean anomalous precipitation and 850-hPa winds greatly resemble the observed (with pattern correlations of 0.89 and 0.97, and RMSE of 0.60 and 0.23, for precipitation and U850 respectively). Overall, it is seen that the EA summertime circulation as well as its interannual variability are well represented by these selected models. In addition, the observed and MME mean EP (CP) El Niño SST patterns, found based on the leading EOFs of tropical Pacific SSTA (figures not shown), have pattern correlation of 0.96 (0.85).

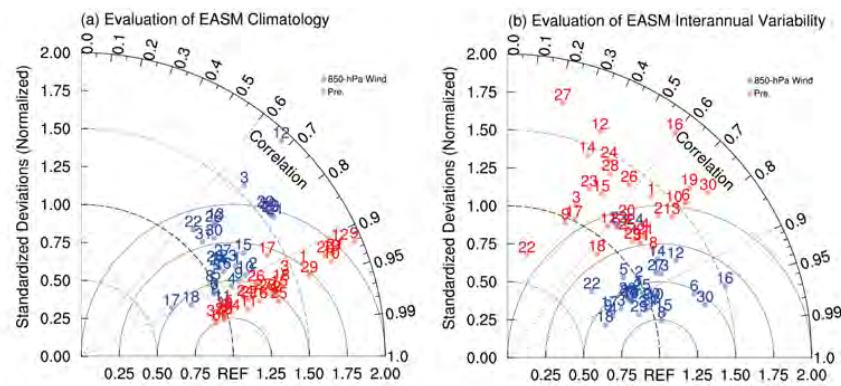


Figure 4.2 Taylor diagrams of (a) JJA climatology and (b) interannual variability of precipitation (red circles) and 850-hPa zonal wind (blue circles) for historical runs from 31 CMIP5 models (see **Table 2.1**). Model results are calculated for the region of 0°–50°N, 100°E–140°E, based on the period of 1949–2000. Regression maps of the precipitation and 850-hPa zonal wind onto the EASM index are used to represent the interannual variability of EASM in models

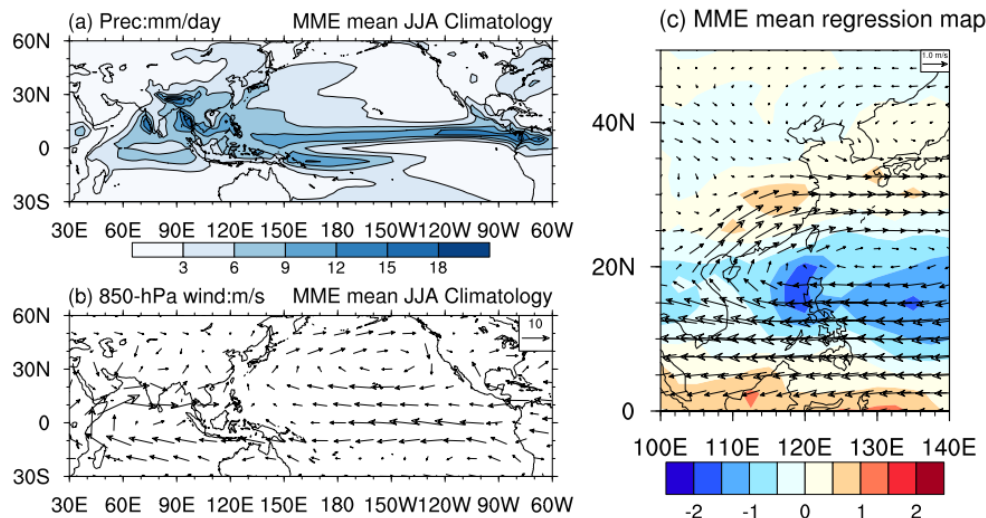


Figure 4.3 Same as **Figure 4.1**, but for the MME mean based on the selected CMIP5 models.

In Chapter 3, it was shown that simulated overturning circulation related to CP El Niño exhibits large inter-model variations. In particular, ACCESS1-0, ACCESS1-3 and HadGEM2-ES give significant westward drift of the rising branch location of the anomalous Walker circulation during CP El Niño, but not for the remaining six of the selected models, i.e. bcc-csm1-1-m, CCSM4, CESM1-BGC, CESM1-CAM5, CNRM-CM5 and FIO-ESM. To inspect the atmospheric circulations during El Niño in these nine models, **Figure 4.4** gives the simulated 0°–20°N averaged DJF stream function composites during two types of El Niño based on their historical runs. Consistent with the previous results, anticyclonic circulation anomalies dominate the regions from the Indian Peninsula to WNP in all the selected models during EP El Niño. However, the cyclonic flow centers (negative stream function anomalies) during CP El Niño are clustered near South China Sea for M_1, M_2 and M_9, but over WNP for other models. As such, the nine selected models can be further separated into two groups, namely group A-1 (B-1) which is a subset of group A (B) including bcc-csm1-1-m, CCSM4, CESM1-BGC, CESM1-CAM5, CNRM-CM5, and FIO-ESM (ACCESS1-0, ACCESS1-3 and HadGEM2-ES). Indeed, the MME mean anomalous stream functions based on both group A-1 and group B-1 resemble the observed during EP El Niño (see **Figure 4.5a, 4.5c, 4.5e**). However, during CP El Niño, group B-1 models tend to give westward shifted cyclonic circulation anomalies, in comparison with group A-1, and also with observations. In summary, the group A-1 models are able to simultaneously reproduce both El Niño diversity and El Niño-induced circulation anomalies over EA. To study how global warming might influence the El Niño-EA rainfall teleconnection, models in group A-1 are considered in the subsequent analyses.

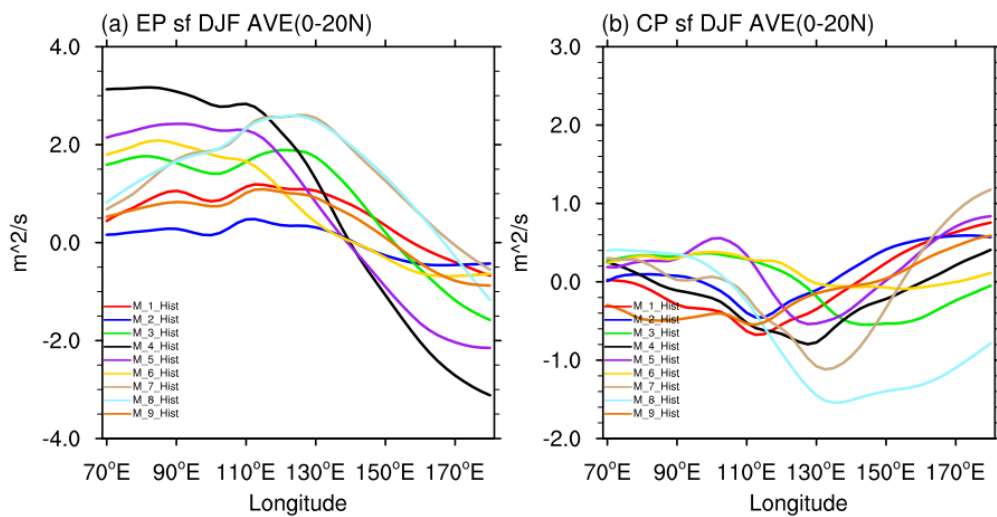


Figure 4.4 0° – 20°N DJF averaged (a) EP and (b) CP El Niño-related stream function anomalies (units: $10^6 \text{ m}^2 \text{ s}^{-1}$) over the region (70°E – 180°E) based on the nine selected models' historical simulations.

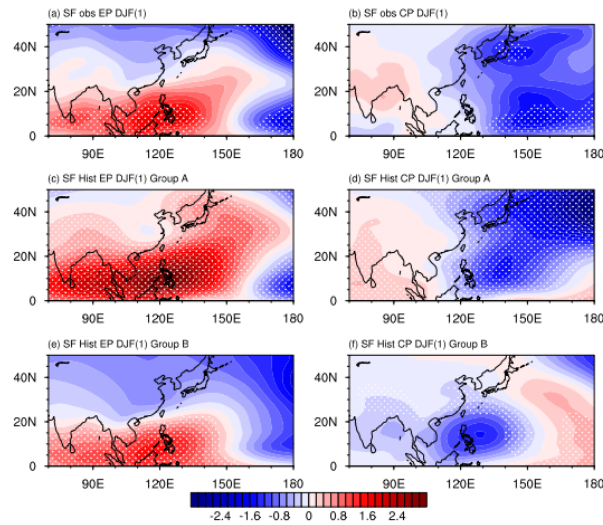


Figure 4.5 Composite stream function (shading; see scale bar at bottom in units of $10^6 \text{ m}^2 \text{ s}^{-1}$) anomalies based on (a), (b) observations, (c), (d) MME mean of models in group A and (e), (f) group B during DJF (1) for (a, c, e) EP and (b, d, f) CP El Niño. White dots indicate

stream function anomalies passing the 90% significance level.

4.2 Future changes of El Niño-EA rainfall teleconnection

To compare the present-day with the future El Niño-EA rainfall teleconnection, **Figure 4.6** and **Figure 4.7** give the evolution of group A-1 MME mean EA precipitation and low-level wind anomalies during the whole El Niño cycle, based on their historical runs and RCP 8.5 simulations, respectively. In general, the anomalous rainfall and low-level wind patterns and the corresponding seasonal evolutions under both scenarios are rather similar. Not surprisingly, they also resemble the patterns and seasonal evolutions generated from 11 models as shown in Chapter 3 (see middle columns in **Figure 3.9** and **Figure 3.10**). In addition, the major suppressed/surplus (anticyclonic/cyclonic) rainfall (wind circulation) anomalies are still significant at the 0.1 level. Note that there is significant change in the El Niño-related circulation strength. This implies that the influence of global warming on the El Niño-related EA circulation and precipitation is more obvious in their intensity but not their patterns. **Figure 4.8** shows the difference between composite maps for the future projections and historical runs. Under global warming, stronger westerly anomalies are found from Indochina to WNP accompanying drier (wetter) conditions over the Maritime Continent (WNP) during the developing summer of EP El Niño (see **Figure 4.8a**). There are stronger anomalous southeasterlies, together with drier (wetter) conditions near the Philippines and SCS (the southern and eastern China) during EP El Niño winter (**Figure 4.8e**). Wetter (drier) conditions can also be seen over the Maritime Continent (WNP) during the decaying summer of EP El Niño, with stronger easterly anomalies near the Philippines (**Figure 4.8i**), and drier conditions over Meiyu rainband. In MAM(1), a slightly weakened circulation is found over coastal EA to south of Japan (**Figure 4.8g**). However, no robust EP El Niño wind circulation pattern changes are found for the SON(0) (**Figure 4.8c**). For CP El Niño, the anomalous

rainfall pattern is amplified with stronger cyclonic circulation anomalies over the Philippines during DJF(1) (**Figure 4.8f**). During JJA(1), stronger westerlies over the western Pacific lead to wetter conditions locally, while Maritime Continent becomes even drier (**Figure 4.8j**). Thus, during CP El Niño the anomalous rainfall will be intensified significantly in DJF(1) and JJA(1). Similar to EP El Niño, changes of anomalous rainfall and low-level wind for CP El Niño are not as robust during SON(0) and MAM(1).

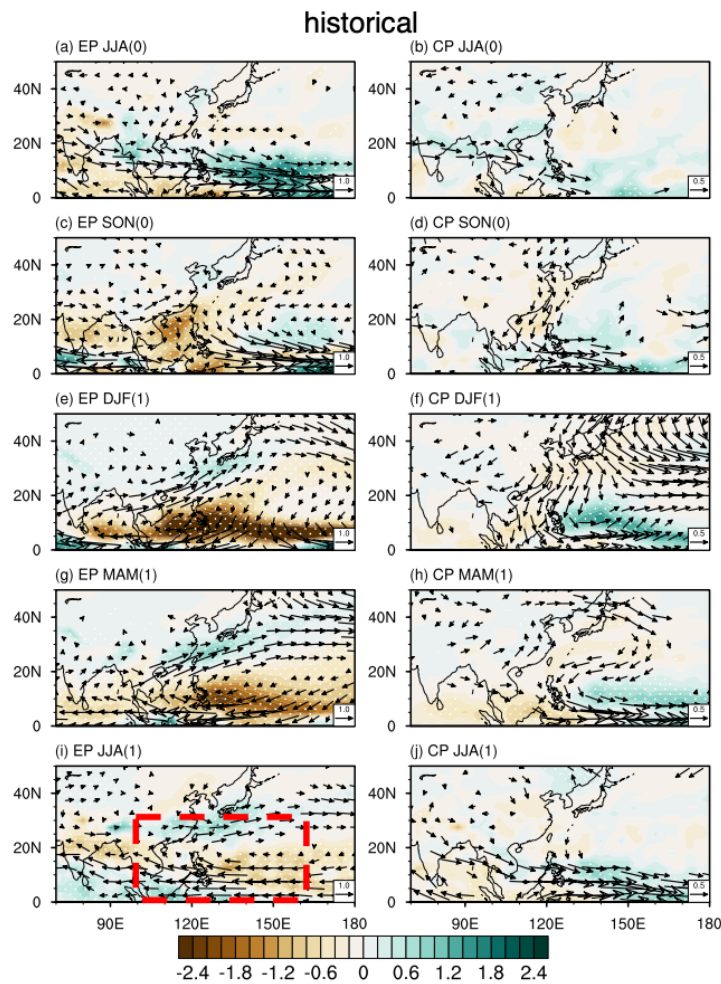


Figure 4.6 Composite precipitation (shading; see scale bar at bottom in units of mm/day) and 850-hPa wind (vectors denoting signals passing the 90% significance level; see scale arrow at bottom right in units of m/s) anomalies during (a), (b) JJA (0), (c), (d) SON (0), (e), (f) DJF (1), (g), (h) MAM (1), and (i), (j) JJA (1) for (a, c, e, g, i) EP and (b, d, f, h, j) CP El Niño based on the MME mean from group A-1 models' historical simulations. White dots indicate precipitation anomalies passing the 90% significance level. Red rectangle represents the region for calculating area-integrated absolute value of rainfall anomalies.

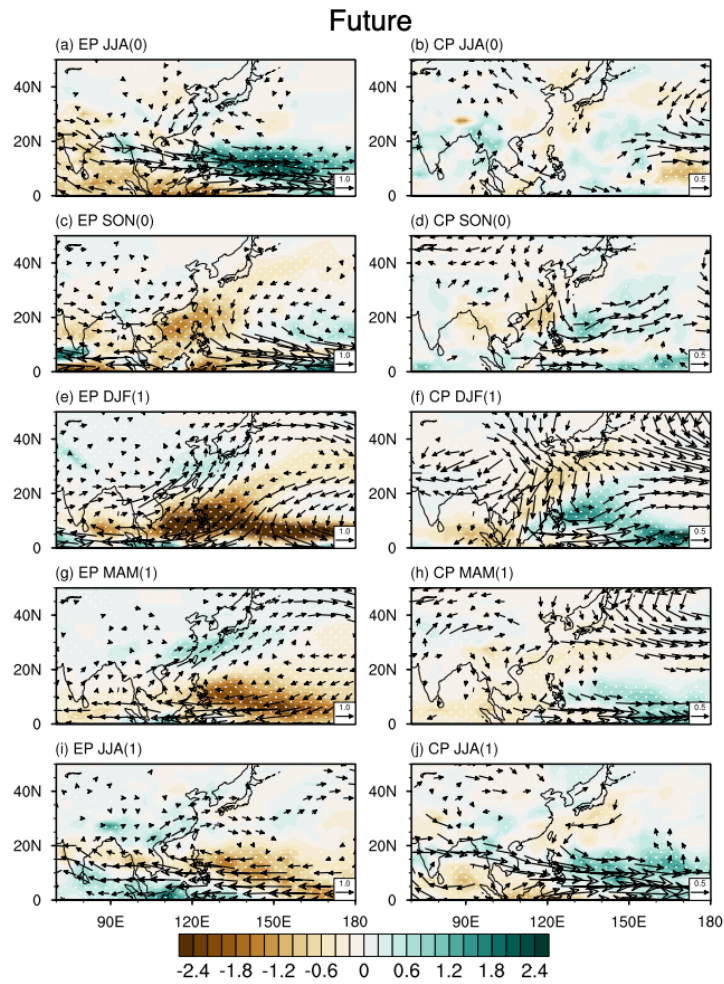


Figure 4.7 Same as **Figure 4.6**, but from group A-1 models' RCP 8.5 scenario simulations.

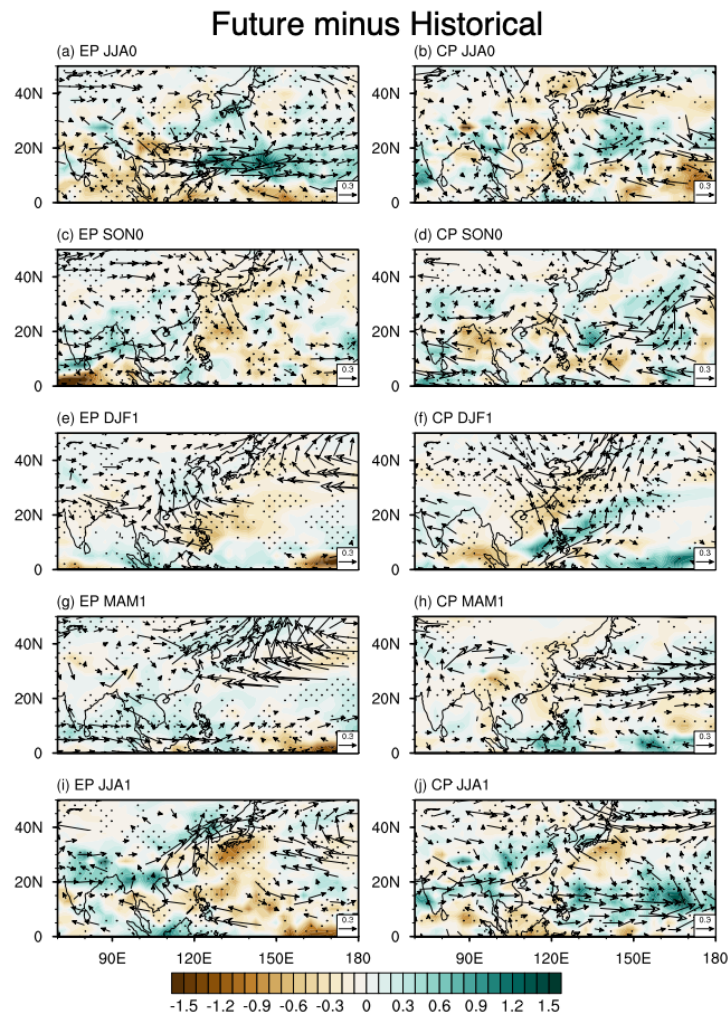


Figure 4.8 Same as Figure 4.6, but the differences between group A-1 models' RCP 8.5 scenario and historical simulations. Black dots indicate precipitation differences passing the 90% significance level.

The abovementioned results are based on the MME mean of the selected models, and thus the projected changes of El Niño-related circulation anomalies might rely on the selection of models. To inspect the future changes in individual models, **Figure 4.9** gives the 5° N–5°S averaged SSTA and 0°–20°N averaged stream function anomalies based on the corresponding composite maps during DJF(1) (i. e. El Niño mature phase) from the nine selected models. Under present-day and future climate, the locations of EP El Niño-related positive SSTA are consistent among these models (**Figure 4.9a**), albeit with inter-model variations in terms of its magnitude; for CP El Niño, the warming SSTA can be located over the central Pacific (far western Pacific) in group A-1 (B-1) models, which are consistent with our previous results in Chapter 3 (**Figure 4.9b**). The EP (CP) El Niño-related anticyclonic (cyclonic) circulation anomalies over the WNP can also be well captured in these models (see **Figure 4.9c, d** for details). Comparing the RCP8.5 scenario and historical results, it is obvious that some models (e.g. M_2 and M_6) tend to simulate stronger El Niño in the future climate, while weaker El Niño for some models (e.g. M_3 and M_4). Note also that the El Niño-related warming centers can be shifted under global warming. The abovementioned inconsistency of future El Niño changes will give rise to the inter-model spread of changes of the anticyclonic/cyclonic circulation anomalies.

To quantify the intensity and location change of circulation/SST signals associated with the two El Niño flavors, the centroid of SSTA and 850-hPa stream function is, defined as:

$$X = \frac{\int SSTA(x)xdx}{\int SSTA(x)dx} \quad (4.1)$$

$$Y = \frac{\int \psi(x)xdx}{\int \psi(x)dx} \quad (4.2)$$

(where $SSTA(x)$ ($\psi(x)$) denotes the equatorial SSTA (anomalous stream function) averaged over 5° N–5°S (0°–20°N) in DJF(1), x being the longitude, and the zonal integration covering 120°E–90°W (90°E–150°E)), were computed. To interpret the magnitude of El Niño (El

Niño-related EA/WNP circulation anomalies), the value of SSTA (stream function) evaluated at X (Y) was used. **Figure 4.10** gives changes of magnitudes and locations of SSTA vs. anomalous stream function, for EP and CP El Niño. Inspection of the individual models reveals no consensus in these changes; there are also large model spreads of SSTA and anomalous stream function differences for both types of El Niño. Hence the MME mean values become rather small due to mutual cancellation between model signals. On the other hand, note that El Niño-induced low-level circulation changes under global warming follow those of the strength and location of El Niño SSTA (**Figure 4.10**). The correlation between SSTA and stream function magnitude changes for EP (CP) El Niño is 0.823 (-0.7); the correlation between their location changes is 0.4 (0.7) for EP (CP) El Niño. These results indicate changes of El Niño-driven circulation anomalies are strongly related to those in the SSTA in each individual model.

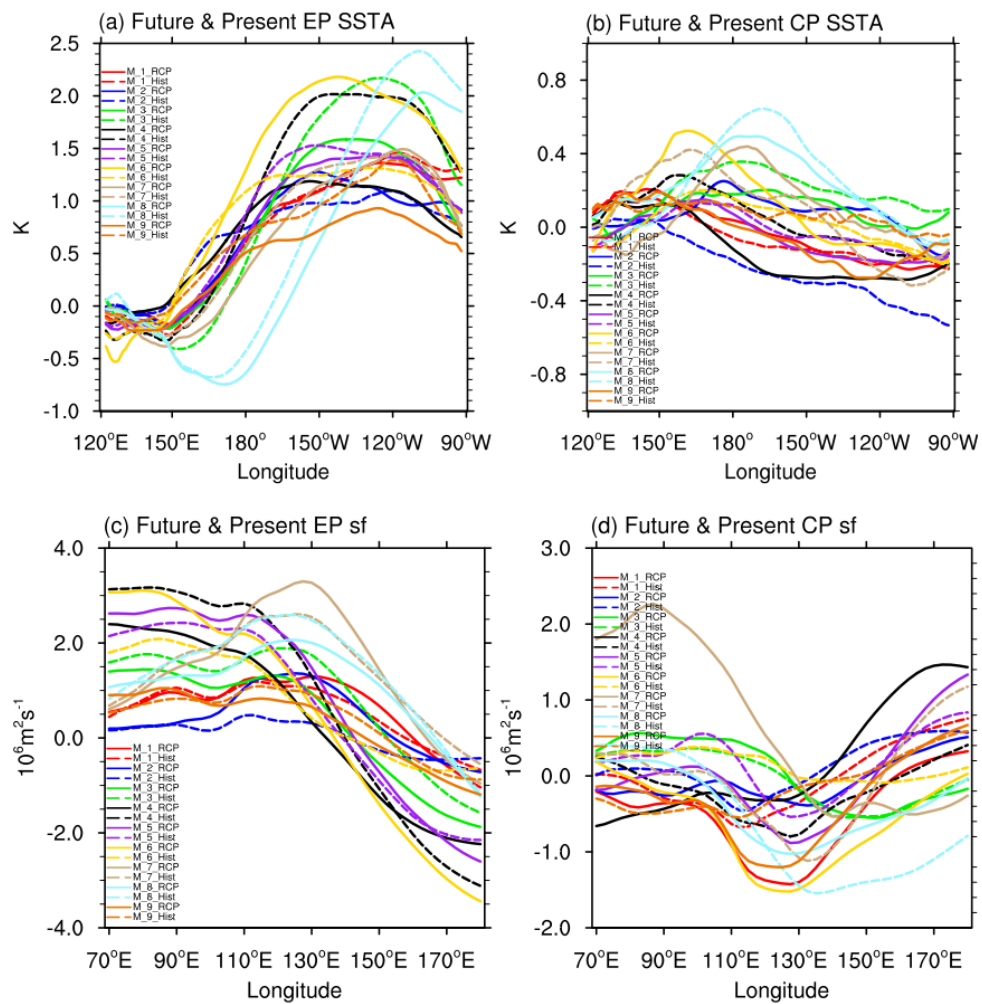


Figure 4.9 (a, b) Five points running mean of $5^{\circ}N$ – $5^{\circ}S$ DJF averaged SSTA (units: K) and (c, d) 0° – $20^{\circ}N$ DJF averaged stream function anomalies (units: $10^6 m^2 s^{-1}$) from the composite maps of (a, c) EP and (b, d) CP El Niño events in the 9 selected models.

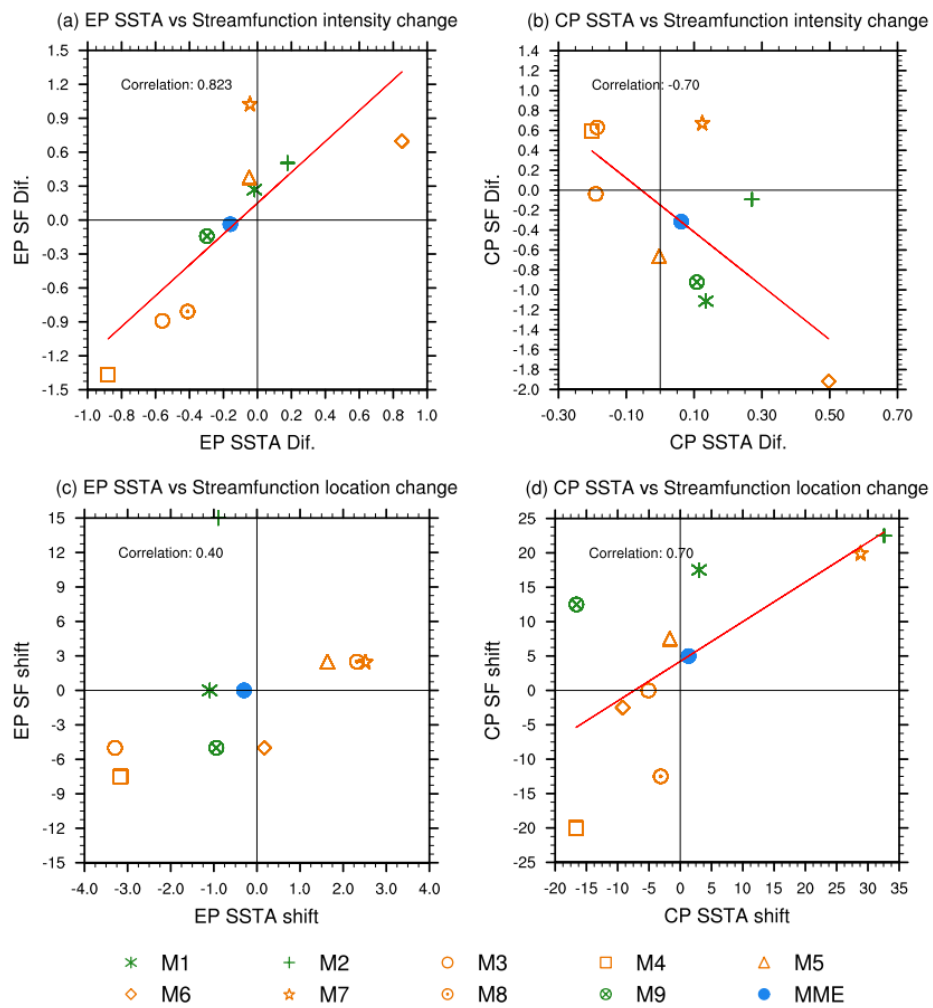


Figure 4.10 Scatter plots of (a, b) El Niño-related SSTA differences (units: K) and stream function differences (units: $10^6 \text{ m}^2 \text{ s}^{-1}$); (c, d) El Niño-related warming location changes (units: $^\circ$) and stream function location changes between RCP 8.5 scenario and historical outputs, for (a, c) EP and (b, d) CP El Niño, in group A-1 (markers in orange) and B-1 (markers in green). The blue dots indicate the MME mean based on all the nine selected models.

Finally, area-integrated absolute values of the rainfall anomalies, defined as $\iint P' \hat{P}' dx dy = \iint |P'| dx dy$ (see section 2.2.3 for details), were computed based on the MME mean of group A-1 models by summing the corresponding values over the region of (0°–30°N, 100°E–160°E) (see red rectangle in **Figure 4.6**); these quantities (see green and blue bars in **Figure 4.11**) can represent the magnitude of El Niño-induced teleconnection pattern. Note that the area-integrated absolute value of rainfall anomalies, in general, is proportional to the number of grid points over the selected region. Detailed results are shown in **Figure 4.11**, together with the fractional change from the present to the future climate. The anomalous rainfall during the JJA(0), DJF(1) and JJA(1) related to EP El Niño is enhanced significantly in the future climate. For CP El Niño, significant increase of the anomalous rainfall amplitude is clearly seen in DJF(1) and JJA(1). The aforementioned changes are consistent with those shown in **Figure 4.8**. It is also noteworthy that changes of CP El Niño-related rainfall due to global warming, in general, are even more robust compared with these for EP El Niño.

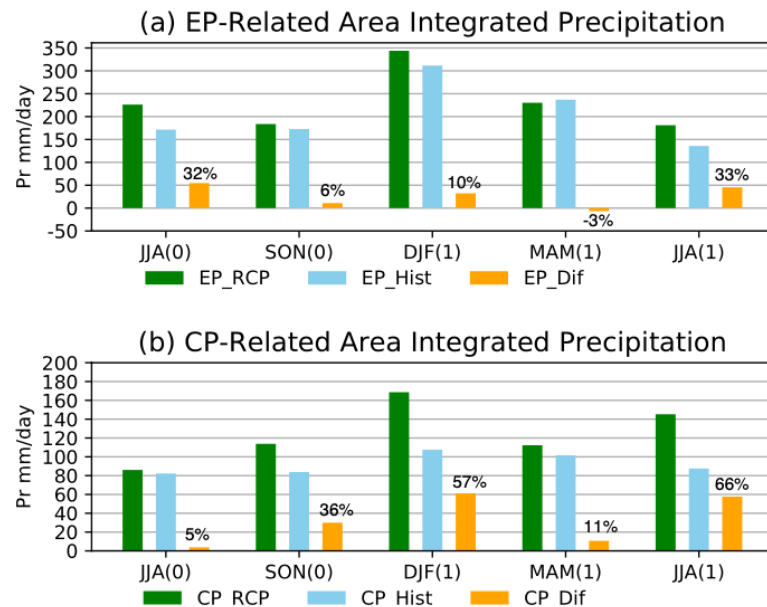


Figure 4.11 Bar charts of the (a) EP El Niño-related and (b) CP El Niño-related spatial integrated absolute values of rainfall anomalies over the region of (0° – 30° N, 100° E– 160° E) during the whole seasonal cycle based on (green bar) RCP 8.5 scenario simulations, (blue bar) historical simulations and (yellow bar) their differences. The fractional changes are denoted on top of the yellow bar (see text for more details).

Furthermore, **Figure 4.12** depicts El Niño SSTA intensity changes (same as in **Figure 4.10**) vs. area-integrated rainfall amplitude changes during DJF(1) based on the nine selected models. For models with strongly enhanced (weakened) EP El Niño intensity, the rainfall amplitudes in these models tend to be enhanced (weakened). For models with moderate EP El Niño intensity changes, (i.e. slightly stronger or weaker), the anomalous rainfall magnitudes are intensified in the future climate, regardless of the change of sign of EP El Niño strength. For CP El Niño, stronger rainfall spatial variations are seen in the future projections for all of these models with slightly stronger or weaker CP El Niño amplitude changes. To summarize, the CP El Niño-driven rainfall variability will be enhanced under a warmer climate, same for EP El Niño unless its amplitude is strongly suppressed in the future due to global warming. To understand how a warmer background climate might influence rainfall variability related to two types of El Niño, and the contribution of various circulation elements, results of moisture budget analyses will be shown in the next section.

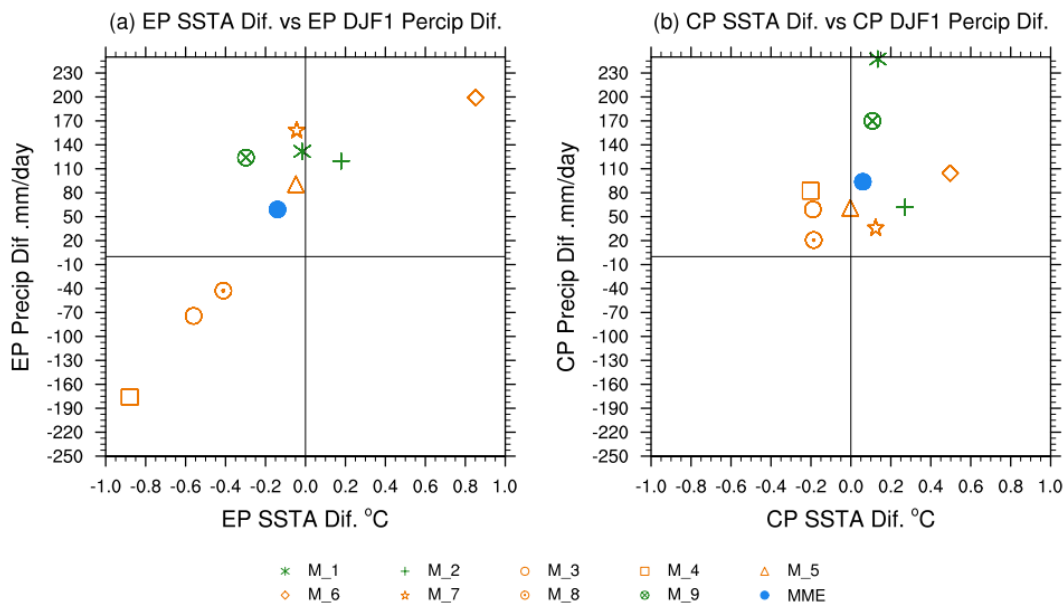


Figure 4.12 Scatter plots of El Niño-related SSTA intensity changes (units: °C) and anomalous rainfall spatial variation changes (units: mm/day) for (a) EP and (b) CP El Niño, based on RCP 8.5 scenario and historical simulations from models in group A-1 (markers in orange) and B-1 (markers in green). The blue dots indicate the MME mean based on all the nine selected models.

4.3 Moisture budget analyses

The total vertically integrated moisture flux and its convergence from the selected models, based on the historical runs and RCP 8.5 scenario projections for the two types of El Niño, are depicted in **Figure 4.13** and **Figure 4.14**. It is seen that the moisture flux patterns resemble those of anomalous low-level wind as shown in **Figure 4.6** and **Figure 4.7**. Comparing **Figure 4.13** with **Figure 4.14**, the patterns of moisture flux and its convergence are very similar. There is obvious change of magnitude in the convergence/divergence signal, which coincides with future changes of rainfall anomalies at the same location. Contributions of dynamic and thermodynamic effects to the total moisture flux convergence are now considered (see equation A1.2 for more details). **Figure 4.15** and **Figure 4.16** give the moisture flux convergence component due to the dynamic term. As expected, the total moisture flux convergence during El Niño events is mainly driven by this term ($-\frac{1}{g\rho_w} \int_{p_s}^{p_t} \nabla \cdot (q_c \vec{V}) dp$) in both simulations, with high resemblance (compare **Figure 4.13** with **Figure 4.15**). This is true for both the historical and RCP 8.5 scenario simulations. The thermodynamic terms are shown in **Figure 4.17** and **Figure 4.18**. Compared with the dynamic term, the thermodynamic component and its convergence exhibit a rather complex pattern and bear little resemblance with the total term, and is also much weaker.

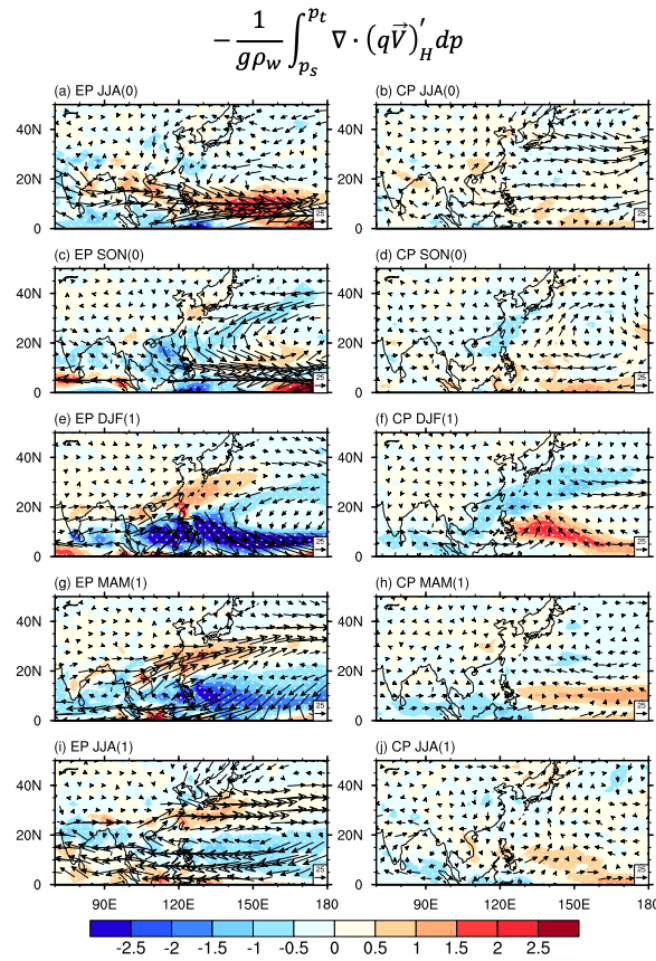


Figure 4.13 Composite vertically integrated moisture convergence contributing to the anomalous rainfall (shading; see scale bar at bottom in units of mm/day) and the corresponding moisture flux transport (vectors; see scale arrow at bottom right in units of $\text{kg m}^{-1} \text{s}^{-1}$) anomalies during (a), (b) JJA (0), (c), (d) SON (0), (e), (f) DJF (1), (g), (h) MAM (1), and (i), (j) JJA (1) for (a, c, e, g, i) EP and (b, d, f, h, j) CP El Niño based on the MME mean from group A-1 models' historical simulations. White dots indicate moisture convergence anomalies passing the 90% significance level.

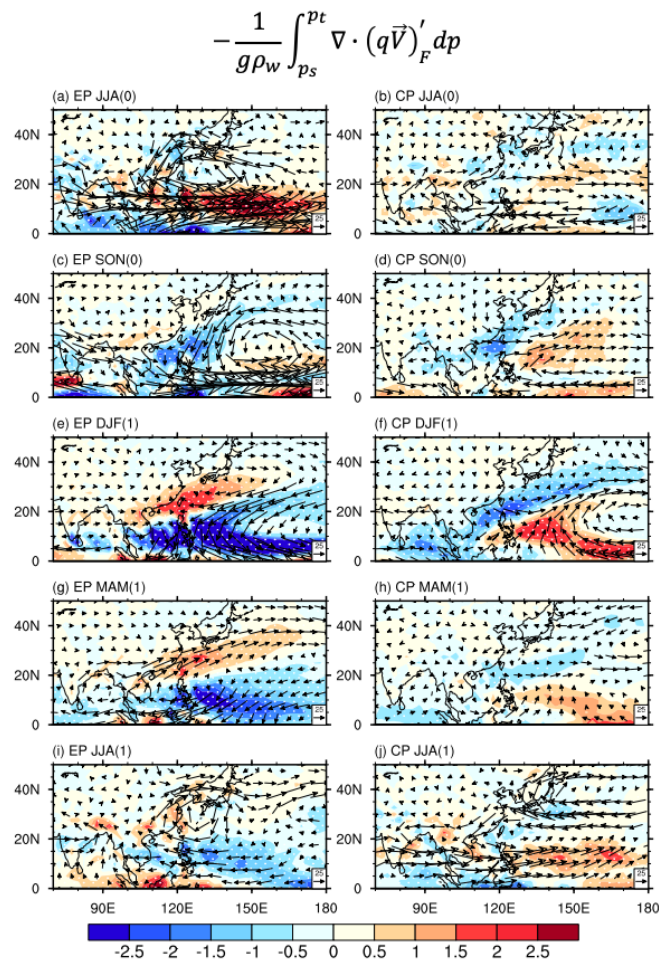


Figure 4.14 Same as **Figure 4.13**, but for RCP 8.5 scenario.

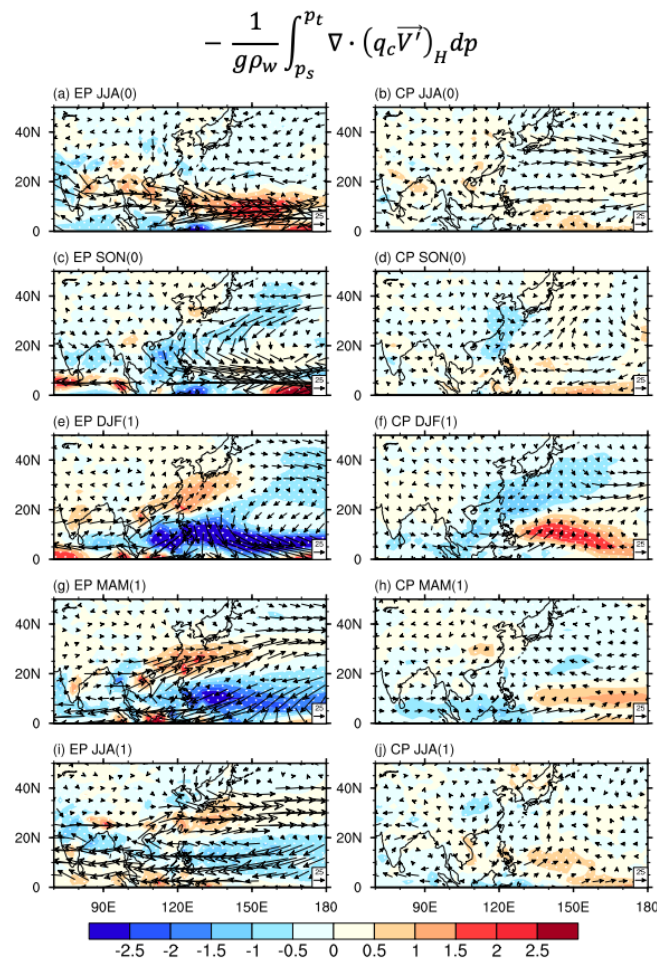


Figure 4.15 Same as **Figure 4.13**, but for moisture convergence and moisture flux transport due to dynamic effect.

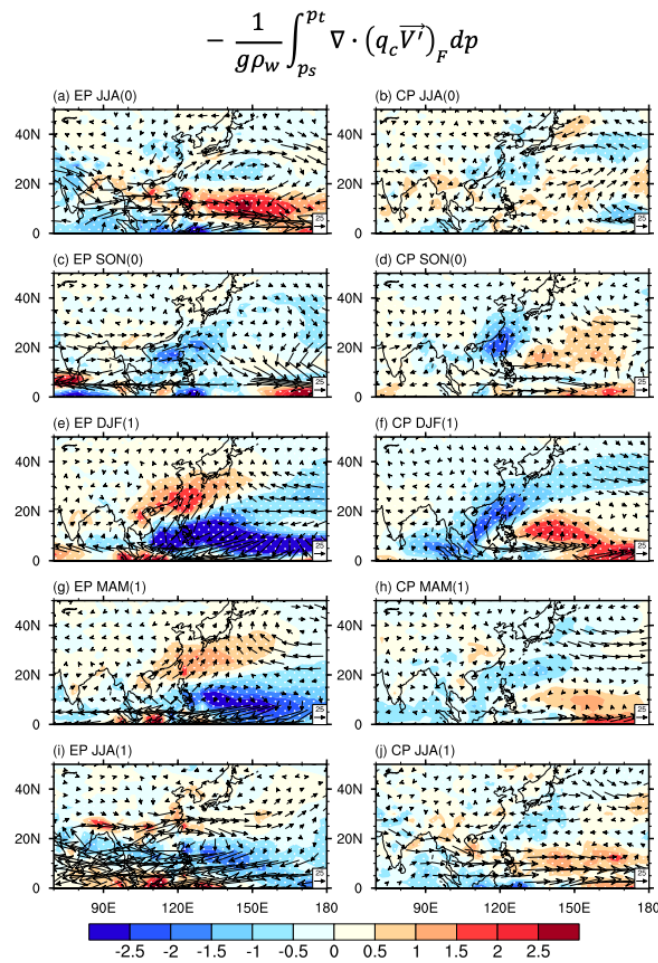


Figure 4.16 Same as **Figure 4.15**, but for RCP 8.5 scenario.

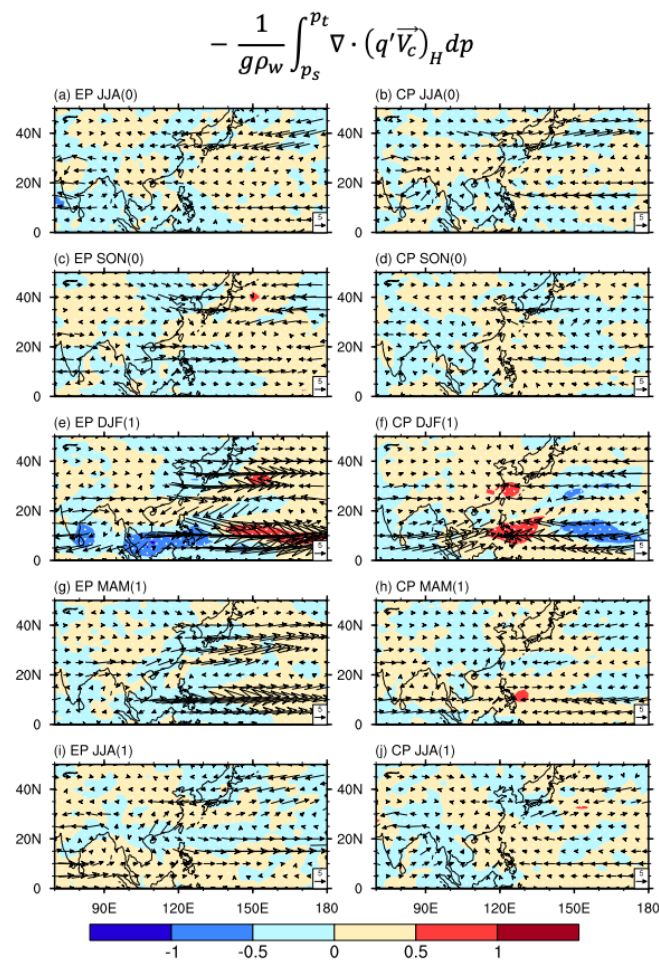


Figure 4.17 Same as **Figure 4.13**, but for moisture convergence and moisture flux transport due to thermodynamic effect.

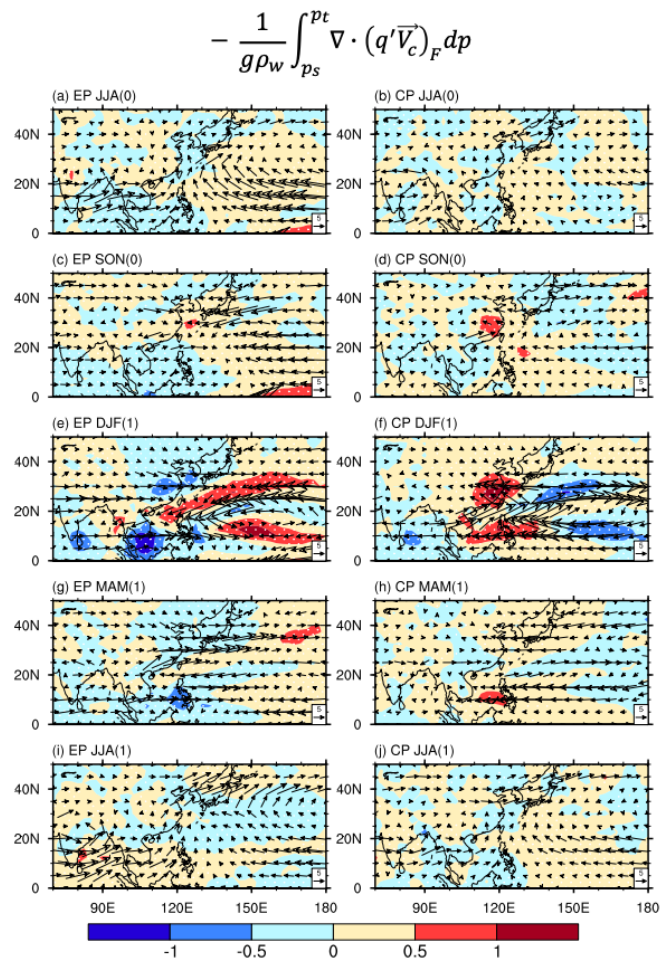


Figure 4.18 Same as **Figure 4.17**, but for RCP 8.5 scenario.

To quantify future change of moisture flux convergence, as well as those due to the dynamic and thermodynamic component, different terms calculated according to equation A1.7 are shown in **Figure 4.19**. The change of spatially integrated moisture flux convergence projected onto \hat{P}' is highly consistent with the change of rainfall amplitude (see leftmost and rightmost bars for each season in **Figure 4.19**). Again the dynamic effect is the dominant term, especially in JJA(0), DJF(1) and JJA(1) during EP El Niño and in DJF(1) and JJA(1) during CP El Niño. These are also the seasons in which significant change in rainfall amplitudes is found. Further decomposition into effects due to perturbations of El Niño-

related circulation anomalies, and changes in the background moisture, is given in **Figure 4.20**. During EP El Niño, the increase of mean moisture in a warmer climate can give a positive contribution and enhance moisture flux convergence, resulting in intensified rainfall anomalies. However, the effect of perturbed EP El Niño-related circulation may vary according to the season. For JJA(0) and JJA(1), it has a positive contribution, indicating an increase of the circulation anomalies. While for other seasons, it has a negative contribution (**Figure 4.20a**). During CP El Niño, positive effect due to the increased mean moisture will also intensify the rainfall variability for the whole El Niño cycle. As for the effect due to circulation change, it gives positive contribution in DJF(1) and JJA(1), but negative for MAM(1) (**Figure 4.20b**). (Note that the CP El Niño-related circulation anomalies are not significant during JJA(0); their future changes and their impacts on the moisture budget will not be discussed here.) To further examine perturbations of El Niño-related circulation changes and their relationship with oceanic changes, maps of perturbed SSTA in a warmer climate are plotted in **Figure 4.21**. For EP El Niño, the warm SSTA in the eastern Pacific is weakened from JJA(0) to DJF(1), accompanied with cooler anomalies in the IO. This indicates weaker EP El Niño during its mature phase, which is consistent with a weaker moisture transport as a result to circulation changes in DJF(1) (**Figure 4.21e**). The EP El Niño-related warming during MAM(1) in the eastern Pacific and IO will be weaker in the future, according to the RCP 8.5 scenario as simulated by group A-1 models (**Figure 4.21g**). This might be related to the anomalous westerlies in **Figure 4.8**, indicating a weaker WNP anticyclonic circulation. In JJA(1) of EP El Niño, IO warming is slightly weaker, but with a stronger reversal to much cooler SSTA (**Figure 4.21i**). The significantly colder SSTA anomalies near the central Pacific may trigger anomalous easterlies near the western Pacific, the Philippines and Maritime Continent, strengthening the anticyclonic circulation anomalies over the WNP region (**Figure 4.8i**). During the DJF(1) for CP El Niño, SSTA changes with

cooler (warmer) conditions in SCS (western Pacific), tend to intensify the circulation anomalies in DJF(1) by inducing a cyclonic flow near the Philippines (**Figure 4.21f**). It is also noteworthy that the circulation changes in JJA(1) of CP El Niño is evident but with insignificant SSTA changes (**Figure 4.21j**). This might result from a stronger response of the low-level circulation anomalies to the SSTA in a warmer climate which warrants further studies. To sum up, the positive contributions of the increased mean moisture tend to offset the negative effects due to weaker circulation anomalies, leading to the amplified rainfall anomalies in most seasons during El Niño events. In other words, notwithstanding the inter-model variations of the future El Niño-related circulation, a warmer climate supplying more moisture in the atmosphere, can induce more variable rainfall during two types of El Niño.

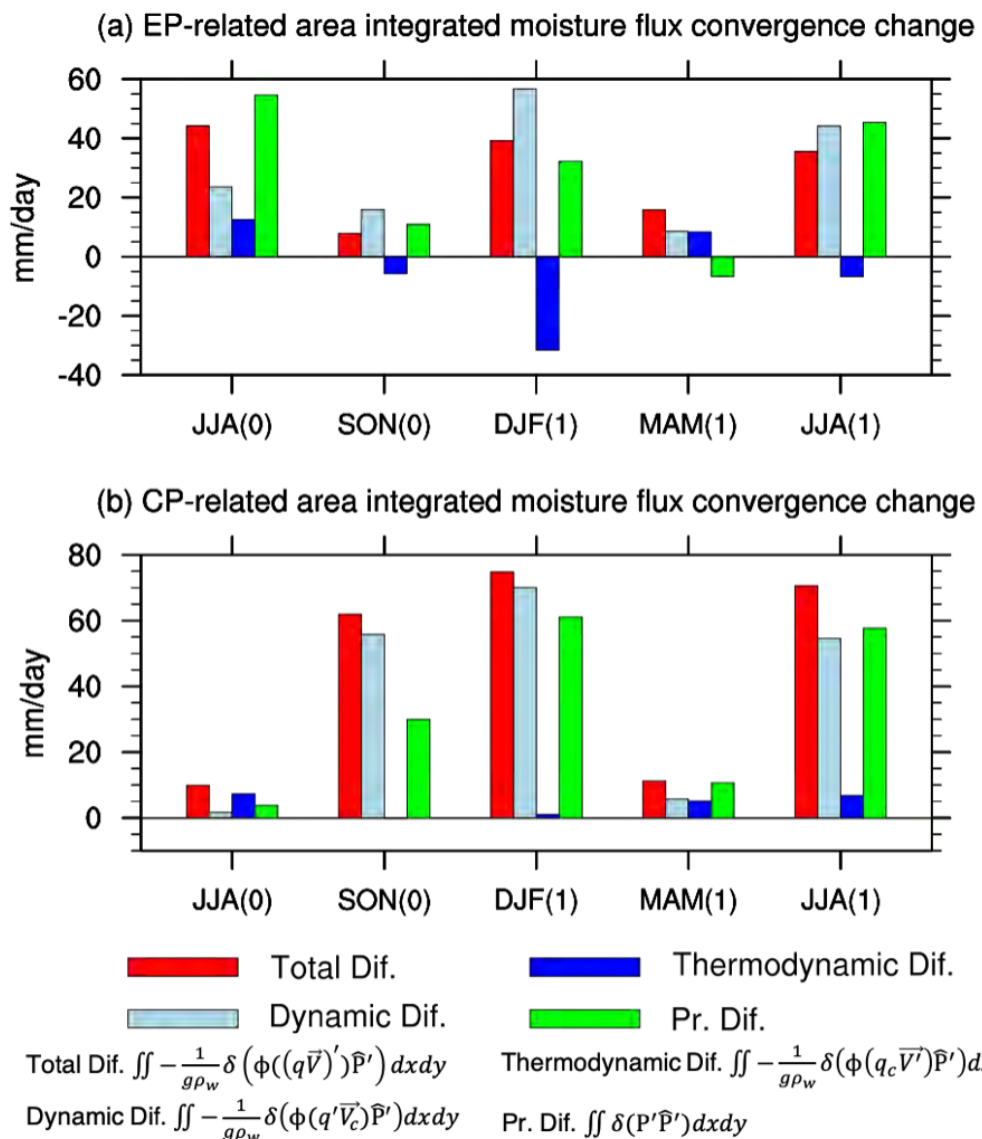


Figure 4.19 The future changes of (a) EP and (b) CP El Niño-related spatially integrated total moisture flux convergence (red bar), dynamic term (light blue bar), thermodynamic term (blue bar) and rainfall anomalies (green bar) which are projected onto \hat{P}' (units: mm/day) during the whole cycle of El Niño events. Note that $\phi(\cdot) = \nabla \cdot \int_{p_s}^{p_t} (\cdot) dp$ is defined in Appendix for simplicity.

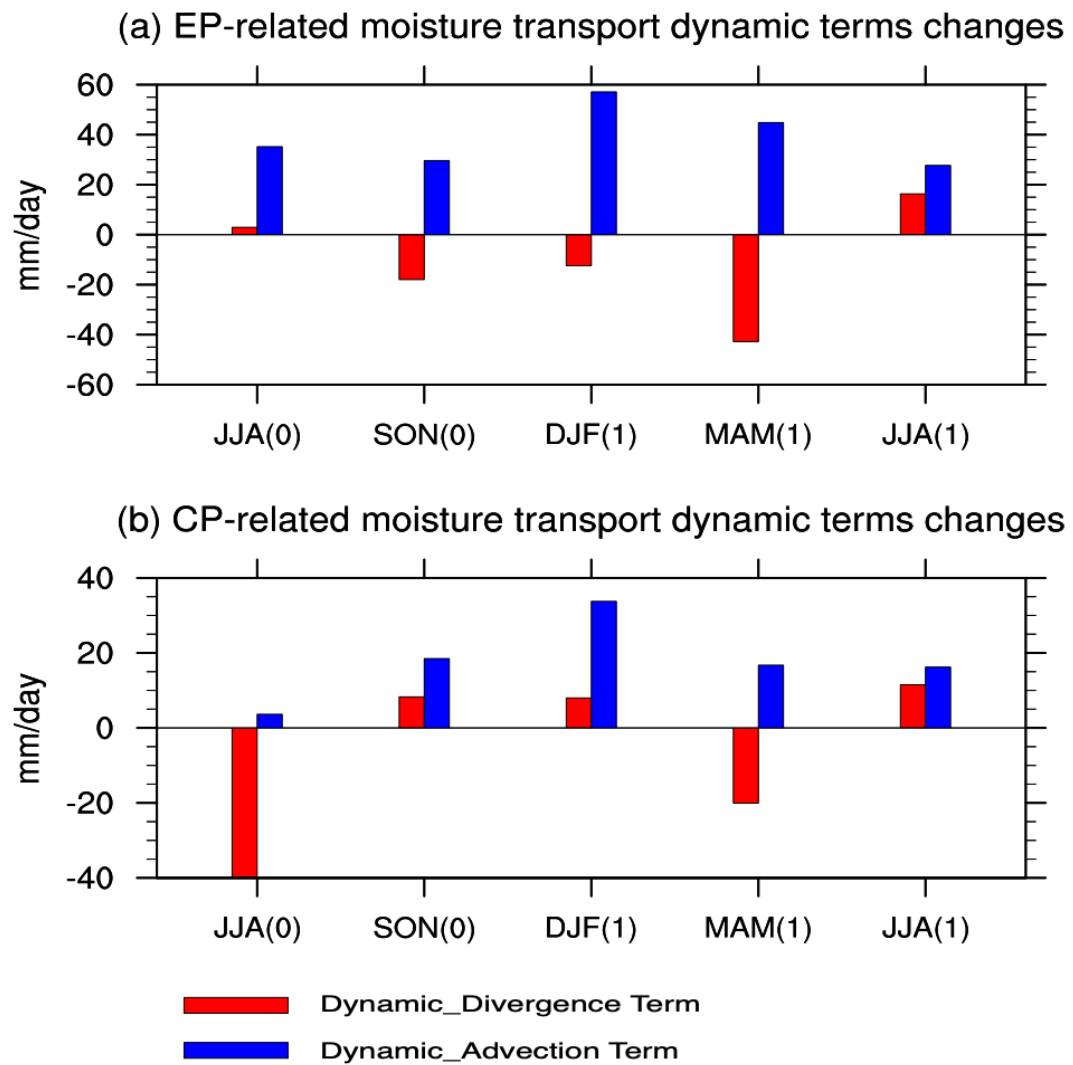


Figure 4.20 The future changes of (a) EP and (b) CP El Niño-related dynamic effect of moisture flux convergence due to changes of circulation anomalies (Dynamic_Divergence Term, red bar) and mean moisture (Dynamic_Advection Term, blue bar) which are projected onto \hat{P}'_H (units: mm/day) during the seasonal cycle of El Niño. See more details in Appendix for dynamic term decomposition.

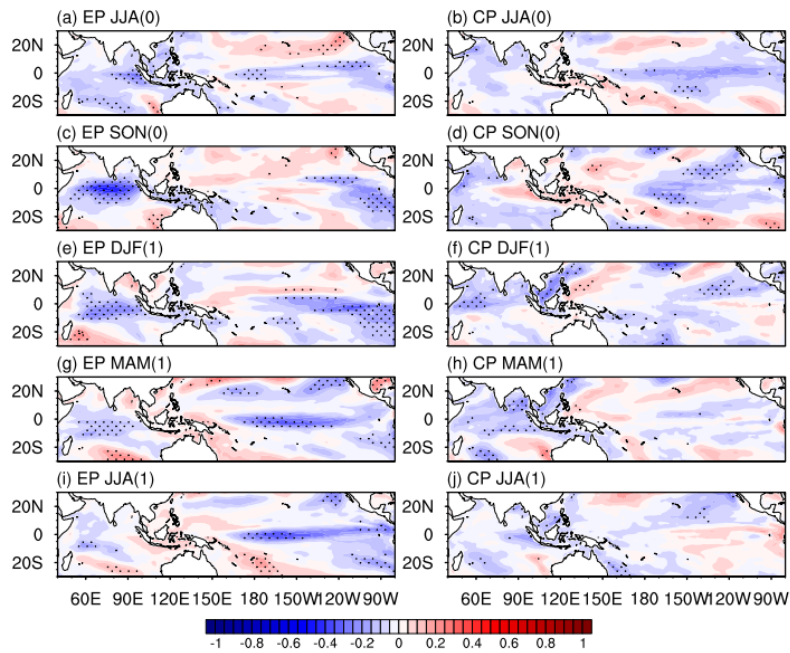


Figure 4.21 The future changes of (a, c, e, g, i) EP and (b, d, f, h, j) CP El Niño-related SSTAs (units: $^{\circ}\text{C}$) based on the differences between composite EP and CP El Niño-related SSTAs from RCP 8.5 scenario and historical simulations. Black dots indicate SSTAs changes passing the 90% significance level.

4.4 Brief summary

Future changes of El Niño-EA teleconnection and its underlying physical mechanisms were elaborated in this chapter. In order to best capture the El Niño-related EA rainfall anomalies under present-day and future climate, the time mean and interannual variations of EASM circulation were evaluated first; nine models were verified to be capable of reproducing El Niño diversity and EASM simultaneously. Over these models, six of them (including bcc-csm1-1-m, CCSM4, CESM1-BGC, CESM1-CAM5, CNRM-CM5, FIO-ESM), named as group A-1, perform better in simulating the El Niño-related EA circulation anomalies; while the others give westward shift of the corresponding stream function, which is consistent with the results in Chapter 3. Inspections of the nine selected models reveal no consensus on how two types of El Niño will be modified in terms of their magnitude and location under global warming. It is also noted that El Niño-induced low-level circulation changes under global warming follow those of the strength and location of El Niño SSTA.

Based on the MME mean of group A-1 models, two types of El Niño-related rainfall change is more obvious in its intensity but not its pattern. In particular, EP El Niño-related rainfall anomalies will be enhanced in a warmer climate during the JJA(0), DJF(1) and JJA(1); for CP El Niño, amplification of rainfall anomalies is seen in DJF(1) and JJA(1). In addition, the intensification of CP El Niño-related rainfall anomalies seems stronger than that for EP El Niño. It is further ascertained that more intense El Niño-induced rainfall will be triggered by global warming unless the El Niño SSTA are massively suppressed.

The change of El Niño-related moisture flux convergence, which is dominant by the dynamic term, well matches its related rainfall amplitude change. For either type of El Niño, a moister atmosphere under global warming can robustly strengthen the rainfall variations; this positive

contribution tend to offset the negative contribution due to weaker El Niño-related circulation anomalies.

5 El Niño-Related Precipitation Under Global Warming Based on AGCM Experiments

In Chapters 3 and 4, the El Niño-related EA/WNP teleconnection under present-day and future climate conditions were investigated based on outputs from selected CMIP5 models. How a warmer climate might shape the El Niño-related rainfall was addressed by diagnosing the moisture budget, with particular focus on the roles of perturbed El Niño-induced circulation and increased mean moisture due to global warming. In this chapter, impacts of global warming on El Niño-EA climate teleconnection are further investigated, based on AGCM-experiments. The atmosphere-only model permits one to isolate the effects of background state perturbations and El Niño SSTA changes. Here the focus is not only on the EA/WNP region but a broader tropical and near-tropical domain.

5.1 AGCM experiment design

For the AGCM experiments, CAM4 was used, with prescribed or model-projected future background climate state, plus El Niño-related SSTA patterns (see Chapter 2). In particular, ten sets of model experiments were carried out as shown in **Table 5.1**, with various states of the climatological SST, CO₂ concentration, as well as SSTA patterns. In the Control_present run, observed climatological (by averaging over 1982-2001) monthly SST is used for 27 years of integration. The transient CO₂ concentration and total solar irradiance (TSI) were kept at constant levels, namely 367 ppm and 1366.09 W/m², respectively, based on the average values during the period of 1982 to 2001 (see **Figure 5.1a, b, c and d** for details). For the future climate experiment (referred to as Control_future), the differences between RCP 8.5 scenario simulations (2050-2099) and historical simulations (1950-1999) of

climatological monthly mean SST based on the MME average of group A-1 models (see **Figure 5.2** for details) were first calculated, and then added onto the SST of Control_present run for reconstructing a future basic SST state. The CO₂ concentration was set to be 719.87 ppm, which is the averaged value during the period of 2050-2099, while TSI was same as that in Control_present (see **Figure 5.1e** and **f** for more details). The increased CO₂ concentration, together with the warmer SST basic state in Control_future run, will give a warmer background climate. The other eight sets of experiments refer to those with SSTA for two types of El Niño superimposed onto the climatology monthly SST over the domain of 30°S-30°N, 40°E-80°W. Note that the SSTA over SCS (0°–30°N, 100°E–120°E) and Eastern China Sea (20°–30°N, 120°E–140°E) were excluded. Sensitivity tests showed that these localized SSTA can lead to large regional rainfall biases in the CAM4 environment (figures not shown). Exp1_EP(CP) had the same basic state as Control_present, but with a repeating two-year life cycle of EP(CP) El Niño-related SSTA from the historical run superimposed onto the background SST (**Figure 5.3** and **Figure 5.5**). In contrast to Exp1_EP(CP), Exp2_EP(CP) adopted the background SST and CO₂ concentration to the future state as in Control_future; the El Niño SSTA was otherwise same from the historical runs. For Exp3_EP(CP) and Exp4_EP(CP), the basic states were the same as those in Exp1_EP(CP) and Exp2_EP(CP), respectively, but with the EP(CP) El Niño SSTA taken from RCP 8.5 simulations (see **Figure 5.4** and **Figure 5.6**). Again, the El Niño-related SSTA were obtained based on the MME mean of projections from group A-1. In general, from the developing year (denoted as year(0)) to mature and decaying year (denoted as year(1)), the SSTA evolve realistically for both El Niño types (see Chapter 3, **Figure 5.3** and **Figure 5.5**). For future El Niño, SSTA patterns are in general similar with their historical counterparts, but with their magnitudes modulated (**Figure 5.4** and **Figure 5.6**). Each of the ten experiments comprises 27 years of integration, and there are 13 ensembles for each set of experiment.

Finally, the following differences were computed:

Exp1_EP(CP) - Control_present, for representing the atmospheric responses to two types of El Niño forcing in the present climate;

Exp3_EP(CP) - Exp1_EP(CP), for assessing the atmospheric circulation changes due to future perturbations of El Niño SSTA only, but under the same historical SST and CO₂ concentration;

Exp2_EP(CP) - Exp1_EP(CP), for assessing the effect of warmer background climate but with same historical El Niño SSTA forcing;

Exp4_EP(CP) - Exp1_EP(CP), for assessing the combined effects of perturbed El Niño SSTA and warmer background climate.

Table 5.1 Design of ten sets of AGCM experiments.

		Historical	Future
No SSTA		El Niño SSTA	El Niño SSTA
Historical mean		Exp1_EP	Exp3_EP
SST and CO ₂	Control_present	Exp1_CP	Exp3_CP
Future mean		Exp2_EP	Exp4_EP
SST and CO ₂	Control_future	Exp2_CP	Exp4_CP

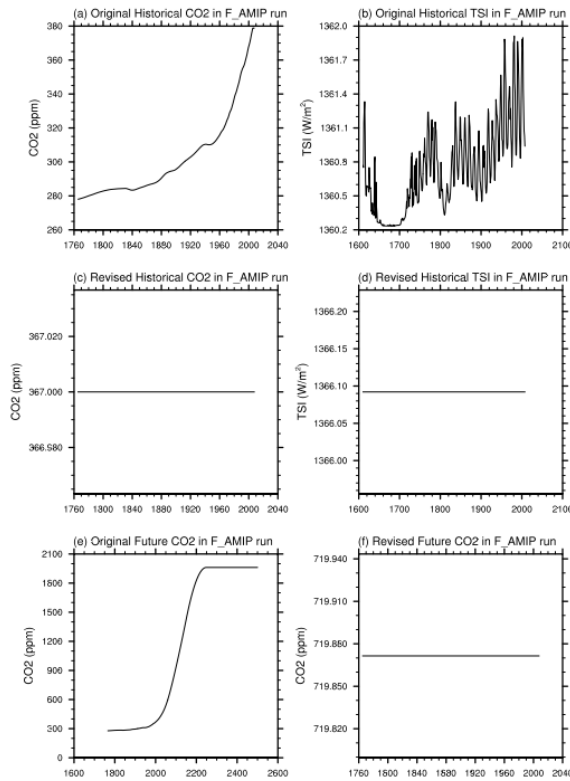


Figure 5.1 (a, b) Original CO₂ concentration and TSI for F_AMIP component set in CAM4, respectively. (c, d) Revised constant CO₂ concentration and TSI in accordant with fixed SST climatology for present-day simulations, respectively. (e) Future projected CO₂ concentration based on RCP 8.5 scenario. (f) Revised CO₂ concentration for future time simulations.

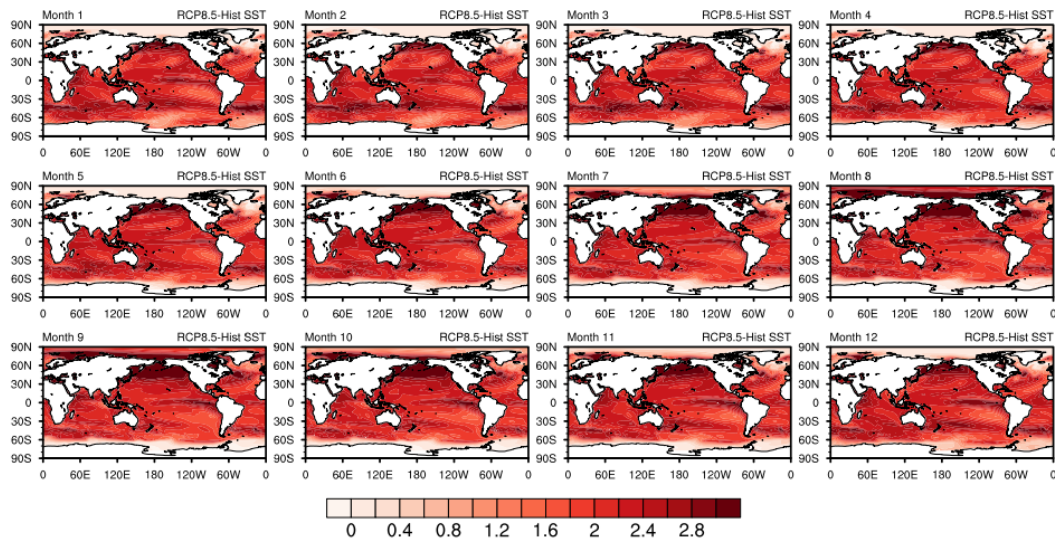


Figure 5.2 Future changes of climatological SST (units: $^{\circ}\text{C}$) based on RCP 8.5 scenario and historical simulations from group A-1 models. See text for more details.

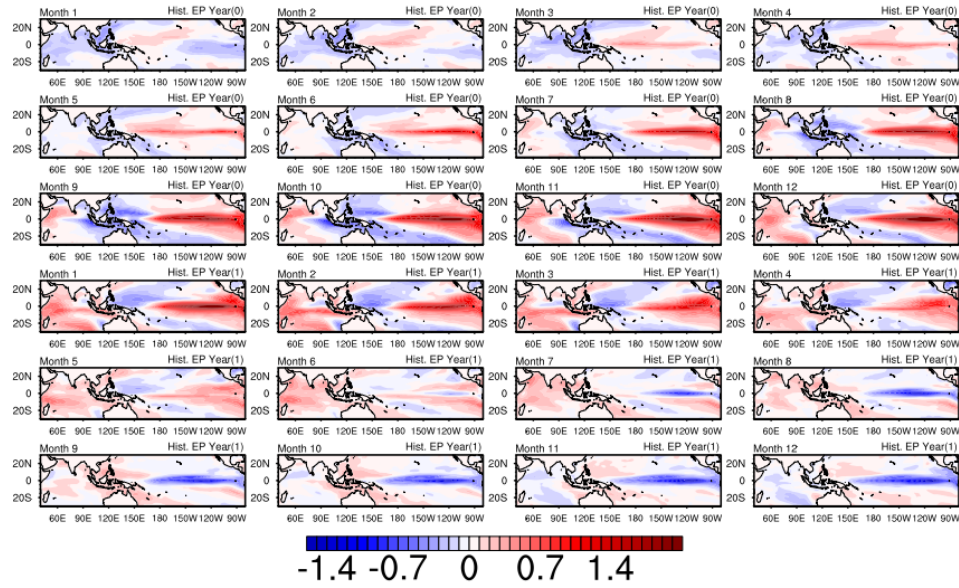


Figure 5.3 Monthly evolution of SSTA during the 2-year life cycle of EP El Niño (units: °C), based on historical runs from group A-1 models, prepared for the AGCM experiments.

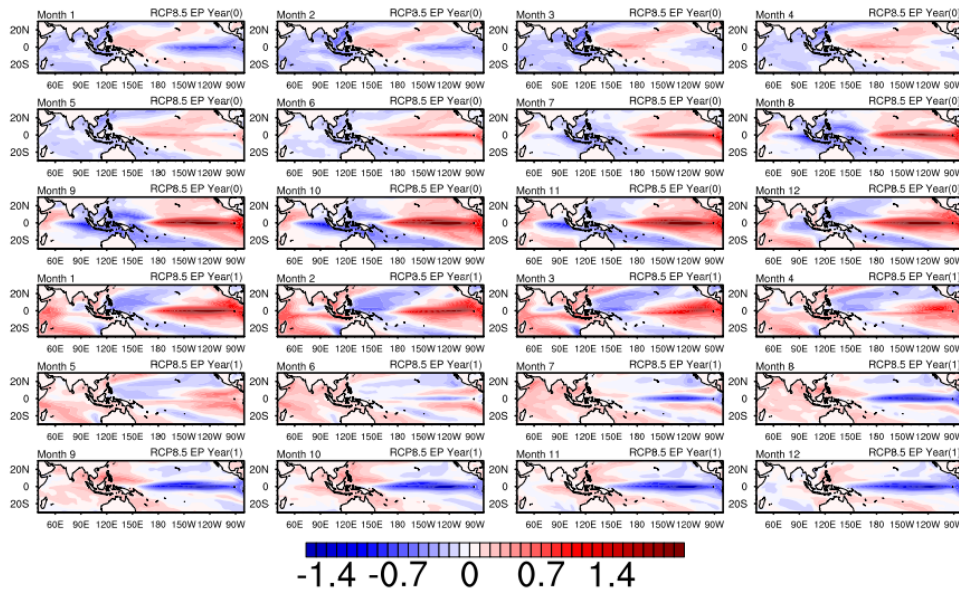


Figure 5.4 Same as **Figure 5.3**, except for the RCP 8.5 scenario.

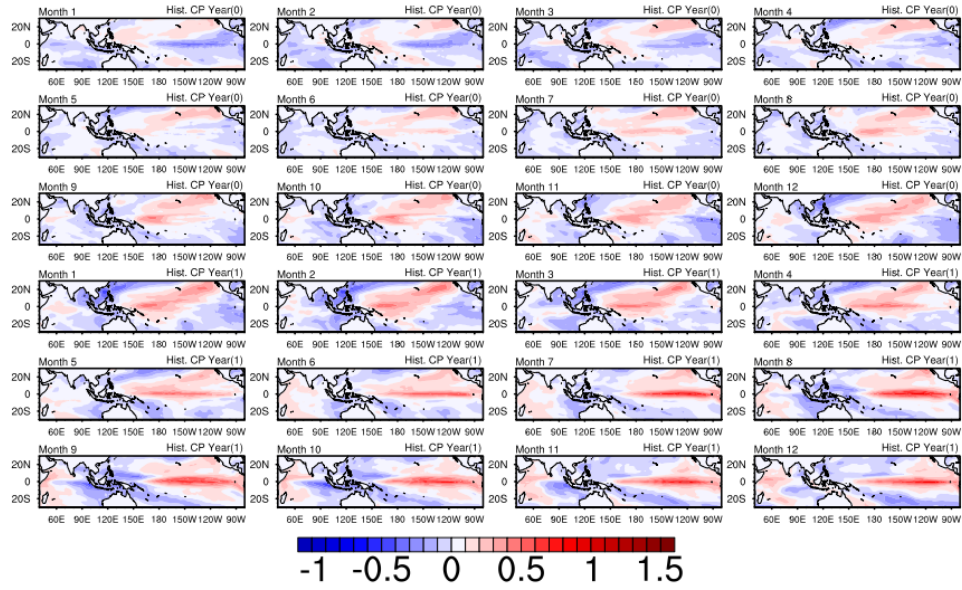


Figure 5.5 Same as **Figure 5.3**, except for CP El Niño

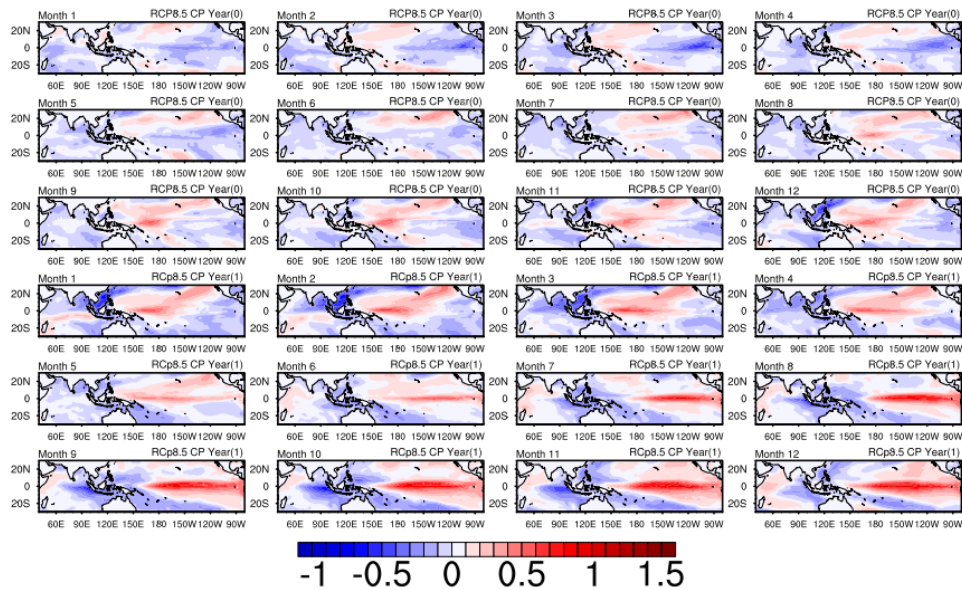


Figure 5.6 Same as **Figure 5.5**, except for the RCP 8.5 scenario.

5.2 Results

5.2.1 Comparison between Control_future and Control_present simulations

Before assessing the El Niño-related rainfall in the AGCM experiments, the mean state of present-day and future climate were compared. Inspection of the surface temperature differences between Control_future and Control_present simulations reveals significant warming throughout the year, with larger magnitudes over land than the ocean (**Figure 5.7**). Meanwhile, an “El Niño-like warming pattern” over the eastern Pacific is found, consistent with results reported by Collins et al. (2010). **Figure 5.8** depicts the difference of precipitable water between Control_future and Control_present runs. It is obvious that the precipitable water over the deep tropics and subtropical regions increases with a warmer SST background, especially over the warm pool region and also ITCZ, supporting more intense hydrological cycle under global warming. It is also noticed that the strongest enhancement lies near the central tropical Pacific for most calendar months. This might be related to an eastward expansion of deep convection from the warm pool region to central tropical Pacific due to warmer SST over the central-eastern Pacific area. For the low-level flow in a warmer climate, CAM4 tends to simulate weaker trades or westerly anomalies over the tropical Pacific, implying a weaker Walker circulation (**Figure 5.9**). Consistent with previous studies, precipitation changes as simulated by CAM4, in general, follow the wet-get-wetter and dry-get-drier paradigm (Held and Soden 2006). However, the monthly rainfall changes over land are insignificant (**Figure 5.10**). In general, the abovementioned results indicate that atmosphere-only experiment can reasonably capture the typical response of the atmosphere to CO₂ concentration increase and SST warming, especially for regions over deep tropics. In the following investigations, the focus will be on El Niño-related circulation over tropical Pacific and the possible influence of SSTA and basic state perturbation in a warmer climate.

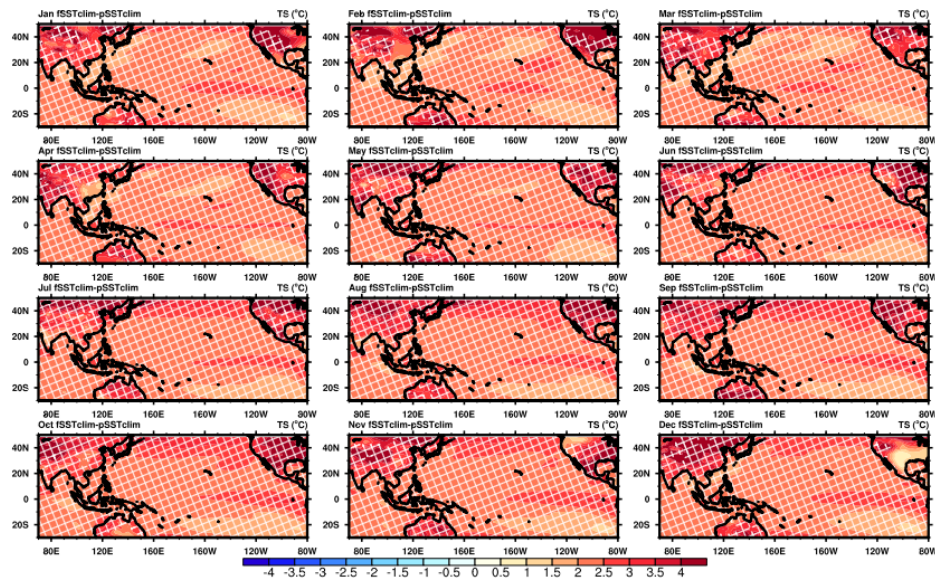


Figure 5.7 Differences of monthly surface temperature (units: $^{\circ}\text{C}$) between *Control_future* and *Control_present* simulations. White crosses indicate the differences passing 90% significance level.

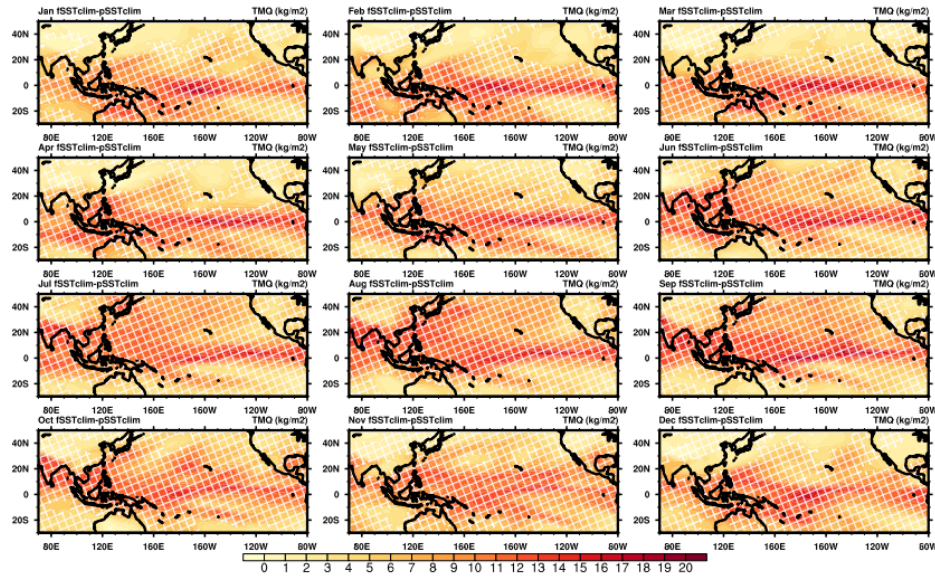


Figure 5.8 Same as **Figure 5.7**, but for monthly total vertically integrated precipitable water (units: kg/m^2).

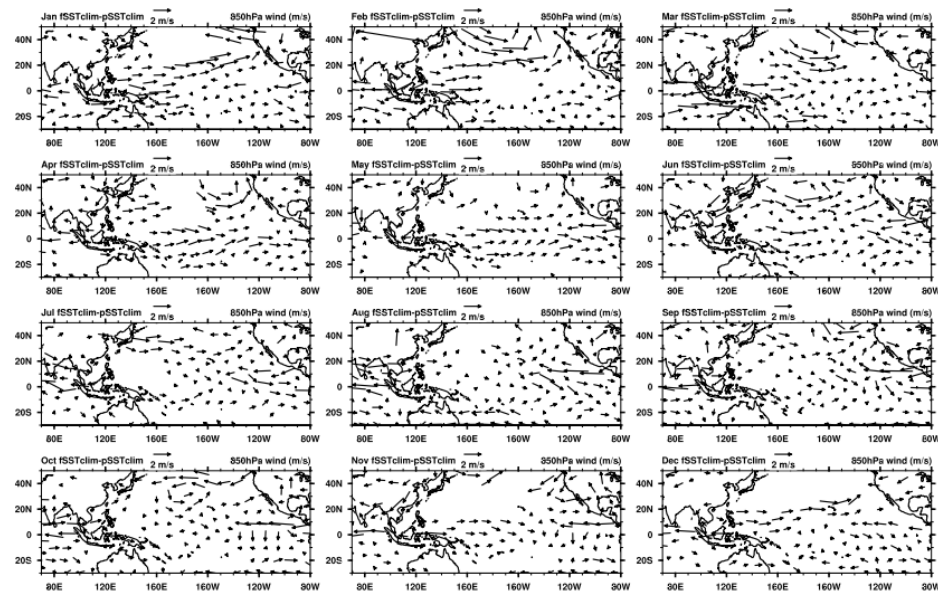


Figure 5.9 Same as **Figure 5.7**, but for 850 hPa wind (see scale arrow at the top in units of m/s).

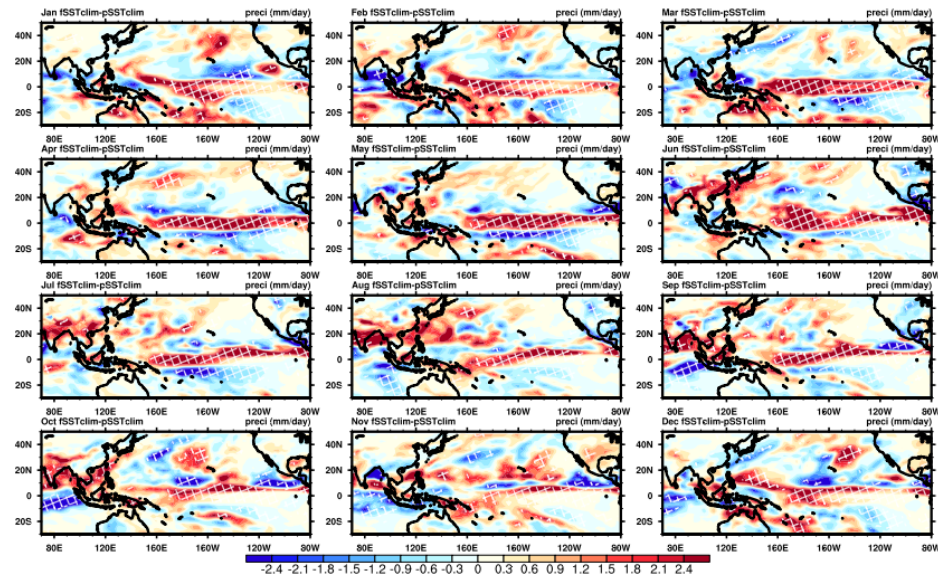


Figure 5.10 Same as **Figure 5.7**, but for precipitation (units: mm/day).

5.2.2 Future changes of El Niño-related rainfall in AGCM runs

The rainfall and low-level circulation anomalies during the DJF(1) of El Niño events, simulated by Exp1_EP(CP), are given in **Figure 5.11**. Under present climate conditions, marked anomalous wet (dry) conditions over the central-eastern Pacific (the western Pacific and EA) flanked by a pair of symmetric cyclonic circulations (anticyclonic circulations) are found during EP El Niño, which are the Gill-type response to EP-type SSTA forcing (**Figure 5.11a**). However, the observed wetter conditions over the eastern China and southern Japan are not well simulated; this could be related to northwesterly biases over these regions which might inhibit the moisture transport, and also due to a very broad anticyclone to the west of dry signal over equatorial WNP (**Figure 5.11a**). For CP EP El Niño, significant wetter (drier) conditions are captured over the central Pacific (SCS and the Philippines) albeit with wet biases found over Bay of Bengal (BOB). Meanwhile, low-level anomalous anticyclonic (cyclonic) flows, passing 90% significance level, are located to the west (east) of the Philippines. Compared with observations, the two types of El Niño-driven circulation responses are displaced westward slightly (figure not shown); this might be related to the slight westward shift of SSTA patterns from coupled models (Collins et al. 2010; Vecchi and Wittenberg 2010). Overall, the broad-scale features of El Niño-related circulation are reasonably simulated by this AGCM. **Figure 5.12a** and **b** give a similar set of results from Exp3, in which the future projected El Niño SSTA were used. In general, anomalous responses to future El Niño forcing resemble those from Exp1; for CP EP El Niño, stronger cyclonic circulation anomaly over the WNP is found to expand northwestward. In fact, since the CP El Niño-related SSTA is marginally enhanced (compare **Figure 5.5** and **Figure 5.6**), the anomalous rainfall and circulation over the Maritime Continent and western Pacific also tend to be stronger. For EP El Niño, since EP-type SSTA is projected to be weaker (compare **Figure 5.3** and **Figure 5.4**), positive (negative) perturbations to rainfall are found over the

105

western Pacific (equatorial central-eastern Pacific). Notwithstanding the low significance level in **Figure 5.12b**, these results highlight the fact that El Niño-related SSTA intensity change governs the amplitudes of anomalous rainfall and circulation.

To demonstrate the influence of a warmer background climate, **Figure 5.13** gives the differences between Exp2 and Exp1. Common patterns of the El Niño-related rainfall and circulation are captured by Exp2 as those in Exp1 (**Figure 5.13a and b**). For EP El Niño, significant intensification of the atmospheric responses is seen with roughly a wet-get-wetter and dry-get-drier pattern of the anomalous rainfall perturbations (**Figure 5.13c**). In particular, drier (wetter) conditions are simulated over the western Pacific (central-eastern Pacific), which are consistent with the results in Huang and Xie (2015) and Power et al. (2013). It is also noticed that EP El Niño-related rainfall seem to shift slightly eastward; this can be inferred from the difference of rainfall anomalies near 150°E-180° (**Figure 5.13c**). The result reflects those of Power et al. (2013), and might due to the eastward drift of the mean tropical convections in Exp2_EP. For CP El Niño, the anomalous rainfall and low-level flow are also stronger under a warmer basic state even though the significance level is lower than EP El Niño. In particular, dry anomalies over the Maritime Continent become stronger, accompanying an eastward extension of dry (wet) conditions to the tropical region near 180° (150°W) (**Figure 5.13d**). Moreover, the corresponding circulation anomalies, in general, strengthen as well even though same EP and CP El Niño forcing were used in Exp2 and Exp1; this implies a stronger atmospheric response to same El Niño forcing in a warmer climate. To ensure consistency with comparison between Exp2 and Exp1, a set of identical comparison between Exp4 and Exp3 is given in **Figure 5.14**. It is obvious that the differences of anomalous rainfall and low-level flow resemble those in **Figure 5.13**, stressing again the effect of warmer background climate on El Niño-driven teleconnection. Overall, the general patterns of both types of El Niño-related rainfall anomalies tend to be enhanced over the deep

tropics in a warmer climate, consistent with the results in Chapter 4 and also supported by recent literature (Power and Delage 2018). It is also likely that global warming can result in a eastward shift of the tropical rainfall over the Pacific for both EP and CP El Niño. Note that the eastward displacement of the rainfall anomaly is also consistent with the changes of time mean rainfall (see **Figure 5.10** for more details). Finally, the difference between Exp4 and Exp1 is given in **Figure 5.15**, which gives the combined impacts of a warmer background and perturbed El Niño-related SSTA. Tropical rainfall anomalies and the corresponding circulation anomalies are significantly enhanced. Drier (wetter) conditions are found from the Maritime Continent to equatorial western Pacific (over equatorial central-eastern Pacific) for EP El Niño. For CP El Niño, drier (wetter) conditions are located over the Maritime Continent and equatorial western Pacific (WNP and off-equator central Pacific). To summarize, the El Niño-related rainfall over the deep tropics as simulated by AGCM will be intensified under global warming. Note that the projected weaker EP El Niño SSTA tend to reduce the circulation anomalies, but this can be offset by the effects from a warmer climate background. For CP El Niño, both stronger future CP-type SSTA and warmer basic state will play a positive role in strengthening the rainfall anomalies. Given the marginal change in the amplitude of El Niño SSTA, a warmer climate background might be more critical to enhance the El Niño-driven rainfall anomalies. The warmer basic state not only provides more moisture in the atmosphere, but also displaces the El Niño-related equatorial rainfall eastward by modulating the mean background convection. It is also noteworthy that the response to EP El Niño forcing is rather robust since the rainfall and circulation anomalies have high consistency amongst different experiments; for CP El Niño, the patterns of anomalous rainfall and circulation seem more distinctive in different experiments (comparing **Figure 5.11b** with **Figure 5.12 b**).

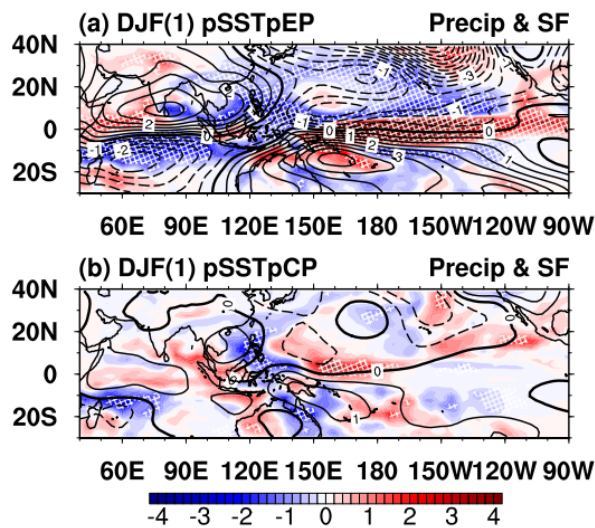


Figure 5.11 Ensemble mean of anomalous precipitation (shading; see scale bar at bottom in units of mm/day) and 850-hPa stream function (solid and dashed contours denoting positive and negative values, respectively, with interval of $0.5 \times 10^6 s^{-1}$) during the DJF(1) of (a) EP and (b) CP El Niño based on Exp1. White crosses indicate precipitation anomalies passing the 90% significance level.

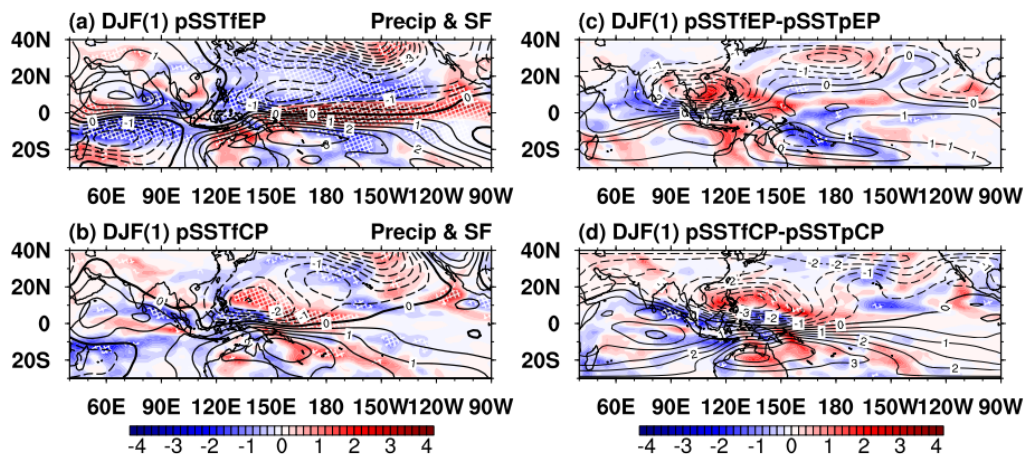


Figure 5.12 (a, b) Same as **Figure 5.11**, but based on Exp3. (c, d) Same as **Figure 5.11**, but for differences between Exp3 and Exp1.

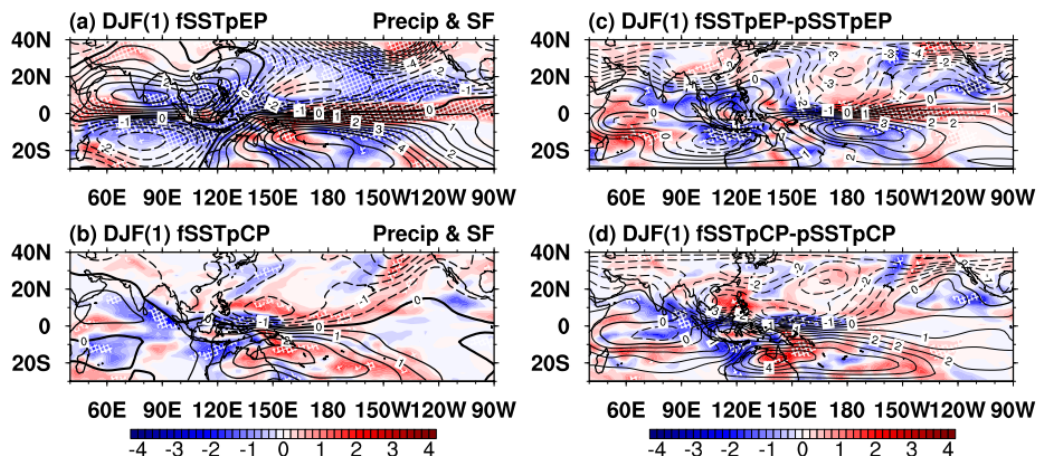


Figure 5.13 Same as **Figure 5.12**, but (a, b) for Exp2 and (c, d) for differences between Exp2 and Exp1

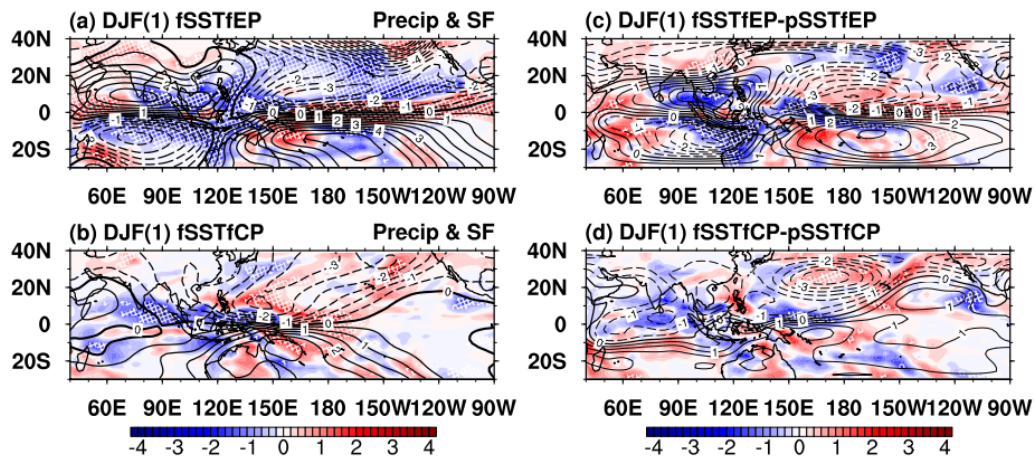


Figure 5.14 Same as **Figure 5.12**, but (a, b) for Exp4 and (c, d) for differences between Exp4 and Exp3.

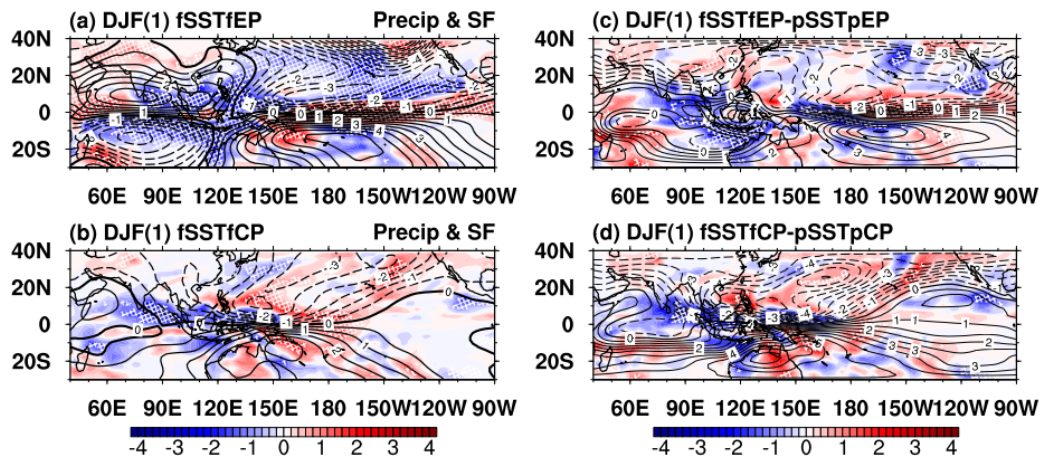


Figure 5.15 Same as **Figure 5.12**, but (a, b) for Exp4 and (c, d) for differences between Exp4 and Exp1.

5.2.3 Moisture budget analyses

To further understand the roles of various circulation elements in modulating the El Niño rainfall, moisture budget analyses (see Chapter 4) were carried out based on the AGCM outputs. **Figure 5.16** gives the total moisture flux and its divergence for Exp1 to Exp4. As expected, the moisture flux convergence largely resembles the rainfall pattern corresponding to each AGCM experiment (see **Figure 5.16**). The moisture flux due to the dynamic term is given in **Figure 5.17**, which dominates the total moisture flux. In general, the thermodynamic terms, for each of the experiments, are much smaller than the dynamic terms, thus negligible to first approximation (see **Figure 5.18**). Also, variations of moisture flux between different sets of experiment are mainly due to the dynamic term. Changes in the total moisture flux between two chosen sets can then be approximated by the dynamic term, which is partitioned to results due to perturbations of the mean moisture and El Niño-related circulation (see again Chapter 4). For Exp4 and Exp1, the difference in the total moisture flux, the dynamic term, the component of the latter due to circulation (referred to as `dynamic_divergence` term) and that due to mean moisture change (referred to as `dynamic_advection` term) are depicted in **Figure 5.19**. Again, the differences in total moisture flux largely reflects changes in anomalous rainfall, especially over the tropical Pacific and IO, and that the dynamic term is the dominant term in comparison to the thermodynamic term. As for the `dynamic_divergence` term (i.e. component due to circulation change), there is divergence (convergence) over 130°E–180° (east of 180°) for EP El Niño; for CP El Niño, convergence is seen over the central tropical Pacific. Regarding `dynamic_advection` term, moisture flux divergence (convergence) is found over IO and most of WNP (equatorial central-to-eastern Pacific) for EP El Niño; for CP El Niño, there is weak convergence near the central Pacific. (**Figure 5.19**). Comparing the two components of the dynamic terms, the `dynamic_divergence` term

$(\frac{1}{g\rho_w} \phi(q_{cH} \delta(\vec{V}')))$ corresponds more to rainfall differences since changes in El Niño-driven circulation ($\delta(\vec{V}')$) are more dominant than mean moisture (q_{cH}); the dynamic_advection term $(\frac{1}{g\rho_w} \phi(\vec{V}_F' \delta(q_c)))$ gives a pattern similar to the original pattern of rainfall anomalies (see **Figure 5.15a and b**), but with weaker magnitude. In general, the amplitude of El Niño-induced rainfall and its shift can be modulated by the circulation changes (**Figure 5.19e and f**). On the other hand, the increase in mean moisture merely contributes to the general intensification of El Niño-related rainfall as appeared in the present climate simulations in CAM4 (**Figure 5.19g and h**). Note that the effect of El Niño-related circulation is larger than that of the mean moisture change; this implies the important role of perturbations of anomalous circulation in determining El Niño-related rainfall based on AGCM simulations.

To further study the effect of a warmer background in the absence of modified El Niño SSTA, results based on Exp2 and Exp1 are shown in **Figure 5.20**. Differences in the total moisture flux, the dynamic term, the dynamic_divergence term and the dynamic_advection term between Exp2 and Exp1 are found to be very similar with their counterparts shown in **Figure 5.19**. It is noteworthy that dynamic_divergence term can be intensified for both types of El Niño, even though there is no change of El Niño SSTA. A “nonlinear” response of canonical El Niño-related rainfall to robust changes in background SST due to global warming has also been reported in Power et al. (2013). In other words, the nonlinearity refers to different El Niño-driven rainfall anomalies due to same SSTA forcing, but under different SST mean state (Power et al. 2013). Here, the intensified dynamic_divergence term might be related to the aforementioned “nonlinear” effect; the response of circulation anomalies to El Niño SSTA can be stronger under a warmer climate. Our results highlight that, for both types of El Niño, stronger circulation responses to identical SSTA in warmer background state tend to strengthen the El Niño-related moisture transport. To summarize, both perturbations of

circulation anomalies and mean moisture due to global warming contribute to stronger moisture flux and its convergence, consistent with El Niño-related rainfall over the deep tropics, based on these AGCM experiments. The effects of perturbed anomalous circulation, in general, is stronger than that due to enhanced background moisture. The former effect is more relevant to changes of rainfall intensity and pattern, while the latter serves to further strengthen present-day El Niño-related precipitation pattern. More importantly, the future background SST and radiative forcing can modulate the El Niño-driven rainfall anomalies by strengthening the anomalous circulation response to identical El Niño SSTA.

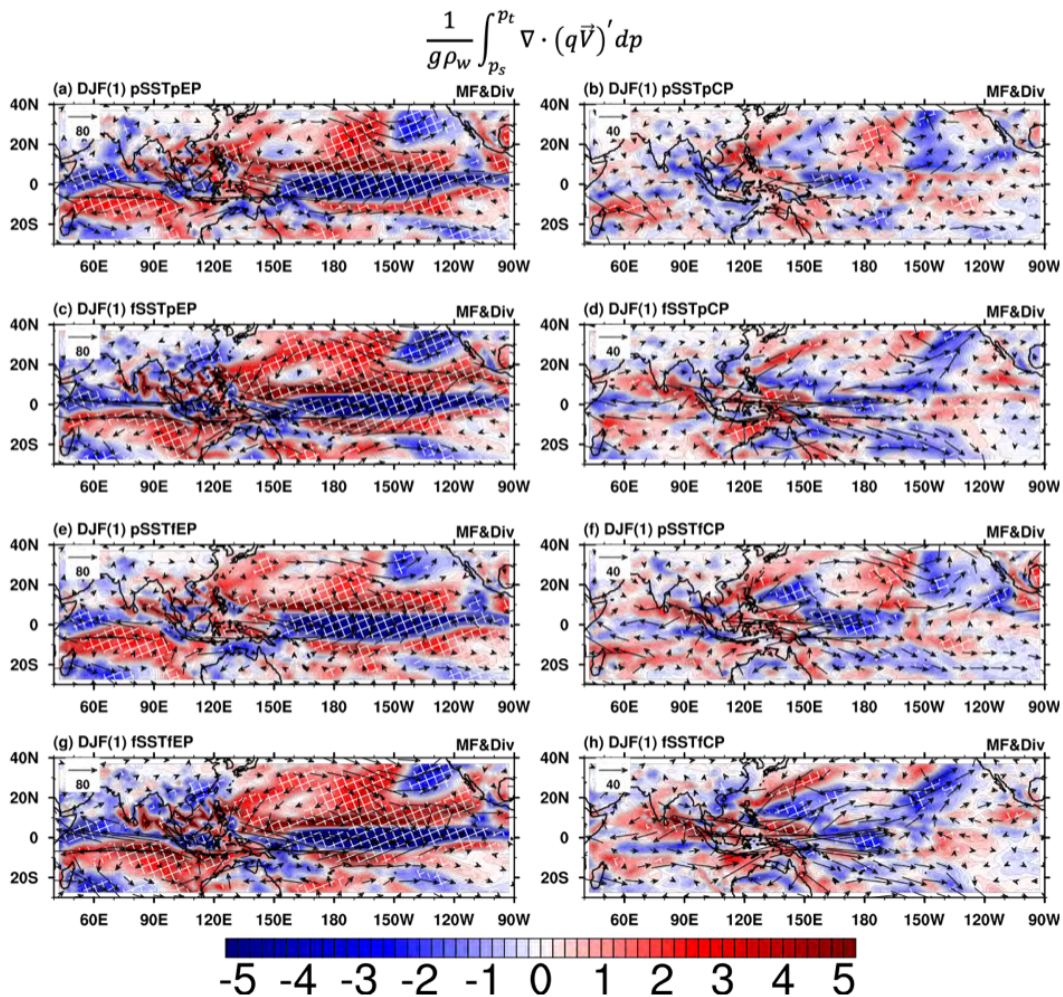


Figure 5.16 Ensemble mean of vertically integrated moisture flux convergence (negative values correspond to moisture convergence) contributing to the anomalous rainfall (shading; see scale bar at bottom in units of mm/day) and the corresponding moisture flux transport (vectors; see scale arrow at top left in units of $\text{kg m}^{-1} \text{s}^{-1}$) anomalies during DJF (1) of (a, c, e, g) EP and (b, d, f, h) CP El Niño based on the (a, b) Exp1, (c, d) Exp2, (e, f) Exp3 and (g, h) Exp4. White crosses indicate moisture convergence anomalies passing the 90% significance level.

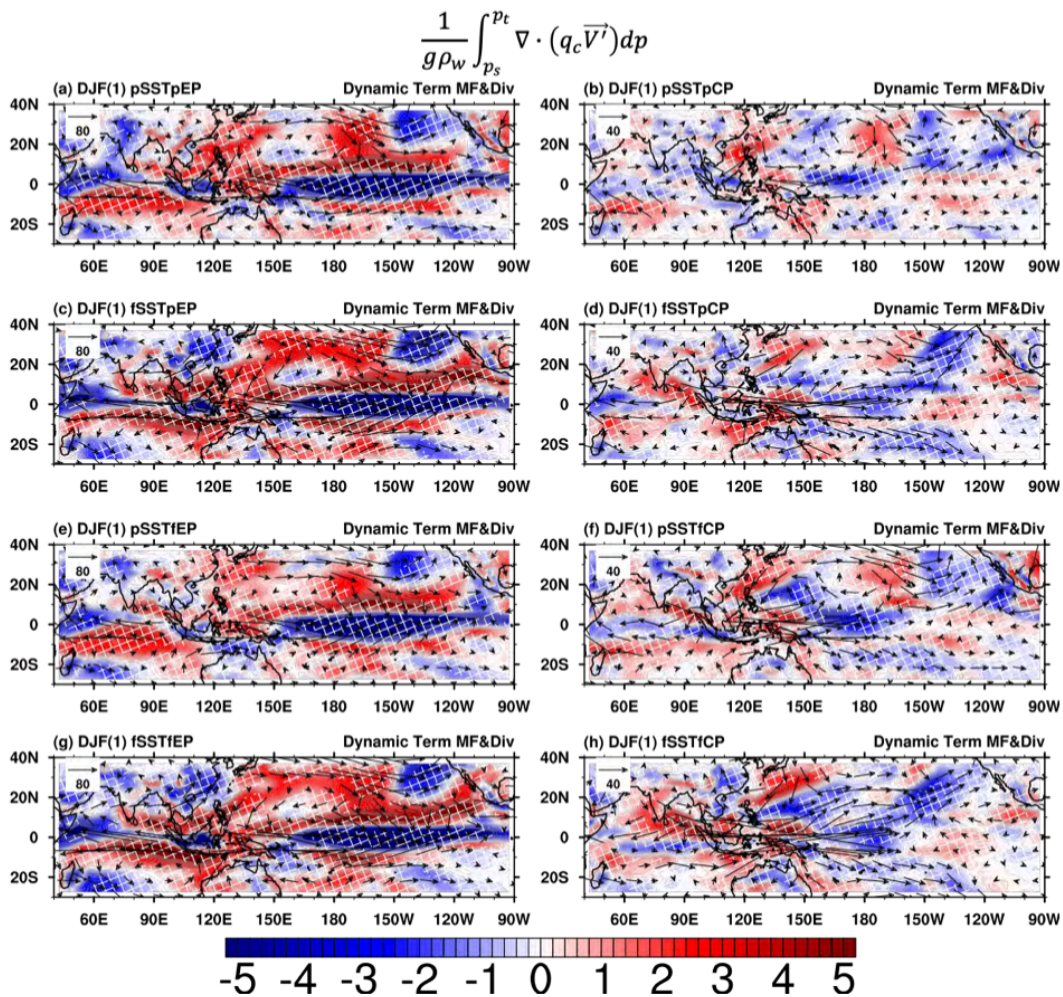


Figure 5.17 Same as Figure 5.16, but for moisture flux and its convergence due to dynamic term.

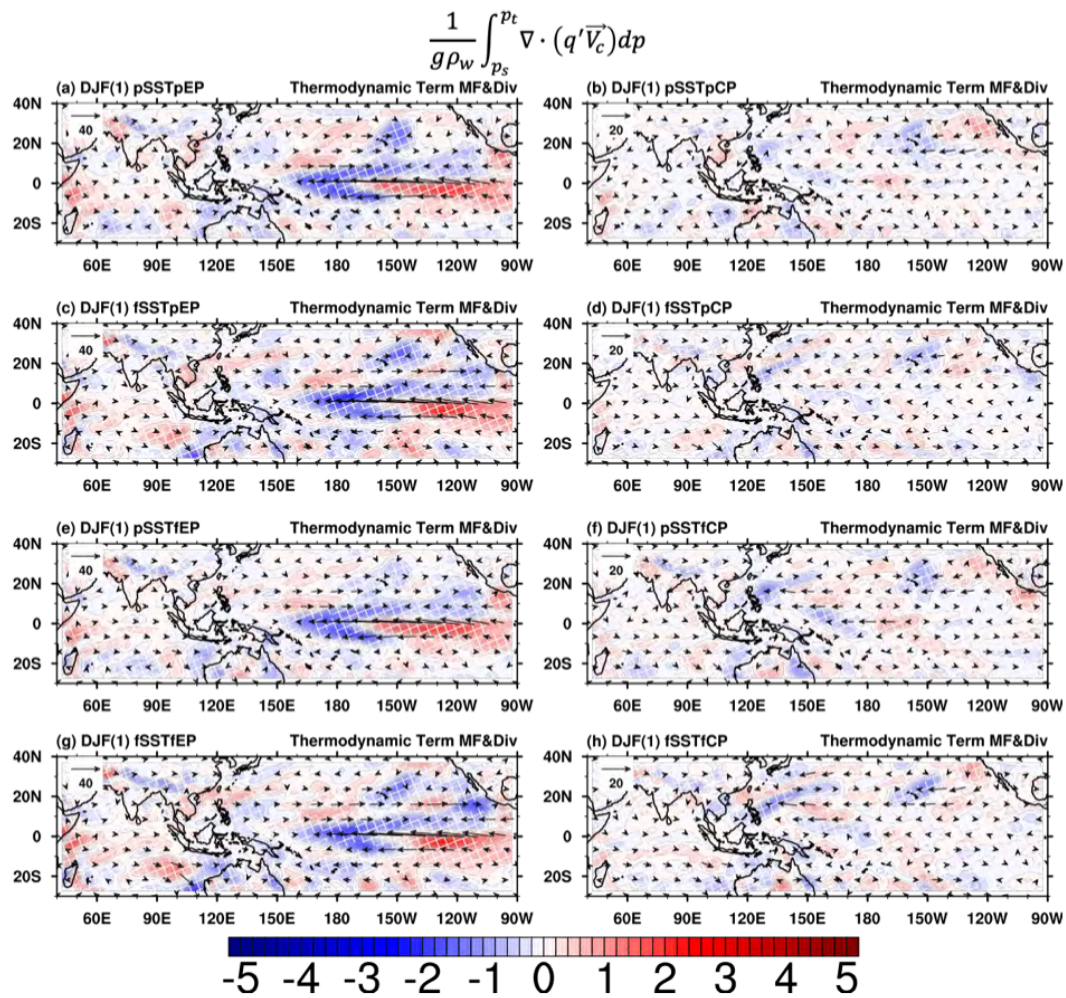


Figure 5.18 Same as Figure 5.16, but for moisture flux and its convergence due to thermodynamic term.

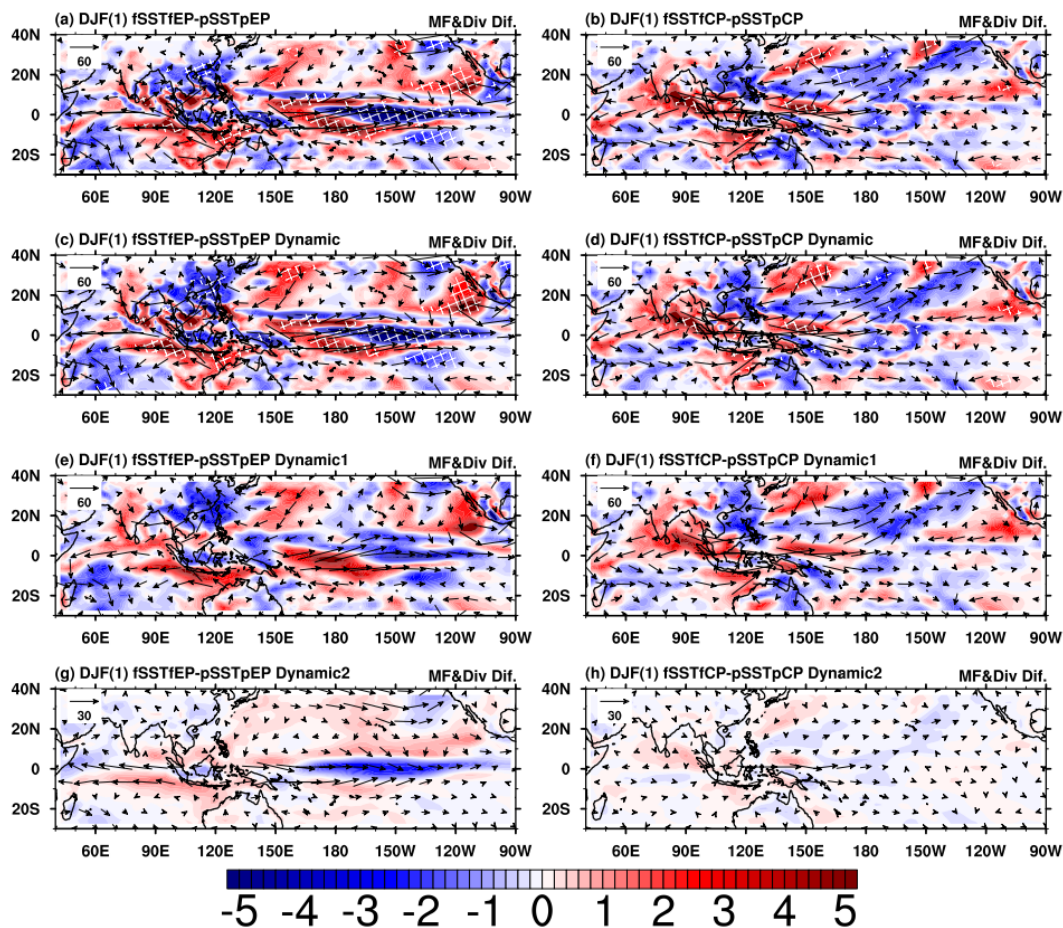


Figure 5.19 Differences of vertically integrated moisture flux convergence (shading; negative values correspond to moisture convergence; see scale bar at bottom in units of mm/day) and the corresponding moisture flux transport (vectors; see scale arrow at top left in units of $\text{kg m}^{-1} \text{s}^{-1}$) anomalies between Exp4 and Exp1 for (a, c, e, g) EP and (b, d, f, h) CP El Niño. (a, b) for total moisture transport changes: $\frac{1}{g\rho_w} \delta(\phi(q\vec{V})')$; (c, d) for dynamic term changes: $\frac{1}{g\rho_w} \delta(\phi(q'\vec{V}_c))$; (e, f) for dynamic_divergence term: $\frac{1}{g\rho_w} \phi(q_{ch}\delta(\vec{V}'))$; (g, h) for dynamic_advection term: $\frac{1}{g\rho_w} \phi(\vec{V}_F'\delta(q_c))$; Here H and F correspond to Exp1 and Exp4, respectively. White crosses indicate differences passing the 90% significance level.

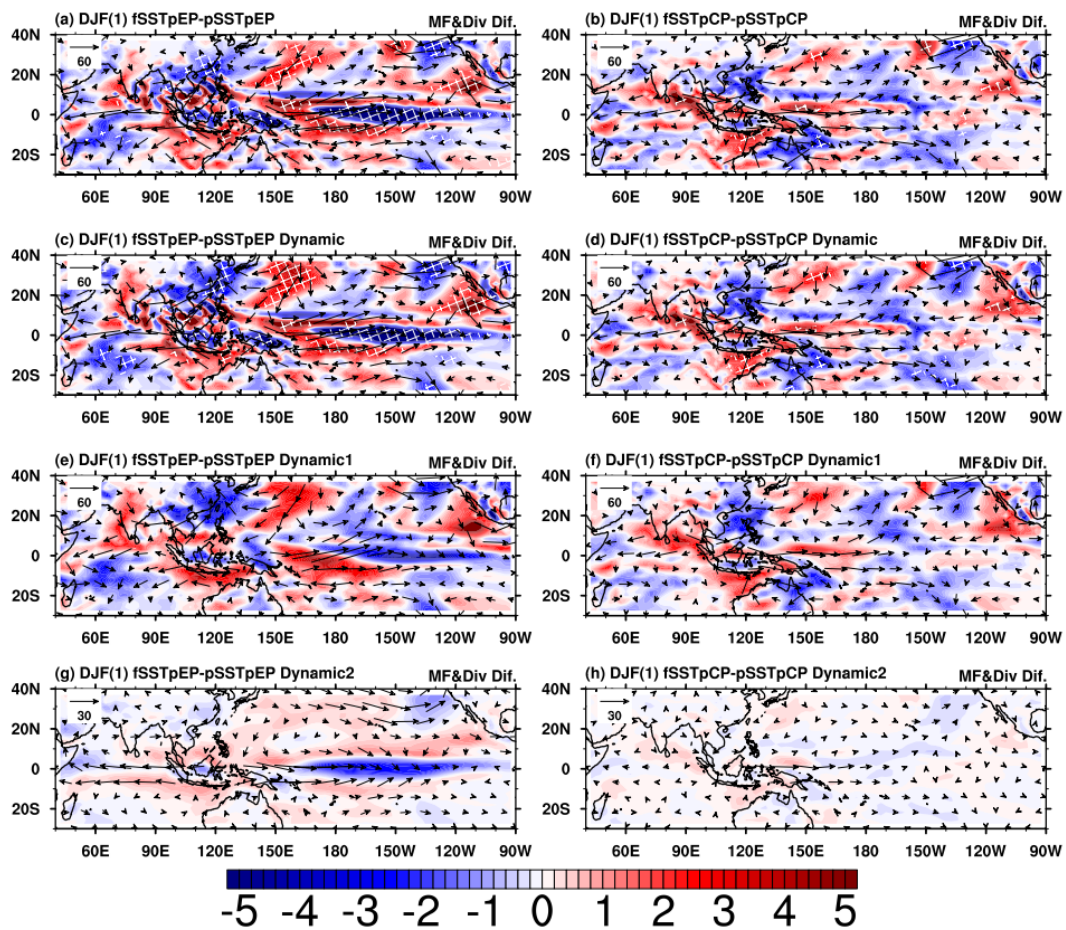


Figure 5.20 Same as **Figure 5.19**, but for differences between Exp2 and Exp1.

5.3 Brief summary

In this chapter, AGCM experiments have been used to delineate how a warmer background climate and SSTA changes can affect El Niño-driven rainfall anomalies. In response to a warmer basic state, the general patterns of both EP and CP El Niño-related rainfall tend to be enhanced over the deep tropics, accompanying a slightly eastward shift which is probably due to the modulated mean background convection. Based on moisture budget analyses, the amplified El Niño-induced rainfall and its shift can be mainly attributed to the perturbed circulation anomalies; the moister atmosphere merely contributes to the general intensification of present-day El Niño-related rainfall. It is noteworthy that the warmer background SST and stronger radiative forcing can intensify the anomalous rainfall by not just providing more moisture in the atmosphere, but also by modulating the rainfall response by strengthening the El Niño-related circulation even with the same El Niño SSTA. Given the marginal change of El Niño SSTA due to global warming, its related changes in circulation anomalies seem to serve a minor role in comparison to changes in the background state of the climate.

6 El Niño Changes Under Global Warming: Role of Ocean-Atmosphere Feedback

In Chapters 4 and 5, investigations based on CMIP5 models and AGCM indicate that El Niño SSTA in the future climate, in terms of both their magnitude and location, are critical in determining projected El Niño-related teleconnection. However, there is no consensus on how the two types of El Niño will be modified in a warmer climate, due to large uncertainties among individual coupled models in simulating future El Niño state (see **Figure 4.9** for more details). In this chapter, we aim to provide useful insights into El Niño changes by inspecting ocean-atmosphere feedbacks in these CMIP5 models under present and future climate.

6.1 Relationship between EP and CP El Niño changes

The future EP and CP El Niño-related SSTA changes are revisited and compared in **Figure 6.1**. It is intriguing that models which simulate a stronger (weaker) EP El Niño tend to produce a stronger (weaker) CP El Niño; this is evidenced by the strong correlation between EP and CP El Niño SSTA differences for the nine individual models, reaching 0.936 which exceeds the 99.9% confidence level (**Figure 6.1a**). In addition, the location changes of EP and CP El Niño-related warming centers are also positively correlated (**Figure 6.1b**); note that the correlation coefficient is insignificant, but it can be 0.6, if M_2 which has an abnormal shift of CP-type SSTA, is excluded. The abovementioned coherence between changes of the two El Niño flavors suggests that the dynamics of EP and CP El Niño in coupled models are governed by the same physical processes. Therefore, global warming tends to modulate EP and CP El Niño SSTA in a similar fashion through the same ocean-atmosphere feedback processes. For a better understanding of the relationship between EP

and CP El Niño changes, the ocean-atmosphere feedbacks based on observations, historical and RCP8.5 scenario outputs are analyzed for both EP and CP ENSO in the following section.

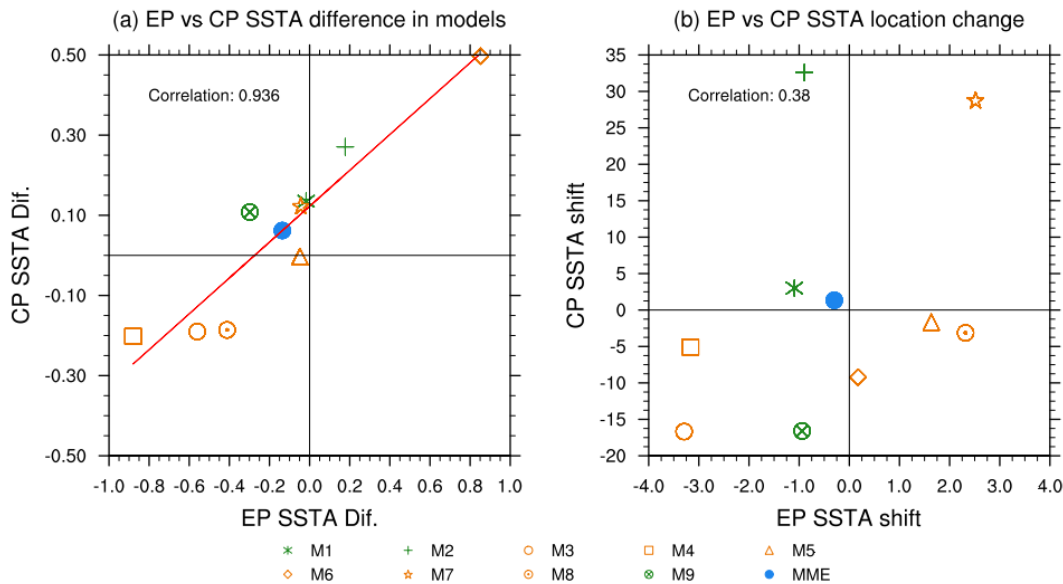


Figure 6.1 Scatter plots of EP and CP El Niño-related (a) SSTA magnitude differences (units: $^{\circ}\text{C}$); (b) SSTA location changes (units: $^{\circ}$) between RCP 8.5 scenario and historical outputs in group A-1 (markers in orange) and B-1 (markers in green) models. The blue dots indicate the MME mean based on all the nine selected models.

6.2 El Niño-related ocean-atmosphere feedback changes in the future climate

The ENSO-related atmospheric feedback, heat flux feedback, and thermocline feedback in the historical run and future climate projections, are assessed in this section. First, an EP (CP) ENSO index corresponding to the principal component of the EP (CP) El Niño-related EOF mode (see section 2.2.1) is defined, namely T' . This dimensional principal component time series, if multiplied by its related normalized EOF pattern, can represent the contribution of the EP (CP) component to the total SST variabilities. Then, the surface zonal wind stress (τ_x), net heat flux (NH) and thermocline depth ($Z20$) anomalies can be regressed onto these indices at each grid point, yielding “sensitivity maps” representing the strength of atmospheric feedback, heat flux feedback and thermocline feedback processes, respectively. The above analyses are carried out during the period of 1979-2010 for observations, 1950-1999 for historical model outputs and 2050-2099 for RCP 8.5 scenario outputs.

Figure 6.2 presents the observed results for these feedbacks. It is noticed that the anomalous positive zonal surface wind stress responses are located near 150°E–130°W for EP ENSO, and around 120°E–180° for CP ENSO, which correspond to the anomalous surface westerlies west of the ENSO-type warming (**Figure 6.2a and b**). The distinct locations of positive atmospheric feedback parameters (μ) for EP and CP ENSO well reflect the contrasting locations of ENSO-related warming center. For heat flux feedback, strong damping effects are observed for EP ENSO, with negative feedback parameters (α) over the equatorial central-eastern Pacific; for CP ENSO, significant is found near 140°E–180° (**Figure 6.2c and d**). It is also noteworthy that damping to EP ENSO SSTA is robust with significant signals over the central-eastern Pacific while less significant for CP ENSO. The thermocline depth anomalies, in response to EP ENSO-related SSTA, exhibit a west-east gradient with negative

feedback parameters (κ) in the western Pacific, and positive κ in the eastern Pacific. This result indicates that the thermocline depth tends to deepen (shoal) over the eastern Pacific (western Pacific) during the warm phase of EP ENSO. For CP ENSO, the thermocline feedback map manifests positive κ over the region of 180° – 120°W , implying a deeper thermocline depth over the equatorial central Pacific during CP El Niño. In general, the structural patterns of atmospheric feedback, net heat flux feedback and thermocline feedback, for both EP and CP ENSO, are consistent with the spatial distributions of their SSTA, emphasizing that these feedbacks are all responsible for both types of ENSO formation. In addition, enhanced atmospheric and thermocline feedbacks can amplify the ENSO amplitude, while stronger net heat flux feedback tends to dampen ENSO.

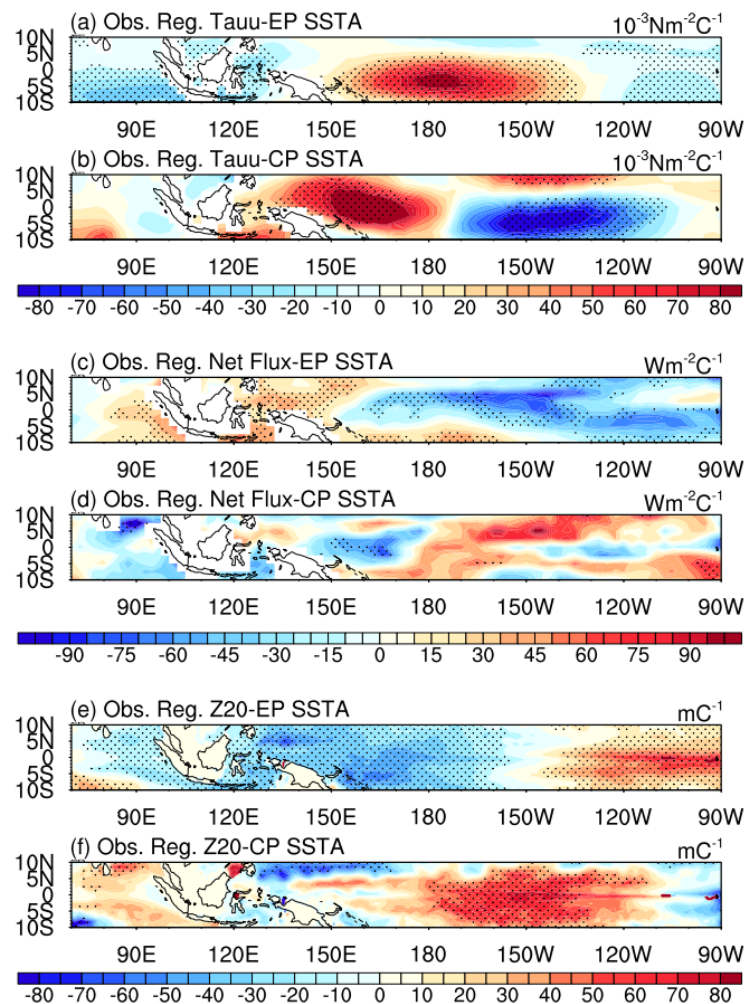


Figure 6.2 (a, b) Observed sensitivity maps of zonal wind stress anomalies (units: 10^{-3}Nm^2) responses to (a) EP ENSO index (unit: $^{\circ}\text{C}$) and (b) CP ENSO index (unit: $^{\circ}\text{C}$); (c, d) Same as (a, b) but for net heat flux anomalies (units: Wm^{-2}) and ENSO index; (e, f) Same as (a, b) but for thermocline depth anomalies (units: m) (see text for more details). Black dots denote the regression coefficients exceeding 95% confidence level.

The model-simulated atmospheric feedbacks by regressing τ'_x onto the EP and CP ENSO-related T' based on historical and RCP 8.5 scenario simulations are shown in **Figure 6.3** and **Figure 6.4**, respectively. In general, sensitivity maps of atmospheric feedback in models resemble those in observations. Positive values of the parameter μ over the equatorial Pacific, representing the strength of EP ENSO-related atmospheric feedback, are confined over 150°E to 120°W, with some inter-model variations of its magnitude. For CP ENSO, positive μ extends to the western-central Pacific, accompanied by a westward shift of the feedback center compared with that for EP ENSO. In addition, feedback centers for CP ENSO are located more westward relative to the observed; this might be related to the common bias of a westward drift of CP El Niño SSTA in models (see Chapter 3). Overall, there is robust inter-model consistency in the EP ENSO-related atmospheric feedback, but much less so for CP ENSO; note that the significance level for CP ENSO is lower compared with that for EP ENSO. It is also consistent with the results in Chapter 3 that models tend to give robust EP-type SSTA, but not for CP-type SSTA. Comparing the sensitivity maps of zonal surface wind stress to ENSO-related SSTA under future (**Figure 6.4**) and present (**Figure 6.3**) climate, patterns of μ remain largely unchanged, albeit with some differences in their magnitude, indicating that the atmospheric feedback intensity can be modified under global warming. Again, such future change of μ tends to have rather large inter-model variations. For instance, the atmospheric feedback simulated by M_5 tends to be weakened, but strengthened for that in M_6.

The net heat flux feedback α is depicted in **Figure 6.5** and **Figure 6.6** for present and future state, respectively. It is noticed that the damping effect of net heat flux feedback for EP ENSO is well captured in these nine models, with significant negative feedback over the central-eastern Pacific, even though large inter-model variations in both their pattern and strength exist (**Figure 6.5**). For CP ENSO, the patterns of net heat flux feedback resemble

those based on observations for most models (**Figure 6.5**); however, M_1, M_2 and M_9 show large biases compared with observations. Again, the net heat flux feedbacks for EP ENSO are rather robust in models, while large inter-model variations are seen for CP ENSO. This inconsistency might also be related to the large biases of model-simulated heat flux (Ferrett et al. 2017), which further influences the ENSO-related net heat flux feedback. Under a warmer background climate, the EP ENSO-related net heat flux feedback patterns are similar to those in the historical runs, but their intensity can be different (**Figure 6.6 a-i**). For CP ENSO-related net heat flux feedback, its magnitude change also varies among models; besides, its spatial pattern can be largely modified in some models (i.e. M_4 and M_9) (**Figure 6.6 j-r**).

The sensitivity maps of thermocline depth anomalies in response to ENSO-related SSTA are shown in **Figure 6.7** and **Figure 6.8**. It is obvious that EP ENSO-related thermocline feedbacks are rather consistent with observations. Observed negative (positive) κ values over the western-central Pacific (eastern Pacific), are well reproduced in these nine models, albeit with different feedback magnitudes in different models. In contrast, the CP ENSO thermocline feedback reveals large inter-model variations; only some models (i.e. M_1, M_2 and M_6) are incapable of simulating positive κ near the central Pacific. Based on simulations under RCP 8.5 scenario, the future patterns of thermocline feedback largely remain unchanged in models (**Figure 6.8**). However, both EP and CP ENSO-related thermocline feedbacks can be modified in term of their strength, as can be seen by comparing **Figure 6.8** and **Figure 6.7**.

To summarize, models' skills in reproducing various CP ENSO-related feedbacks are lower compared with those for EP ENSO, which might contribute to the large inconsistency of CP-type SSTA among models. In addition, the inter-model spread in the net heat flux feedback is relatively larger than the other two feedbacks, which might also contribute to discrepancies of

El Niño simulations in general. It is also notable that the EP and CP ENSO-related feedback strength can be modified, while their patterns tend to be unchanged due to global warming.

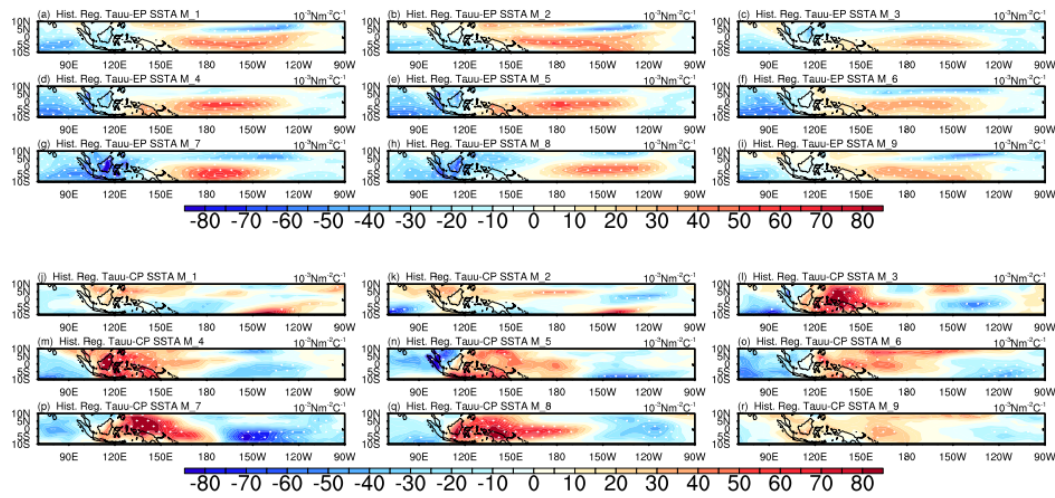


Figure 6.3 Sensitivity maps of zonal wind stress anomalies (units: 10^{-3}N/m^2) responses to (a-i) EP ENSO index (unit: $^{\circ}\text{C}$) and (j-r) CP ENSO index (unit: $^{\circ}\text{C}$) in 9 models from historical outputs (see text for more details). White dots denote the regression coefficients exceeding 95% confidence level.

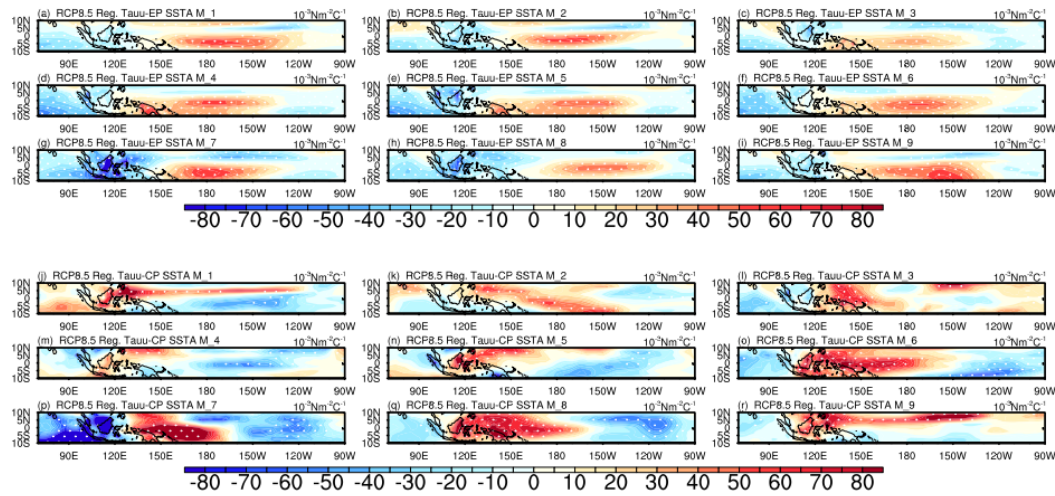


Figure 6.4 Same as **Figure 6.3**, but from the RCP8.5 scenario outputs.

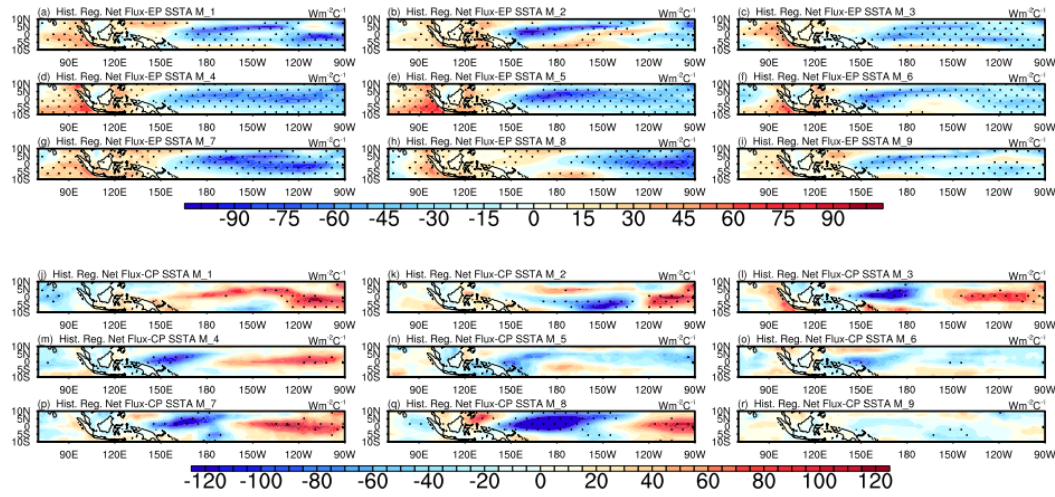


Figure 6.5 Sensitivity maps of net heat flux anomalies (units: W/m^2) responses to (a-i) EP ENSO index (unit: $^\circ\text{C}$) and (j-r) CP ENSO index (unit: $^\circ\text{C}$) in 9 models from historical outputs. Black dots denote the regression coefficients exceeding 95% confidence level.

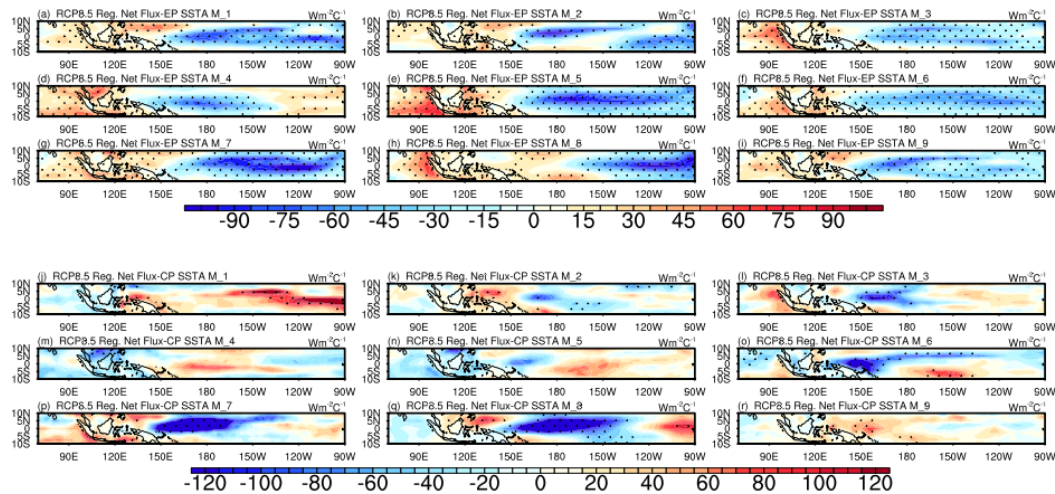


Figure 6.6 Same as **Figure 6.5**, but from the RCP8.5 scenario outputs.

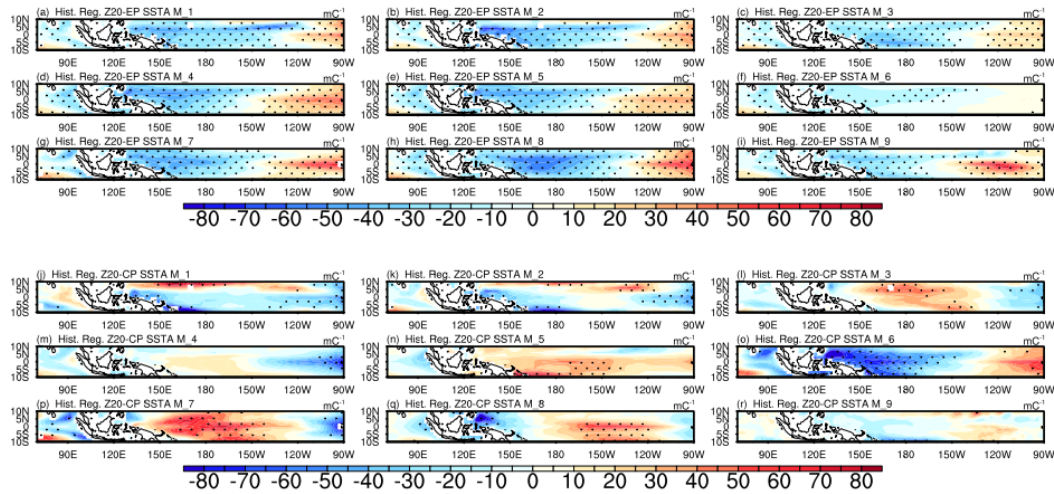


Figure 6.7 Sensitivity maps of thermocline depth anomalies (units: m) responses to (a-i) EP ENSO index (unit: °C) and (j-r) CP ENSO index (unit: °C) in 9 models from historical outputs. Black dots denote the regression coefficients exceeding 95% confidence level.

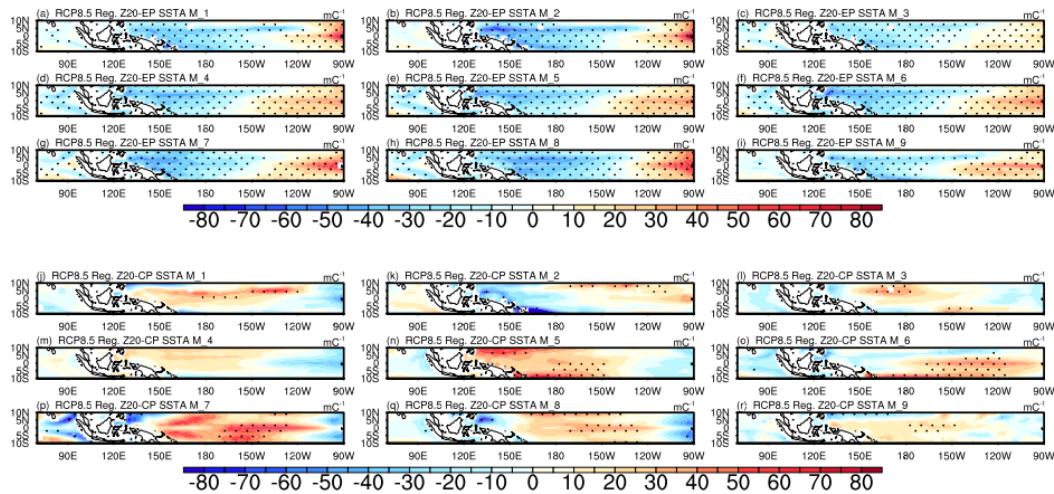


Figure 6.8 Same as **Figure 6.7**, but from the RCP8.5 scenario outputs.

To quantify the atmospheric feedback, heat flux feedback, and thermocline feedback for EP and CP ENSO, the corresponding feedback parameters (i.e. μ , α and κ) are first averaged over 10°S–10°N. Next, centroids of present-day and future $\bar{\mu}$, $\bar{\alpha}$ and $\bar{\kappa}$ defined respectively as:

$$A = \frac{\int \bar{\mu}(x)xdx}{\int \bar{\mu}(x)dx} \quad (6.1)$$

$$B = \frac{\int \bar{\alpha}(x)xdx}{\int \bar{\alpha}(x)dx} \quad (6.2)$$

$$C = \frac{\int \bar{\kappa}(x)xdx}{\int \bar{\kappa}(x)dx} \quad (6.3)$$

(where $\bar{\mu}(x)$, $\bar{\alpha}(x)$ and $\bar{\kappa}(x)$ denotes the meridional-averaged ENSO-related equatorial feedbacks, x being the longitude), are computed. The integrations, regarding these feedbacks, are executed over different regions for different types of ENSO (see **Table 6.1** for details). Note that negative values of $\bar{\mu}(x)$ and $\bar{\kappa}(x)$, and positive values of $\bar{\alpha}(x)$ are excluded in the integral equations 6.1-6.3. To interpret the magnitude change of ENSO-related feedbacks, differences between the values of future and present-day $\bar{\mu}(x)$, $\bar{\alpha}(x)$ and $\bar{\kappa}(x)$ evaluated at A , B and C are used, respectively.

The changes in magnitude of EP vs. CP ENSO-related feedbacks are further shown in **Figure 6.9**. It is obvious that the feedback changes for two types of ENSO are positively correlated; the correlation coefficient reaches 0.68 (exceeds 98% confidence level) for atmospheric feedback, 0.15 for heat flux feedback and 0.60 (exceeds 95% confidence level) for thermocline feedback, respectively. Hence, the strength changes of these feedbacks due to global warming, for EP and CP ENSO, behave in a coherent way. This result verifies the hypothesis that EP and CP El Niño simulated by models, to a large extent, are modulated by the same physical processes. The feedbacks, under a warmer climate, are changed in a similar trend and determine the future change of El Niño. It is also noticed that the positive correlation between EP and CP ENSO-related heat flux feedback changes is insignificant

compared with the other two feedback changes. This might be related to the diverse damping effects for CP ENSO among these models; in other words, the change of CP ENSO-related net heat flux feedback is sensitive to the calculation method applied to each individual models.

Figure 6.10 gives the relationships between ocean-atmosphere feedback and El Niño SSTA changes. It is noticed that the thermocline feedback and atmospheric feedback changes are positively correlated with the SSTA changes for both types of ENSO. These two feedback changes, for both EP and CP ENSO, have the same sign in most models. This implies that a stronger thermocline feedback and atmospheric feedback correspond to a stronger Bjerknes feedback, which tend to enhance ENSO variability. However, the net heat flux feedback changes for EP and CP ENSO are negatively correlated with the SSTA changes; that is, a stronger damping effects are even related to a stronger ENSO variability. Therefore, the changes of SSTA might be dominated by the changes of Bjerknes feedback. In particular, both EP and CP El Niño are enhanced markedly in the future climate based on M_6, accompanying remarkable intensification of the thermocline feedback and atmospheric feedback; for M_3 and M_4, the weakened EP and CP El Niño correspond to prominently reduced thermocline feedback and atmospheric feedback. However, the indicative role of thermocline feedback and atmospheric feedback is not applicable to all these models. Thus, the ocean-atmosphere feedbacks for two types of ENSO warrant more detailed analyses by using multiple approaches.

Table 6.1 The longitude ranges of x (see equations 6.1, 6.2 and 6.3) for different ocean-atmosphere feedbacks in terms of EP and CP ENSO.

Longitude Range for Integration	EP Type ENSO	CP Type ENSO
Atmospheric Feedback	150°E–120°W	100°E–150°W
Net Heat flux Feedback	150°E–90°W	100°E–150°W
Thermocline Feedback	150°W–90°W	120°E–120°W

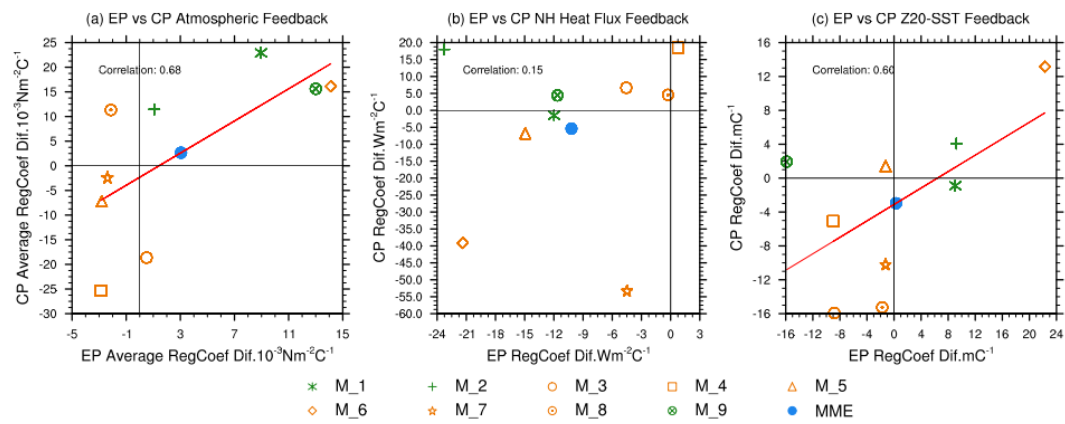


Figure 6.9 Scatter plots of EP and CP ENSO-related (a) atmospheric feedback changes (units: $10^{-3} \text{Nm}^2 \text{K}^{-1}$), (b) heat flux feedback changes (units: $\text{Wm}^{-2} \text{C}^{-1}$) and thermocline feedback changes ($\text{m}^\circ \text{C}^{-1}$) (see text for more details) in group A-1 (markers in orange) and B-1 (markers in green). The blue dots indicate the MME mean based on all the nine selected models.

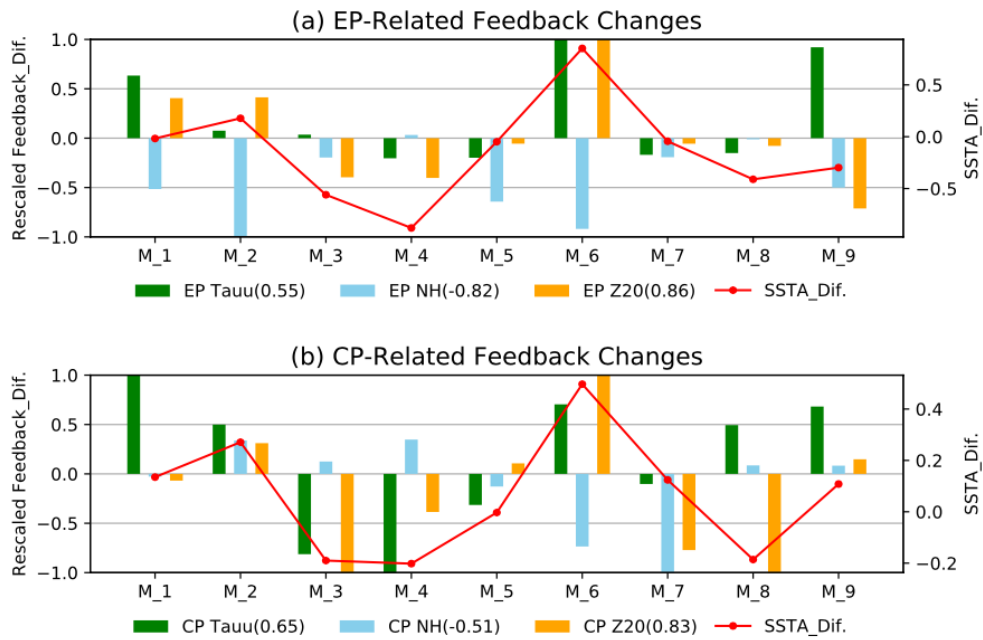


Figure 6.10 Bar charts of the rescaled (a) EP ENSO-related and (b) CP ENSO-related atmospheric feedback (green bar), net heat flux feedback (blue bar) and thermocline feedback (yellow bar) changes based on the nine selected models. The red line indicates the future changes of EP and CP El Niño SSTA (units: °C). Numbers in the brackets indicate the correlations between feedback and SSTA changes. Note that the atmospheric feedback changes and thermocline feedback changes (net heat flux feedback changes) are rescaled by dividing their corresponding maximum (minimum) value among these nine models for rescaling.

7 Conclusion and Discussion

The overarching aim of this thesis is to provide a better understanding of El Niño diversity and its related rainfall anomalies under global warming. It is motivated by the improvement of CMIP5 models in simulating El Niño diversity and relatively robust enhancement of El Niño-driven rainfall anomalies under global warming. With intensive analyses on the state-of-the-art CMIP5 models and complementary AGCM experiments, the four research questions proposed in Chapter 1 have been answered in this thesis. Here, a conclusion and discussion of each result chapter are presented, highlighting the main findings and novel contributions to the field.

7.1 Performance of CMIP5 models in simulating present-day El Niño-EA rainfall teleconnection and its diversity

CMIP5 models' fidelity in simulating El Niño diversity and EA rainfall variability has been improved during the past decade, but with relatively few studies have focused on their teleconnection diversity. Taking the Walker circulation anomalies as a proxy to describe the El Niño-related SSTA, it is found that while all of the 17 selected models, which are capable in simulating El Niño diversity, well represent the EP El Niño-related anomalous atmospheric circulation due to robust inter-model consistency of EP-type SSTA; some model members show large biases for the same circulation elements when CP El Niño occurs due to their lower skill in simulating CP-type SSTA. In particular, unrealistic CP El Niño-induced Walker cell anomalies exist in 6 out of the 17 models with erroneous rising motion in the equatorial western Pacific, due to the westward shift of CP-type SSTA. For the remaining 11 models, which simulate reasonable CP-type SSTA, the corresponding Walker circulation anomalies are faithfully reproduced. Thus, the critical role of SSTA in determining the

overturning circulation anomalies implies that the large inter-model spread of CP-type SSTA should be taken into consideration for further studies on diverse El Niño-rainfall teleconnection. Therefore, the simulation of CP El Niño in models warrants thorough studies from the community.

Regarding the model-simulated anomalous precipitation and low-level wind during two types of El Niño, contrasting atmospheric responses to CP El Niño are found among the models with higher and lower skills in capturing the CP-type SSTA. Due to distinct location of Gill-type responses, CP El Niño-related dryer (wetter)-than-normal conditions over SCS (at $\sim 150^{\circ}\text{N}$) from DJF(1) to JJA(1) can merely be captured based on skillful models; while unrealistic surplus rainfall over SCS, accompanying cyclonic circulation anomalies in the low level, are simulated based on less skillful models. On the other hand, rainfall and low-level circulation anomalies that related to EP El Niño from the developing summer to the decaying summer are well reproduced by both sets of models. The “Indian Ocean capacitor” effect, which contributes to the persistence of the anomalous WNP anticyclone when the EP-type warming already decayed, gives rise to enhanced EASM during the decaying summer. Thus, the simulations of El Niño-EA rainfall teleconnection and its diversity in coupled models highly rely on the model-simulated El Niño SSTA. These imply again that the reduction of inter-model biases in simulating CP El Niño-driven rainfall anomalies should center on the improvement of CP-type SSTA simulation.

The linkage between mean state of SST and El Niño simulation in CMIP5 models is emphasized in Chapter 3. It is found that CP El Niño and its related overturning circulation are sensitive to the common eastern Pacific cold tongue bias. Colder mean SST over the eastern Pacific might facilitate more upwelling of cold water and lead to a westward shift of CP El Niño-related SSTA, and hence affecting the El Niño-driven teleconnections. These results also highlight the importance of reducing excessive cold tongue biases in coupled

models for a more realistic representation of El Niño diversity. Additionally, it is envisaged that the dynamics of CP El Niño warrant further investigations, to find out what factors are exactly responsible for the lower skill of coupled models in simulating CP El Niño. Comparing the skillful and less skillful models with respect to CP El Niño-related ocean-atmosphere feedbacks might provide some insights into the improvement of the CP El Niño simulation.

7.2 El Niño-EA rainfall teleconnection and its diversity in a warmer climate

The El Niño-EA rainfall teleconnection and its diversity under present climate can be realistically reproduced by part of the CMIP5 coupled models. To provide a further understanding of their future changes in a warmer climate, the “best” models which are capable in simulating both El Niño diversity and EASM variability are selected by intensive evaluations of EASM climatology and interannual variability simulated by CMIP5 models. In this thesis, the MME mean of present-day and future El Niño-related EA rainfall anomalies based on six “best” models are compared. It is verified that the patterns of both EP and CP El Niño-driven rainfall and low-level wind anomalies largely persist under global warming. More intriguing changes are the significantly enhanced variation of rainfall anomalies over EA region during the developing summer, mature winter and decaying summer (mature winter and decaying summer) for EP (CP) El Niño. It is also noticed that the global warming effect seems to be more influential in enhancing the CP El Niño-related rainfall variations since the ratio of rainfall increase is higher than that for EP El Niño.

Inspections of individual models reveal no consensus on the changes of El Niño SSTA and its corresponding circulation in the future climate; large inter-model spreads of these variables are given for both types of El Niño. Hence rather small MME mean values might be related

to the mutual cancellation between model signals. In addition, it is obvious that El Niño-induced low-level circulation changes under global warming follow those of the strength and location of El Niño. Even though stronger or weaker El Niño might be projected in different models, the CP El Niño-related rainfall, with relatively moderate CP-type SSTA change, will be enhanced robustly under global warming; same for EP El Niño unless its related SSTA is massively weakened. The abovementioned results are based on coupled CMIP5 models, AGCM experiments carried out in this thesis further verify the fact that El Niño-induced rainfall variations over the deep tropics will be enhanced with warmer mean state of SST and strengthened radiative forcing; an eastward shift of the El Niño-related equatorial tropical rainfall anomalies can be simulated by AGCM experiments, which might due to the drift of mean tropical convection and time-mean precipitation.

These results all point to more variable El Niño-driven rainfall under global warming, implying a higher chance of EA region to be influenced by El Niño-related rainfall extremes. Given a higher ratio of enhanced rainfall variations for CP El Niño, this study not only provides a complement to the future state of El Niño-related rainfall but also emphasize the necessity for taking care of CP El Niño impacts in the future climate.

In this thesis, the diversity of ENSO-EA rainfall teleconnection in the future climate is adequately studied but only focus on El Niño events. The relationship between La Niña and EA rainfall is not a major concern mainly because of the near-absence of La Niña diversity in observations (Timmermann et al. 2018). The SST and precipitation associated with two types of La Niña events are much less distinctive or less independent (Kug and Ham 2011). Therefore, La Niña diversity warrants future studies. Besides, the asymmetric responses of El Niño and La Niña-driven rainfall anomalies under global warming should also be investigated in future studies.

The subtropical western North Pacific (WNP), controlled by high pressure system associated with anticyclonic circulation in the mid and lower troposphere, also regulates the EA rainfall variability. The potential change of WNP subtropical high (WNPSH) under global warming might also be important for future change of EASM. A recent study pointed that the WNPSH tends to weaken and retreat eastward in the mid-troposphere in response to global warming, accompanied by an eastward expansion of East Asian rain belt along the northwestern flank of WNPSH (He et al. 2015). However, the integral impacts of WNPSH and two types of El Niño under global warming are still unknown and warrant future studies.

7.3 Physical processes responsible for the two types of El Niño-related rainfall changes under global warming

A partitioning framework is introduced in this thesis to evaluate the contributions of perturbed moisture in the atmosphere as well as the El Niño-driven circulation anomalies in determining the future El Niño-related rainfall variations. Based on the MME mean of best models, the El Niño-induced moisture flux convergence/divergence changes are consistent with the corresponding rainfall changes. The total moisture flux convergence is dominated by the dynamic term, while the thermodynamic term is of secondary importance. Importantly, the change of El Niño-related moisture flux transport is more likely a balance of two partitioned dynamic terms, with perturbations of circulation anomalies acting on present-day specific humidity, and future circulation anomalies acting upon perturbations of specific humidity, respectively. In the former one, a weaker or stronger El Niño-related circulation can be simulated during different El Niño phases, corresponding to a weakened or strengthened moisture flux convergence. In the latter one, a moister atmosphere under global warming tends to robustly strengthen the moisture flux, which serves a positive role in enhancing rainfall variations during all El Niño phases. Thus, a competing effect or a

cooperative effect of these two terms leads to the moisture flux transport changes. In particular, the mean moisture enhancement can offset the effect of weaker circulation anomalies during most El Niño phases, resulting in the intensification of rainfall variations. Again, individual model inspections interpret that the rainfall variations are likely to be weaker only if a massively weaker EP El Niño is projected, while tend to be stronger in models with moderately modified EP El Niño. For CP El Niño, the rainfall variations in all models tend to be stronger regardless of their relatively weak SSTA changes. Thus, the future change of rainfall variations in individual models should also be a balance of moisture flux transport due to the perturbations of mean moisture and El Niño-related circulation.

In this thesis, moisture budget analyses on AGCM experiments are also conducted to better delineate the underlying physical mechanisms. Results show that the general patterns of EP and CP El Niño-related moisture flux and its convergence coincide with the anomalous rainfall over deep tropics under global warming, consistent with that in the CMIP5 coupled models. Moisture budget decomposition gives rather consistent results that the dynamic term dominates the changes in total moisture flux, for which the moisture flux due to perturbed El Niño-related circulation and mean moisture are all responsible for the tropical El Niño-related rainfall changes. However, the effect due to the former one is stronger than that due to the latter one. The former effect contributes to both amplitude enhancement and shift of El Niño-related rainfall, while the latter effect is merely related to the intensification of present-day El Niño-driven rainfall pattern. More importantly, the moisture flux and its convergence changes due to El Niño-related circulation can be stronger even with identical El Niño forcing in a warmer background.

Based on coupled and atmosphere-only model simulations, it is concluded that the two types of El Niño-driven rainfall variabilities are highly possible to be enhanced under a warmer climate. Three factors should be taken into consideration here: Firstly, the enhancement of

the mean moisture will robustly play a positive role in enhancing the rainfall variations projected onto the same anomalous rainfall pattern. Secondly, the warmer climate tends to intensify the El Niño-driven circulation anomalies by a “nonlinear” response to different background climate states. Thirdly, the El Niño-related circulation changes are positively correlated with the corresponding SSTA changes, only massively weakened SSTA can lead to the weakened rainfall variations even with enhanced mean moisture and stronger circulation responses to El Niño forcing under global warming. It is also noteworthy that the dynamic_advection term (i.e. $\frac{1}{g\rho_w} \nabla \cdot \int_{p_s}^{p_t} \vec{V}_F' \delta(q_c) dp$) corresponds to “wet gets wetter, dry gets drier” mechanism which indicates the current rainfall pattern will be enhanced under the assumption of unchanged circulation. In fact, El Niño-related circulation can be modified under global warming. Thus, the dynamic_divergence term (i.e. $\frac{1}{g\rho_w} \nabla \cdot \int_{p_s}^{p_t} q_{cH} \delta(\vec{V}') dp$) emphasizes the impacts of perturbed circulation anomalies on moisture flux and its convergence/divergence. In this way, a more deliberate moisture flux decomposition is given in this thesis.

It is noticed that the circulation responses to El Niño under warmer background climate are stronger in AGCM relative to those from the MME mean of CMIP5 coupled models (see also **Figure 7.1** for more details). This might explain the reason why the changes in moisture flux transport due to dynamic_divergence term is much stronger than that due to the dynamic_advection term based on AGCM simulations, while relatively comparable in CMIP5 models (see Chapter 4) for these two terms. It's possible that ocean-atmosphere coupling processes tend to weaken the atmospheric responses to El Niño forcing under global warming; the circulation responses to El Niño in CAM4 might be too strong relative to other models. According to the AGCM experiments, the circulation response to El Niño seems to be sensitive to changes in basic SST, but not to changes in El Niño-related SSTA. This might

be related to the El Niño-like warming in the eastern Pacific due to global warming which is much larger than the changes in El Niño SSTA (note that the change of SSTA based on MME mean is relatively small for two types of El Niño; see **Figure 4.21** for more details). Besides, three additional experiments were designed to test the sensitivity of El Niño-induced circulation anomalies to SSTA change.

Table 7.1 Design of three additional sets of AGCM experiments. 0.8 and 1.5 indicate that the El Niño-related SSTA are reduced and enlarged by 0.8 and 1.5 times, respectively.

	Historical El Niño SSTA*0.8	Historical El Niño SSTA*1.5
Historical mean SST and CO₂	Exp1_EP_0.8	Exp1_EP_1.5
	Exp1_CP_0.8	Exp1_CP_1.5
Future mean SST and CO₂	Exp2_EP_0.8	
	Exp2_CP_0.8	

Based on Exp1_EP_0.8 (Exp1_EP_1.5) and Exp1_CP_0.8 (Exp1_CP_1.5), it is verified that a weakened (amplified) El Niño SSTA corresponds to a weaker (stronger) circulation response (figures not shown). Comparing Exp1_EP_0.8 (Exp1_CP_0.8) and Exp2_EP_0.8 (Exp2_CP_0.8), it is noticed that both sets of experiment tend to give a weaker circulation response under both present-day and future basic state. However, the decrease of circulation response in Exp2_EP(CP)_0.8 is relatively smaller than that in Exp1_EP(CP)_0.8 (figures not shown). The abovementioned implies that the AGCM-simulated El Niño-driven circulation anomalies are still largely determined by the SSTA, but with the modulation of climate basic state. Thus, the response of circulation to SSTA simulated by AGCM is roughly consistent with their linear relationship in CMIP5 models.

To summarize, the future changes in two types of El Niño-related rainfall are rather complex; the interactions between El Niño-driven circulation anomalies and mean state are still not fully understood which warrant further studies.

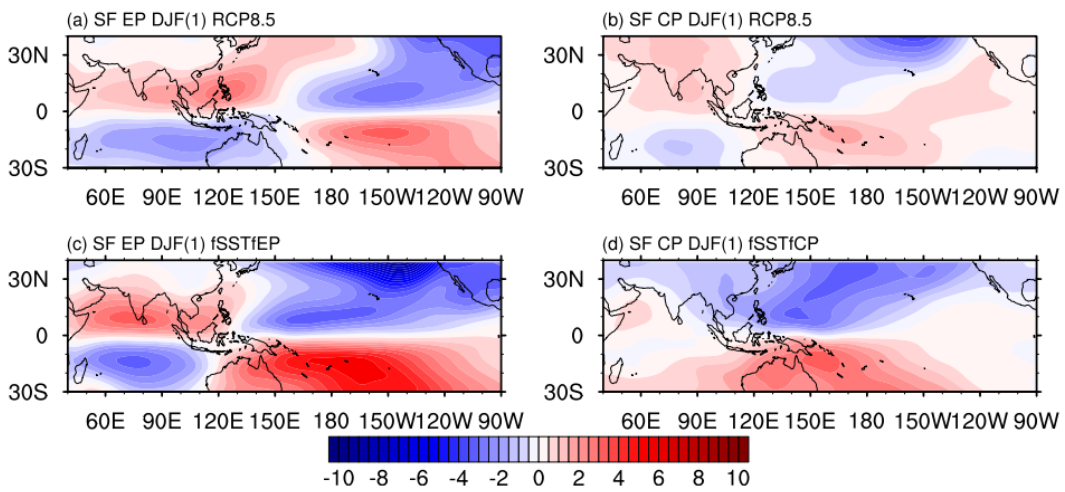


Figure 7.1 Stream function anomalies (shading; see scale bar at bottom in units of $10^6 \text{ m}^2 \text{ s}^{-1}$) based on the (a, b) MME mean of coupled models in group A-1 and (c, d) AGCM simulations in Exp4 during DJF(1) for (a, c) EP and (b, d) CP El Niño. Note that the EP and CP El Niño SSTA in Exp4 is identical with the MME mean of corresponding SSTA based on group A-1 models.

7.4 Modulation of two types of El Niño due to global warming

The performances of coupled models in simulating realistic El Niño diversity, which have a large influence on the simulated El Niño-EA rainfall teleconnection and its diversity at present-day and in the future, have been emphasized in the thesis. However, there is no consensus on how two types of El Niño will be modified as inferred from the nine selected models since weaker or stronger El Niño can be projected with a west-east shift of the warming center. Even so, the intensity and location changes of EP and CP El Niño reveal marked coherence. This implies that similar physical processes are dominating the El Niño evolution and its future change. In this study, the performances of models in simulating these feedback processes under present-day and future climate were examined. In particular, the atmospheric feedback, heat flux feedback, and thermocline feedback changes associated with EP and CP ENSO are positively correlated, which might be responsible for the coherent changes of the EP and CP-type SSTA. However, the correlation coefficients for atmospheric feedback and thermocline feedback are significant, but insignificant for heat flux feedback; this implies larger inconsistency of heat flux feedback among these models. As shown in Chapter 3, the simulation of CP El Niño is still challenging for state-of-the-art climate models. It is noticed that the physical processes responsible for CP El Niño have large inter-model variations, which might give rise to the lower skill of CP El Niño simulation. In addition, CP ENSO-related feedbacks in group A-1 models seem to bear higher resemblance to observations compared with those in group B-1 models. This might be related to the higher performances of group A-1 models in reproducing the CP-type El Niño. Certainly, the inter-model spread of CP-type SSTA might also arise from an incomplete CP ENSO formation mechanism in models or low skill of models in capturing the stochastic forcing (i.e. extropical atmospheric forcing (Yu et al. 2010; Yu and Kim 2011) and westerly wind event

burst (Chen et al. 2015a)), which can initiate CP El Niño events. It is also noteworthy that the intensity change of thermocline feedback and atmospheric feedback coincides with the change of El Niño amplitude for some models (especially models with large intensity change); this result provides a valuable hint for future El Niño projections.

Appendix

A1 Details of moisture budget decomposition

For historical and future runs in each model, original values of monthly mean wind velocity and specific humidity during El Niño can be expressed as $\vec{V} = \vec{V}_c + \vec{V}'$ and $q = q_c + q'$, respectively, where \vec{V}_c and q_c denote their climatologies in each model, \vec{V}' and q' represent the respective deviations due to El Niño from the corresponding climatology of each model. Thus, the moisture transport in equation 2.2 can be expanded as:

$$\begin{aligned} -\nabla \cdot \vec{Q} &= -\frac{1}{g\rho_w} \nabla \cdot \int_{p_s}^{p_t} (q \vec{V}) dp = -\frac{1}{g\rho_w} \nabla \cdot \int_{p_s}^{p_t} (q_c + q') (\vec{V}_c + \vec{V}') dp \\ &= -\left(\frac{1}{g\rho_w} \nabla \cdot \int_{p_s}^{p_t} (q_c \vec{V}_c) dp + \frac{1}{g\rho_w} \nabla \cdot \int_{p_s}^{p_t} (q' \vec{V}_c) dp + \frac{1}{g\rho_w} \nabla \cdot \int_{p_s}^{p_t} (q_c \vec{V}') dp \right. \\ &\quad \left. + \frac{1}{g\rho_w} \nabla \cdot \int_{p_s}^{p_t} (q' \vec{V}') dp \right) \quad (A1.1) \end{aligned}$$

The two terms, $\frac{1}{g\rho_w} \nabla \cdot \int_{p_s}^{p_t} (q_c \vec{V}') dp$ (relating to dynamic effect) and $\frac{1}{g\rho_w} \nabla \cdot \int_{p_s}^{p_t} (q' \vec{V}_c) dp$ (relating to thermodynamic effect), are major contributors to the deviations of moisture transport in the models, while the term by transient eddies $\frac{1}{g\rho_w} \nabla \cdot \int_{p_s}^{p_t} (q' \vec{V}') dp$ is neglectable since both q' and \vec{V}' are small deviations from their climatologies, and $\frac{1}{g\rho_w} \nabla \cdot \int_{p_s}^{p_t} (q_c \vec{V}_c) dp$ is stationary within the simulation period chosen. Finally, the El Niño-related anomalous moisture transport can be expressed as:

$$\begin{aligned} -\nabla \cdot \vec{Q}' &= -\frac{1}{g\rho_w} \int_{p_s}^{p_t} \nabla \cdot (q \vec{V})' dp \\ &\approx -\left(\frac{1}{g\rho_w} \int_{p_s}^{p_t} \nabla \cdot (q' \vec{V}_c) dp + \frac{1}{g\rho_w} \int_{p_s}^{p_t} \nabla \cdot (q_c \vec{V}') dp \right) \quad (A1.2) \end{aligned}$$

Thus, we can have the anomalous moisture transport and its dynamical and thermodynamical component for both types of El Niño under present and future scenarios.

I

Denoting

$$\delta(\cdot) = (\cdot)_F - (\cdot)_H \quad (A1.3)$$

where subscripts F and H indicate the MME mean values from RCP 8.5 scenario simulations and historical simulations in parentheses. δ represent the deviations due to global warming.

Then, the future changes of anomalous moisture transport can be approximated as:

$$\begin{aligned} & \frac{1}{g\rho_w} \delta \left(\nabla \cdot \int_{p_s}^{p_t} (q \vec{V})' dp \right) \\ & \approx \frac{1}{g\rho_w} \delta \left(\nabla \cdot \int_{p_s}^{p_t} (q' \vec{V}_c) dp \right) + \frac{1}{g\rho_w} \delta \left(\nabla \cdot \int_{p_s}^{p_t} (q_c \vec{V}') dp \right) \quad (A1.4) \end{aligned}$$

Also, the changes of dynamic effect (thermodynamic effect) under different climate background can be further decomposed into two terms (Seager et al. 2010; Wang et al. 2017b), referring to the changes of El Niño-related wind circulation anomalies (moisture anomalies) and mean state of moisture (wind circulation) in the atmosphere as follows:

$$\frac{1}{g\rho_w} \delta \left(\nabla \cdot \int_{p_s}^{p_t} (q_c \vec{V}') dp \right) = \frac{1}{g\rho_w} \nabla \cdot \int_{p_s}^{p_t} q_{cH} \delta(\vec{V}') dp + \frac{1}{g\rho_w} \nabla \cdot \int_{p_s}^{p_t} \vec{V}'_F \delta(q_c) dp \quad (A1.5)$$

$$\frac{1}{g\rho_w} \delta \left(\nabla \cdot \int_{p_s}^{p_t} (q' \vec{V}_c) dp \right) = \frac{1}{g\rho_w} \nabla \cdot \int_{p_s}^{p_t} \vec{V}_{cH} \delta(q') dp + \frac{1}{g\rho_w} \nabla \cdot \int_{p_s}^{p_t} q'_F \delta(\vec{V}_c) dp \quad (A1.6)$$

where the subscripts cF and cH represent the climatologies in RCP 8.5 scenario and historical simulations, respectively.

Based on the abovementioned moisture decomposition, equation 2.6 can be transformed as follow:

II

$$\begin{aligned}
\iint \delta(P' \widehat{P}') dx dy &= \iint -\frac{1}{g\rho_w} \delta(\phi((q \vec{V})' \widehat{P}')) dx dy + \iint \delta(E' \widehat{P}') dx dy \\
&= \iint \left(-\frac{1}{g\rho_w} \left(\delta(\phi(q' \vec{V}_c) \widehat{P}') - \frac{1}{g\rho_w} \delta(\phi(q_c \vec{V}') \widehat{P}') \right) \right) dx dy \\
&\quad + \iint \delta(E' \widehat{P}') dx dy \\
&= \iint \left(-\frac{1}{g\rho_w} \phi(q_{ch} \delta(\vec{V}')) \right) \widehat{P}'_H dx dy + \iint \left(-\frac{1}{g\rho_w} \phi(\vec{V}'_F \delta(q_c)) \right) \widehat{P}'_H dx dy \\
&\quad + \iint \left(-\frac{1}{g\rho_w} \phi(\vec{V}_{ch} \delta(q')) \right) \widehat{P}'_F dx dy + \iint \left(-\frac{1}{g\rho_w} \phi(q'_F \delta(\vec{V}_c)) \right) \widehat{P}'_F dx dy \\
&\quad + \iint \delta(E' \widehat{P}') dx dy \quad (A1.7)
\end{aligned}$$

where $\phi(\cdot) = \nabla \cdot \int_{p_s}^{p_t} (\cdot) dp$ is defined for simplicity and assume \widehat{P}'_H and \widehat{P}'_F are identical with each other. Thus, the relative contributions of the different moisture transport processes in determining the future changes of El Niño-related rainfall anomalies can be quantified and compared.

A2 Kernel Density Estimation

In Chapter 3, kernel density estimation (KDE) was applied to the El Niño-related Walker circulation locations in 17 selected models. KDE is a non-parametric way to estimate the probability density of a random variable. Let $(x_1, x_2, x_3, \dots, x_n)$ be a univariate independent sample with a density function f . To estimate the shape of this function f , its kernel density estimator is written as:

$$f_h(x) = \frac{1}{n} \sum_{i=1}^n K_h(x - x_i) = \frac{1}{nh} \sum_{i=1}^n K\left(\frac{x - x_i}{h}\right) \quad (A2.1)$$

where K is the kernel-a non-negative function, and h is a smoothing parameter called the bandwidth. For the kernel function, uniform, triangular, quartic, Epanechnikov, normal and

other functions are commonly used. Here, the normal kernel is used, which means $K(x) = \phi(x)$, where ϕ is the standard normal density function. The bandwidth h , corresponding to normal kernel, can be approximated as:

$$h = \left(\frac{4\hat{\sigma}^5}{3n} \right)^{\frac{1}{5}} \approx 1.06\hat{\sigma}n^{-\frac{1}{5}} \quad (A2.2)$$

where $\hat{\sigma}$ is the standard deviation of the samples (Silverman 1986).

Kernel density estimations are closely related to histograms, but can be endowed with properties such as smoothness or continuity by using suitable kernel (see link https://en.wikipedia.org/wiki/Kernel_density_estimation and Silverman 1986 for more details about KDE).

A3 Taylor diagram

Taylor diagram has been devised in Taylor (2001) to provide a concise statistical summary of how well patterns match each other in terms of their correlation, root-mean-square difference, and the ratio of their variances. This diagram has been widely used to evaluate climate models, such as their performances in reproducing geophysical phenomena. The theoretical basis for Taylor diagram is given in Taylor (2001). Here, a brief description is shown as below.

Consider two variables, f_n and r_n defined at N discrete points in time and/or space, their correlation coefficient R can be expressed as

$$R = \frac{\frac{1}{N} \sum_{n=1}^N (f_n - \bar{f})(r_n - \bar{r})}{\sigma_f \sigma_r} \quad (A3.1)$$

where \bar{f} and \bar{r} are mean values, σ_f and σ_r for standard deviations of f and r , respectively.

The root-mean-square (RMS) difference is often used to quantify differences in two fields which can be written as

IV

$$E = \left[\frac{1}{N} \sum_{n=1}^N (f_n - r_n)^2 \right]^{1/2} \quad (A3.2)$$

The differences in the means of the two fields can be isolated from the differences in the patterns, the overall “bias” is defined as

$$\bar{E} = \bar{f} - \bar{r} \quad (A3.3)$$

and the RMS error (RMSE), with the overall bias removed, can be defined by

$$E' = \left\{ \frac{1}{N} \sum_{n=1}^N [(f_n - \bar{f}) - (r_n - \bar{r})]^2 \right\}^{1/2} \quad (A3.2)$$

(Note that the means of the fields are subtracted out before computing their second-order statistics, so the diagram does not provide information about overall biases, but solely characterizes the centered pattern error.) The correlation coefficient, RMS error (RMSE) and standard deviation provide statistical information quantifying the correspondence between two patterns. Here, the relationship between these three statistics is given by

$$E'^2 = \sigma_f^2 + \sigma_r^2 - 2\sigma_f\sigma_r R \quad (A3.4)$$

In this thesis, the standard deviations and RMSE shown in Taylor diagram are normalized by the standard deviation of the observed fields. That is, the standard deviations of observed field is one. Thus, the above equation can be rescaled as

$$\frac{E'}{\sigma_r}^2 = \frac{\sigma_f^2}{\sigma_r^2} + 1 - \frac{2\sigma_f R}{\sigma_r} \quad (A3.5)$$

Figure A3.1 gives a sample of Taylor diagram displaying pattern statistics. The radial distance from origin to a point (i.e. testing point) is proportional to σ , the azimuthal position gives the correlation between the reference and the test field. Dashed line measures RMSE (i.e. distance from reference to test data) (Taylor 2001). In general, a closer distance to the reference indicates higher resemblance of the test field compared with the reference field.

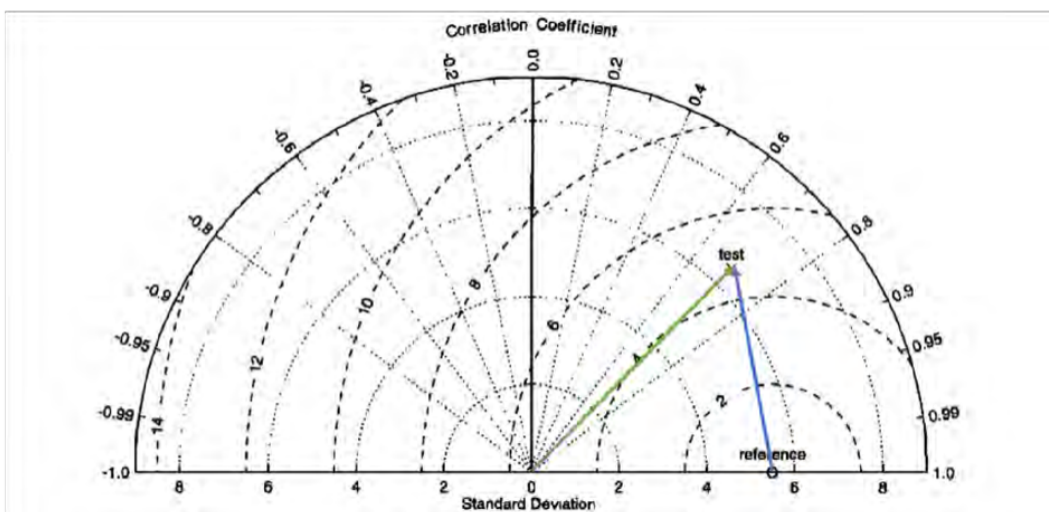


Figure A3.1 Taylor diagram displaying a statistical comparison between the test and reference field. From Taylor (2001).

Bibliography

- An, S. Il, E. S. Heo, and S. T. Kim, 2017: Feedback process responsible for intermodel diversity of ENSO variability. *Geophys. Res. Lett.*, **44**, 4272–4279, doi:10.1002/2017GL073203.
- Ashok, K., S. K. Behera, S. A. Rao, H. Weng, and T. Yamagata, 2007: El Niño Modoki and its possible teleconnection. *J. Geophys. Res.*, **112**, doi:10.1029/2006jc003798.
- Bayr, T., M. Latif, D. Dommenget, C. Wengel, J. Harlaß, and W. Park, 2018: Mean-state dependence of ENSO atmospheric feedbacks in climate models. *Clim. Dyn.*, **50**, 3171–3194, doi:10.1007/s00382-017-3799-2.
- , D. I. V. Domeisen, and C. Wengel, 2019: The effect of the equatorial Pacific cold SST bias on simulated ENSO teleconnections to the North Pacific and California. *Clim. Dyn.*, **16**, doi:10.1007/s00382-019-04746-9.
- Behringer, D., and Y. Xue, 2004: *Evaluation of the global ocean data assimilation system at NCEP: The Pacific Ocean. Eighth Symposium on Integrated Observing and Assimilation Systems for Atmosphere, Oceans, and Land Surface, AMS 84th Annual Meeting, Washington State Convention and Trade*. 11–15 pp.
- Bellenger, H., E. Guilyardi, J. Leloup, M. Lengaigne, and J. Vialard, 2014: ENSO representation in climate models: From CMIP3 to CMIP5. *Clim. Dyn.*, **42**, 1999–2018, doi:10.1007/s00382-013-1783-z.
- Bonfils, C. J. W., B. D. Santer, T. J. Phillips, K. Marvel, L. Ruby Leung, C. Doutriaux, and A. Capotondi, 2015: Relative contributions of mean-state shifts and ENSO-driven variability to precipitation changes in a warming climate. *J. Clim.*, **28**, 9997–10013, doi:10.1175/JCLI-D-15-0341.1.

- Cai, W., and Coauthors, 2015a: ENSO and greenhouse warming. *Nat. Clim. Chang.*, **5**, 849, doi:10.1038/nclimate2743. <http://dx.doi.org/10.1038/nclimate2743>.
- , and Coauthors, 2015b: Increased frequency of extreme La Niña events under greenhouse warming. *Nat. Clim. Chang.*, **5**, 132–137, doi:10.1038/nclimate2492.
- , and Coauthors, 2018: Increased variability of eastern Pacific El Niño under greenhouse warming. *Nature*, **564**, 201–206, doi:10.1038/s41586-018-0776-9.
- Carton, J. A., and B. S. Giese, 2008: A Reanalysis of Ocean Climate Using Simple Ocean Data Assimilation (SODA). *Mon. Weather Rev.*, **136**, 2999–3017, doi:10.1175/2007mwr1978.1.
- Chadwick, R., I. Boutle, and G. Martin, 2013: Spatial patterns of precipitation change in CMIP5: Why the rich do not get richer in the tropics. *J. Clim.*, **26**, 3803–3822, doi:10.1175/JCLI-D-12-00543.1.
- Chang, C. P., Y. Zhang, and T. Li, 2000: Interannual and Interdecadal Variations of the East Asian Summer Monsoon and Tropical Pacific SSTs. Part I: Roles of the Subtropical Ridge. *J. Clim.*, **13**, 4310–4325, doi:10.1175/1520-0442(2000)013<4310:iaivot>2.0.co;2.
- Chen, D., and Coauthors, 2015a: Strong influence of westerly wind bursts on El Niño diversity. *Nat. Geosci.*, **8**, 339, doi:10.1038/ngeo2399. <http://dx.doi.org/10.1038/ngeo2399>.
- Chen, L., T. Li, and Y. Yu, 2015b: Causes of Strengthening and Weakening of ENSO Amplitude under Global Warming in Four CMIP5 Models*. *J. Clim.*, **28**, 3250–3274, doi:10.1175/jcli-d-14-00439.1.
- Chen, Z., Z. Wen, R. Wu, P. Zhao, and J. Cao, 2013: Influence of two types of El Niños on the East Asian climate during boreal summer: a numerical study. *Clim. Dyn.*, **43**, 469–481, doi:10.1007/s00382-013-1943-1.

- Chou, C., J. D. Neelin, C. A. Chen, and J. Y. Tu, 2009: Evaluating the “rich-get-richer” mechanism in tropical precipitation change under global warming. *J. Clim.*, **22**, 1982–2005, doi:10.1175/2008JCLI2471.1.
- Christensen, J. H., and Coauthors, 2013: WG1, CH14: Climate Phenomena and their Relevance for Future Regional Climate Change Supplementary Material. *Clim. Chang. 2013 Phys. Sci. Basis. Contrib. Work. Gr. I to Fifth Assess. Rep. Intergov. Panel Clim. Chang.*, 62, doi:10.1017/CBO9781107415324.028. www.climatechange2013.org.
- Chung, P.-H., and T. Li, 2013: Interdecadal Relationship between the Mean State and El Niño Types*. *J. Clim.*, **26**, 361–379, doi:10.1175/jcli-d-12-00106.1.
- Collins, M., 2000: Understanding Uncertainties in the response of to Greenhouse Warming. *27*, 3509–3512.
- Collins, M., and Coauthors, 2010: The impact of global warming on the tropical Pacific Ocean and El Nino. *Nat. Geosci.*, **3**, 391–397, doi:10.1038/ngeo868.
- Dai, A., 2006: Precipitation Characteristics in Eighteen Coupled Climate Models. *J. Clim.*, **19**, 4605–4630, doi:10.1175/JCLI3884.1.
- Ding, Y., and C. J. C. L., 2005: The East Asian summer monsoon: an overview. *Meteorol. Atmos. Phys.*, **89**, 117–142, doi:10.1007/s00703-005-0125-z.
- Endo, H., and A. Kitoh, 2014: Thermodynamic and dynamic effects on regional monsoon rainfall changes in a warmer climate. *Geophys. Res. Lett.*, **41**, 1704–1711, doi:10.1002/2013GL059158.
- Feng, J., and J. Li, 2011: Influence of El Niño Modoki on spring rainfall over south China. *J. Geophys. Res.*, **116**, doi:10.1029/2010jd015160.
- , L. Wang, W. Chen, S. K. Fong, and K. C. Leong, 2010: Different impacts of two types of Pacific Ocean warming on Southeast Asian rainfall during boreal winter. *J. Geophys. Res.*, **115**, doi:10.1029/2010jd014761.

- , W. Chen, C. Y. Tam, and W. Zhou, 2011: Different impacts of El Niño and El Niño Modoki on China rainfall in the decaying phases. *Int. J. Climatol.*, **31**, 2091–2101, doi:10.1002/joc.2217.
- , L. Wang, and W. Chen, 2014: How does the east asian summer monsoon behave in the decaying phase of El Niño during different PDO phases. *J. Clim.*, **27**, 2682–2698, doi:10.1175/JCLI-D-13-00015.1.
- , W. Chen, H. Gong, J. Ying, and W. Jiang, 2018: An investigation of CMIP5 model biases in simulating the impacts of central Pacific El Niño on the East Asian summer monsoon. *Clim. Dyn.*, **0**, 1–16, doi:10.1007/s00382-018-4284-2.
- Ferrett, S., and M. Collins, 2019: ENSO feedbacks and their relationships with the mean state in a flux adjusted ensemble. *Clim. Dyn.*, **52**, 7189–7208, doi:10.1007/s00382-016-3270-9.
- , —, and H. L. Ren, 2017: Understanding bias in the evaporative damping of El Niño-Southern Oscillation events in CMIP5 models. *J. Clim.*, **30**, 6351–6370, doi:10.1175/JCLI-D-16-0748.1.
- Flato, G., and Coauthors, 2013: Evaluation of Climate Models. *Clim. Chang. 2013 Phys. Sci. Basis. Contrib. Work. Gr. I to Fifth Assess. Rep. Intergov. Panel Clim. Chang.*, 741–866, doi:10.1017/CBO9781107415324.
- Gastineau, G., and B. J. Soden, 2009: Model projected changes of extreme wind events in response to global warming. *Geophys. Res. Lett.*, **36**, 1–5, doi:10.1029/2009GL037500.
- Gong, H., L. Wang, W. Chen, D. Nath, G. Huang, and W. Tao, 2015: Diverse Influences of ENSO on the East Asian–Western Pacific Winter Climate Tied to Different ENSO Properties in CMIP5 Models. *J. Clim.*, **28**, 2187–2202, doi:10.1175/jcli-d-14-00405.1.
- Guilyardi, E., H. Bellenger, M. Collins, S. Ferrett, W. Cai, and A. Wittenberg, 2012: A first look at ENSO in CMIP5. *CLIVAR Exch.*, **17**, 29–32.

- Ha, K. J., K. Y. Heo, S. S. Lee, K. S. Yun, and J. G. Jhun, 2012: Variability in the East Asian Monsoon: A review. *Meteorol. Appl.*, **19**, 200–215, doi:10.1002/met.1320.
- Ham, Y.-G., and J.-S. Kug, 2011: How well do current climate models simulate two types of El Niño? *Clim. Dyn.*, **39**, 383–398, doi:10.1007/s00382-011-1157-3.
- Hawkins, E., and R. Sutton, 2009: The Potential to Narrow Uncertainty in Regional Climate Predictions. *Bull. Am. Meteorol. Soc.*, **90**, 1095–1108, doi:10.1175/2009bams2607.1.
- He, C., T. Zhou, A. Lin, B. Wu, D. Gu, C. Li, and B. Zheng, 2015: Enhanced or Weakened Western North Pacific Subtropical High under Global Warming? *Sci Rep.*, **5**, 16771, doi:10.1038/srep16771.
- Held, I. M., and B. J. Soden, 2006: Robust responses of the hydrologic cycle to global warming. *J. Clim.*, **19**, 5686–5699, doi:10.1175/JCLI3990.1.
<http://dx.doi.org/10.1175/JCLI3990.1>.
- Hsu, P. C., T. Li, J. J. Luo, H. Murakami, A. Kitoh, and M. Zhao, 2012: Increase of global monsoon area and precipitation under global warming: A robust signal? *Geophys. Res. Lett.*, **39**, 2–7, doi:10.1029/2012GL051037.
- , —, H. Murakami, and A. Kitoh, 2013: Future change of the global monsoon revealed from 19 CMIP5 models. *J. Geophys. Res. Atmos.*, **118**, 1247–1260, doi:10.1002/jgrd.50145.
- Hu, X., S. Yang, and M. Cai, 2016: Contrasting the eastern Pacific El Niño and the central Pacific El Niño: process-based feedback attribution. *Clim. Dyn.*, **47**, 2413–2424, doi:10.1007/s00382-015-2971-9.
- Huang, P., and S.-P. Xie, 2015: Mechanisms of change in ENSO-induced tropical Pacific rainfall variability in a warming climate. *Nat. Geosci.*, **advance** on, doi:10.1038/ngeo2571

<http://www.nature.com/ngeo/journal/vaop/ncurrent/abs/ngeo2571.html#supplementary-information>.

Huffman, G. J., R. F. Adler, D. T. Bolvin, and G. Gu, 2009: Improving the global precipitation record: GPCP Version 2.1. *Geophys. Res. Lett.*, **36**, 1–5, doi:10.1029/2009GL040000.

Intergovernmental Panel on Climate Change, 2014: *Climate Change 2013 – The Physical Science Basis: Working Group I Contribution to the Fifth Assessment Report of the Intergovernmental Panel on Climate Change*. Cambridge University Press, Cambridge, <https://www.cambridge.org/core/books/climate-change-2013-the-physical-science-basis/BE9453E500DEF3640B383BADDCC332C3E>.

Jiang, W., G. Huang, K. Hu, R. Wu, H. Gong, X. Chen, and W. Tao, 2017: Diverse relationship between ENSO and the northwest pacific summer climate among CMIP5 models: Dependence on the enso decay pace. *J. Clim.*, **30**, 109–127, doi:10.1175/JCLI-D-16-0365.1.

Jin, F.-F., S. T. Kim, and L. Bejarano, 2006: A coupled-stability index for ENSO. *Geophys. Res. Lett.*, **33**, L23708, doi:10.1029/2006GL027221. <http://dx.doi.org/10.1029/2006GL027221>.

Kalnay, E., and Coauthors, 1996: The NCEP/NCAR 40-Year Reanalysis Project. *Bull. Am. Meteorol. Soc.*, **77**, 437–471, doi:10.1175/1520-0477(1996)077<0437:TNYRP>2.0.CO;2.

Kao, H.-Y., and J.-Y. Yu, 2009: Contrasting eastern-Pacific and central-Pacific types of ENSO. *J. Clim.*, **22**, 615–632, doi:10.1175/2008jcli2309.1.

Kim, S., H. Y. Son, and J. S. Kug, 2017: How well do climate models simulate atmospheric teleconnctions over the North Pacific and East Asia associated with ENSO? *Clim. Dyn.*, **48**, 971–985, doi:10.1007/s00382-016-3121-8.

- Kim, S. T., and J.-Y. Yu, 2012: The two types of ENSO in CMIP5 models. *Geophys. Res. Lett.*, **39**, doi:10.1029/2012gl052006.
- Kitoh, A., 2016: The Asian Monsoon and its Future Change in Climate Models: A Review. *J. Meteorol. Soc. Japan. Ser. II*, **95**, 7–33, doi:10.2151/jmsj.2017-002.
- Kug, J.-S., F.-F. Jin, and S.-I. An, 2009: Two types of El Niño events: Cold Tongue El Niño and Warm Pool El Niño. *J. Clim.*, **22**, 1499–1515, doi:10.1175/2008jcli2624.1.
- , S.-I. An, Y.-G. Ham, and I.-S. Kang, 2010: Changes in El Niño and La Niña teleconnections over North Pacific–America in the global warming simulations. *Theor. Appl. Climatol.*, **100**, 275–282, doi:10.1007/s00704-009-0183-0.
- , Y.-G. Ham, J.-Y. Lee, and F.-F. Jin, 2012: Corrigendum: Improved simulation of two types of El Niño in CMIP5 models. *Environ. Res. Lett.*, **7**, 39502, doi:10.1088/1748-9326/7/3/039502.
- Kug, J. S., and Y. G. Ham, 2011: Are there two types of la Nina? *Geophys. Res. Lett.*, **38**, 2–7, doi:10.1029/2011GL048237.
- Kumar, K. K., B. Rajagopalan, M. Hoerling, G. Bates, and M. Cane, 2006: Unraveling the mystery of Indian Monsoon failure during El Niño. *Science (80-.)*, **314**, 115–119, doi:10.1126/science.1131152.
- Lau, N.-C., and M. J. Nath, 2003: Atmosphere–Ocean variations in the Indo-Pacific sector during ENSO episodes. *J. Clim.*, **16**, 3–20, doi:10.1175/1520-0442(2003)016<0003:AOVITI>2.0.CO;2.
- Lee, J.-Y., and B. Wang, 2012: Future change of global monsoon in the CMIP5. *Clim. Dyn.*, doi:10.1007/s00382-012-1564-0.
- Li, G., and S.-P. Xie, 2012: Origins of tropical-wide SST biases in CMIP multi-model ensembles. *Geophys. Res. Lett.*, **39**, n/a-n/a, doi:10.1029/2012gl053777.

- , and S. P. Xie, 2014: Tropical biases in CMIP5 multimodel ensemble: The excessive equatorial pacific cold tongue and double ITCZ problems. *J. Clim.*, **27**, 1765–1780, doi:10.1175/JCLI-D-13-00337.1.
- , and Coauthors, 2019: Effect of excessive equatorial Pacific cold tongue bias on the El Niño-Northwest Pacific summer monsoon relationship in CMIP5 multi-model ensemble. *Clim. Dyn.*, **52**, 6195–6212, doi:10.1007/s00382-018-4504-9.
- Li, X., and M. Ting, 2015: Recent and future changes in the Asian monsoon-ENSO relationship: Natural or forced? *Geophys. Res. Lett.*, **42**, 3502–3512, doi:10.1002/2015GL063557.
- Lian, T., D. Chen, Y. Tang, and Q. Wu, 2014: Effects of westerly wind bursts on El Niño: A new perspective. *Geophys. Res. Lett.*, **41**, 3522–3527, doi:10.1002/2014GL059989.
- Lloyd, J., E. Guilyardi, H. Weller, and J. Slingo, 2009: The role of atmosphere feedbacks during ENSO in the CMIP3 models. *Atmos. Sci. Lett.*, **10**, 170–176, doi:10.1002/asl.227.
- Meehl, G. A., J. M. Arblaster, J. M. Caron, H. Annamalai, M. Jochum, A. Chakraborty, and R. Murtugudde, 2012: Monsoon regimes and processes in CCSM4. Part I: The Asian-Australian monsoon. *J. Clim.*, **25**, 2583–2608, doi:10.1175/JCLI-D-11-00184.1.
- Mitchell, J. F. B., C. A. Wilson, and W. M. Cunningham, 1987: On CO₂ climate sensitivity and model dependence of results. *Q. J. R. Meteorol. Soc.*, **113**, 293–322, doi:10.1002/qj.49711347517.
- Neale, R. B., and Coauthors, 2010: Description of the NCAR Community Atmosphere Model (CAM 4.0). *Ncar/Tn-464+Str*, 214.
- Nitta, T., 1987: Convective Activities in the Tropical Western Pacific and Their Impact on the Northern Hemisphere Summer Circulation. *J. Meteorol. Soc. Japan. Ser. II*, **65**, 373–390, doi:10.2151/jmsj1965.65.3_373.

- Perry, S. J., S. McGregor, A. Sen Gupta, and M. H. England, 2017: Future Changes to El Niño–Southern Oscillation Temperature and Precipitation Teleconnections. *Geophys. Res. Lett.*, **44**, 10,608–610,616, doi:10.1002/2017GL074509.
- Philip, S. Y., and G. J. van Oldenborgh, 2006: Shifts in ENSO coupling processes under global warming. *Geophys. Res. Lett.*, **33**, 1–5, doi:10.1029/2006GL026196.
- Power, S., F. Delage, C. Chung, G. Kociuba, and K. Keay, 2013: Robust twenty-first-century projections of El Niño and related precipitation variability. *Nature*, **502**, 541–545, doi:10.1038/nature12580.
- Power, S. B., and F. P. D. Delage, 2018: El Niño–Southern Oscillation and Associated Climatic Conditions around the World during the Latter Half of the Twenty-First Century. *J. Clim.*, **31**, 6189–6207, doi:10.1175/JCLI-D-18-0138.1.
- Rasmusson, E. M., and T. H. Carpenter, 1982: Variations in tropical sea surface temperature and surface wind fields associated with the Southern Oscillation/El Niño. *Mon. Weather Rev.*, **110**, 354–384, doi:10.1175/1520-0493(1982)110<0354:vtsst>2.0.co;2.
- Rayner, N. A., D. E. Parker, E. B. Horton, C. K. Folland, L. V Alexander, D. P. Rowell, E. C. Kent, and A. Kaplan, 2003: Global analyses of sea surface temperature, sea ice, and night marine air temperature since the late nineteenth century. *J. Geophys. Res.*, **108**, doi:10.1029/2002jd002670.
- Roy, I., R. G. Tedeschi, and M. Collins, 2017: ENSO teleconnections to the Indian summer monsoon in observations and models. *Int. J. Climatol.*, **37**, 1794–1813, doi:10.1002/joc.4811.
- Samanta, D., K. B. Karanauskas, N. F. Goodkin, S. Coats, J. E. Smerdon, and L. Zhang, 2018: Coupled Model Biases Breed Spurious Low-Frequency Variability in the Tropical Pacific Ocean. *Geophys. Res. Lett.*, **45**, 10,609–10,618, doi:10.1029/2018GL079455.

- Santoso, A., S. McGregor, F. F. Jin, W. Cai, M. H. England, S. Il An, M. J. McPhaden, and E. Guilyardi, 2013: Late-twentieth-century emergence of the El Niño propagation asymmetry and future projections. *Nature*, **504**, 126–130, doi:10.1038/nature12683.
- Seager, R., N. Naik, and G. A. Vecchi, 2010: Thermodynamic and dynamic mechanisms for large-scale changes in the hydrological cycle in response to global warming. *J. Clim.*, **23**, 4651–4668, doi:10.1175/2010JCLI3655.1.
- Silverman, B. W., 1986: *Density estimation for statistics and data analysis*. London: Chapman and Hall, London,
- Sohn, S.-J., C.-Y. Tam, and H.-I. Jeong, 2016: How do the strength and type of ENSO affect SST predictability in coupled models. *Sci Rep*, **6**, 33790, doi:10.1038/srep33790.
- Song, F., and T. Zhou, 2013: Interannual Variability of East Asian Summer Monsoon Simulated by CMIP3 and CMIP5 AGCMs: Skill Dependence on Indian Ocean–Western Pacific Anticyclone Teleconnection. *J. Clim.*, **27**, 1679–1697, doi:10.1175/JCLI-D-13-00248.1. <https://doi.org/10.1175/JCLI-D-13-00248.1>.
- , and —, 2014: The Climatology and Interannual Variability of East Asian Summer Monsoon in CMIP5 Coupled Models: Does Air–Sea Coupling Improve the Simulations? *J. Clim.*, **27**, 8761–8777, doi:10.1175/JCLI-D-14-00396.1. <https://doi.org/10.1175/JCLI-D-14-00396.1>.
- Sperber, K. R., H. Annamalai, I.-S. Kang, A. Kitoh, A. Moise, A. Turner, B. Wang, and T. Zhou, 2013: The Asian summer monsoon: an intercomparison of CMIP5 vs. CMIP3 simulations of the late 20th century. *Clim. Dyn.*, **41**, 2711–2744, doi:10.1007/s00382-012-1607-6.
- Stevenson, S., B. Fox-Kemper, and M. Jochum, 2012: Understanding the ENSO-CO₂ link using stabilized climate simulations. *J. Clim.*, **25**, 7917–7936, doi:10.1175/JCLI-D-11-00546.1.

- Stevenson, S. L., 2012: Significant changes to ENSO strength and impacts in the twenty-first century: Results from CMIP5. *Geophys. Res. Lett.*, **39**, 1–5, doi:10.1029/2012GL052759.
- Tan, W., X. Wang, W. Wang, C. Wang, and J. Zuo, 2016: Different Responses of Sea Surface Temperature in the South China Sea to Various El Niño Events during Boreal Autumn. *J. Clim.*, **29**, 1127–1142, doi:10.1175/jcli-d-15-0338.1. <http://journals.ametsoc.org/doi/abs/10.1175/JCLI-D-15-0338.1>.
- Taschetto, A. S., A. Sen Gupta, N. C. Jourdain, A. Santoso, C. C. Ummenhofer, and M. H. England, 2014: Cold tongue and warm pool ENSO Events in CMIP5: Mean state and future projections. *J. Clim.*, **27**, 2861–2885, doi:10.1175/JCLI-D-13-00437.1.
- Taylor, K. E., 2001a: Summarizing multiple aspects of model performance in a single diagram. *J. Geophys. Res.*, **106**, 7183–7192, doi:10.1029/2000JD900719.
- , 2001b: Summarizing multiple aspects of model performance in a single diagram. *J. Geophys. Res. Atmos.*, **106**, 7183–7192, doi:10.1029/2000JD900719.
- , R. J. Stouffer, and G. A. Meehl, 2012: An overview of CMIP5 and the experiment design. *Bull. Am. Meteorol. Soc.*, **93**, 485–498, doi:10.1175/bams-d-11-00094.1.
- Tedeschi, R. G., and M. Collins, 2016: The influence of ENSO on South American precipitation during austral summer and autumn in observations and models. *Int. J. Climatol.*, **36**, 618–635, doi:10.1002/joc.4371.
- , and —, 2017: The influence of ENSO on South American precipitation: simulation and projection in CMIP5 models. *Int. J. Climatol.*, **37**, 3319–3339, doi:10.1002/joc.4919.
- Timmerman, A., J. Oberhuber, A. Blacher, M. Esch, M. Latif, and E. Roeckner, 1999: Increased El Niño frequency in a climate model forced by future greenhouse warming. *Nature*, **398**, 1996–1999.

- Timmermann, A., and Coauthors, 2018: El Niño–Southern Oscillation complexity. *Nature*, **559**, 535–545, doi:10.1038/s41586-018-0252-6. <http://dx.doi.org/10.1038/s41586-018-0252-6>.
- Todd, A., M. Collins, F. H. Lambert, and R. Chadwick, 2017: Diagnosing ENSO and Global Warming Tropical Precipitation Shifts Using Surface Relative Humidity and Temperature. *J. Clim.*, **31**, 1413–1433, doi:10.1175/JCLI-D-17-0354.1.
- , —, F. H. Lambert, and R. Chadwick, 2018: Diagnosing ENSO and global warming tropical precipitation shifts using surface relative humidity and temperature. *J. Clim.*, **31**, 1413–1433, doi:10.1175/JCLI-D-17-0354.1.
- Trenberth, K. E., and D. P. Stepaniak, 2001: Indices of El Niño Evolution. *J. Clim.*, **14**, 1697–1701, doi:10.1175/1520-0442(2001)014<1697:lioeno>2.0.co;2.
- Turner, A. G., and H. Annamalai, 2012: Climate change and the South Asian summer monsoon. *Nat. Clim. Chang.*, **2**, 587–595. <http://dx.doi.org/10.1038/nclimate1495>.
- Ueda, H., A. Iwai, K. Kuwako, and M. E. Hori, 2006: Impact of anthropogenic forcing on the Asian summer monsoon as simulated by eight GCMs. *Geophys. Res. Lett.*, **33**, 20–23, doi:10.1029/2005GL025336.
- Vecchi, G. A., and B. J. Soden, 2007: Global warming and the weakening of the tropical circulation. *J. Clim.*, **20**, 4316–4340, doi:10.1175/JCLI4258.1.
- Vecchi, G. A., and A. T. Wittenberg, 2010: El Niño and our future climate: where do we stand? *Wiley Interdiscip. Rev. Clim. Chang.*, **1**, 260–270, doi:10.1002/wcc.33. <http://dx.doi.org/10.1002/wcc.33>.
- Wang, B., and Z. Fan, 1999: Choice of South Asian Summer Monsoon Indices. *Bull. Am. Meteorol. Soc.*, **80**, 629–638, doi:10.1175/1520-0477(1999)080<0629:cosasm>2.0.co;2.

- , R. Wu, and X. Fu, 2000: Pacific-East Asian teleconnection: How does ENSO affect East Asian climate? *J. Clim.*, **13**, 1517–1536, doi:10.1175/1520-0442(2000)013<1517:PEATHD>2.0.CO;2.
- , —, and K.-M. Lau, 2001: Interannual Variability of the Asian Summer Monsoon: Contrasts between the Indian and the Western North Pacific–East Asian Monsoons. *J. Clim.*, **14**, 4073–4090, doi:10.1175/1520-0442(2001)014<4073:IVOTAS>2.0.CO;2. <http://journals.ametsoc.org/doi/abs/10.1175/1520-0442%282001%29014%3C4073%3AIVOTAS%3E2.0.CO%3B2>.
- , Z. Wu, J. Li, J. Liu, C.-P. Chang, Y. Ding, and G. Wu, 2008: How to Measure the Strength of the East Asian Summer Monsoon. *J. Clim.*, **21**, 4449–4463, doi:10.1175/2008jcli2183.1.
- , S. Y. Yim, J. Y. Lee, J. Liu, and K. J. Ha, 2014: Future change of Asian-Australian monsoon under RCP 4.5 anthropogenic warming scenario. *Clim. Dyn.*, **42**, 83–100, doi:10.1007/s00382-013-1769-x.
- Wang, C., 2018: A review of ENSO theories. *Natl. Sci. Rev.*, **5**, 813–825, doi:10.1093/nsr/nwy104.
- , C. Deser, J.-Y. Yu, P. DiNezio, and A. Clement, 2017a: El Niño and Southern Oscillation (ENSO): A Review. *Coral Reefs of the Eastern Tropical Pacific: Persistence and Loss in a Dynamic Environment*, P.W. Glynn, D.P. Manzello, and I.C. Enochs, Eds., Springer Netherlands, Dordrecht, 85–106.
- Wang, Z., G. Li, and S. Yang, 2017b: Origin of Indian summer monsoon rainfall biases in CMIP5 multimodel ensemble. *Clim. Dyn.*, **0**, 0, doi:10.1007/s00382-017-3953-x.
- Watanabe, M., Y. Kamae, and M. Kimoto, 2014a: Robust increase of the equatorial Pacific rainfall and its variability in a warmed climate. *Geophys. Res. Lett.*, **41**, 3227–3232, doi:10.1002/2014gl059692.

- , H. Shiogama, H. Tatebe, M. Hayashi, M. Ishii, and M. Kimoto, 2014b: Contribution of natural decadal variability to global warming acceleration and hiatus. *Nat. Clim. Chang.*, **4**, 893–897, doi:10.1038/nclimate2355.
- Webster, P. J., V. O. Magaña, T. N. Palmer, J. Shukla, R. A. Tomas, M. Yanai, and T. Yasunari, 1998: Monsoons: Processes, predictability, and the prospects for prediction. *J. Geophys. Res. Ocean.*, **103**, 14451–14510, doi:10.1029/97JC02719.
- Weng, H., S. K. Behera, and T. Yamagata, 2009: Anomalous winter climate conditions in the Pacific rim during recent El Niño Modoki and El Niño events. *Clim. Dyn.*, **32**, 663–674, doi:10.1007/s00382-008-0394-6.
- Wittenberg, A. T., A. Rosati, N. C. Lau, and J. J. Poshay, 2006: GFDL's CM2 global coupled climate models. Part III: Tropical Pacific climate and ENSO. *J. Clim.*, **19**, 698–722, doi:10.1175/JCLI3631.1.
- Wu, B., and T. Zhou, 2016: Relationships between ENSO and the East Asian–western North Pacific monsoon: observations versus 18 CMIP5 models. *Clim. Dyn.*, **46**, 729–743, doi:10.1007/s00382-015-2609-y.
- Wu, R., and B. Wang, 2000: Interannual variability of summer monsoon onset over the Western North Pacific and the underlying processes. *J. Clim.*, **13**, 2483–2501, doi:10.1175/1520-0442(2000)013<2483:ivosmo>2.0.co;2.
- , Z.-Z. Hu, and B. P. Kirtman, 2003: Evolution of ENSO-related rainfall anomalies in East Asia. *J. Clim.*, **16**, 3742–3758, doi:10.1175/1520-0442(2003)016<3742:EOERAI>2.0.CO;2.
- Xie, R., and F. F. Jin, 2018: Two leading ENSO modes and El Niño types in the Zebiak-Cane model. *J. Clim.*, **31**, 1943–1962, doi:10.1175/JCLI-D-17-0469.1.

- Xie, S.-P., K. Hu, J. Hafner, H. Tokinaga, Y. Du, G. Huang, and T. Sampe, 2009: Indian Ocean Capacitor Effect on Indo–Western Pacific Climate during the Summer following El Niño. *J. Clim.*, **22**, 730–747, doi:10.1175/2008jcli2544.1.
- , C. Deser, G. A. Vecchi, J. Ma, H. Teng, and A. T. Wittenberg, 2010: Global Warming Pattern Formation: Sea Surface Temperature and Rainfall*. *J. Clim.*, **23**, 966–986, doi:10.1175/2009JCLI3329.1. <http://dx.doi.org/10.1175/2009JCLI3329.1>.
- Xie, S. P., and Coauthors, 2015: Towards predictive understanding of regional climate change. *Nat. Clim. Chang.*, **5**, 921–930, doi:10.1038/nclimate2689. <http://dx.doi.org/10.1038/nclimate2689>.
- Xu, K., C. Zhu, and J. He, 2013: Two Types of El Niño-related Southern Oscillation and Their Different Impacts on Global Land Precipitation. *Adv. Atmos. Sci.*, **30**, 1743–1757, doi:10.1007/s00376-013-2272-3.
- , J. Su, and C. Zhu, 2014: The natural oscillation of two types of ENSO events based on analyses of CMIP5 model control runs. *Adv. Atmos. Sci.*, **31**, 801–813, doi:10.1007/s00376-013-3153-5.
- , C.-Y. Tam, C. Zhu, B. Liu, and W. Wang, 2017: CMIP5 Projections of Two Types of El Niño and Their Related Tropical Precipitation in the Twenty-First Century. *J. Clim.*, **30**, 849–864, doi:10.1175/jcli-d-16-0413.1.
- , Q. L. Huang, C. Y. Tam, W. Wang, S. Chen, and C. Zhu, 2018: Roles of tropical SST patterns during two types of ENSO in modulating wintertime rainfall over southern China. *Clim. Dyn.*, **0**, 1–16, doi:10.1007/s00382-018-4170-y.
- Yang, S., Z. Li, J. Yu, X. Hu, W. Dong, S. He, N. D. Studies, and S. Yat-sen, 2018: El Niño–Southern Oscillation and Its Impact in the Changing Climate. doi:10.1093/nsr/nwy046/4975301.

- Yeh, S.-W., and Coauthors, 2018: ENSO atmospheric teleconnections and their response to greenhouse gas forcing. *Rev. Geophys.*, doi:10.1002/2017RG000568.
- Yu, J.-Y., and S. T. Kim, 2010a: Identification of Central-Pacific and Eastern-Pacific types of ENSO in CMIP3 models. *Geophys. Res. Lett.*, **37**, doi:10.1029/2010gl044082.
- , and —, 2010b: Three evolution patterns of Central-Pacific El Niño. *Geophys. Res. Lett.*, **37**, doi:10.1029/2010gl042810.
- , and —, 2011: Relationships between Extratropical Sea Level Pressure Variations and the Central Pacific and Eastern Pacific Types of ENSO. *J. Clim.*, **24**, 708–720, doi:10.1175/2010jcli3688.1.
- , and —, 2013: Identifying the types of major El Niño events since 1870. *Int. J. Climatol.*, **33**, 2105–2112, doi:10.1002/joc.3575. <http://dx.doi.org/10.1002/joc.3575>.
- , H.-Y. Kao, and T. Lee, 2010: Subtropics-Related Interannual Sea Surface Temperature Variability in the Central Equatorial Pacific. *J. Clim.*, **23**, 2869–2884, doi:10.1175/2010jcli3171.1.
- , Y. Zou, S. T. Kim, and T. Lee, 2012: The changing impact of El Niño on US winter temperatures. *Geophys. Res. Lett.*, **39**, doi:10.1029/2012gl052483.
- , P. Kao, H. Paek, H.-H. Hsu, C. Hung, M.-M. Lu, and S.-I. An, 2015: Linking Emergence of the Central Pacific El Niño to the Atlantic Multidecadal Oscillation. *J. Clim.*, **28**, 651–662, doi:10.1175/jcli-d-14-00347.1.
- Yuan, Y., and S. Yang, 2012: Impacts of Different Types of El Niño on the East Asian Climate: Focus on ENSO Cycles. *J. Clim.*, **25**, 7702–7722, doi:10.1175/JCLI-D-11-00576.1.
- Zhang, G. J., and N. A. McFarlane, 1995: Sensitivity of climate simulations to the parameterization of cumulus convection in the canadian climate centre general circulation model. *Atmos. - Ocean*, **33**, 407–446, doi:10.1080/07055900.1995.9649539.

- Zhang, W., F.-F. Jin, J. Li, and H.-L. Ren, 2011: Contrasting Impacts of Two-Type El Niño over the Western North Pacific during Boreal Autumn. *J. Meteorol. Soc. Japan*, **89**, 563–569, doi:10.2151/jmsj.2011-510.
- Zheng, F., X.-H. Fang, J.-Y. Yu, and J. Zhu, 2014: Asymmetry of the Bjerknes Positive Feedback between the Two Types of El Niño. *Geophys. Res. Lett.*, 2014GL062125, doi:10.1002/2014GL062125.
- Zheng, Y., J. L. Lin, and T. Shinoda, 2012: The equatorial Pacific cold tongue simulated by IPCC AR4 coupled GCMs: Upper ocean heat budget and feedback analysis. *J. Geophys. Res. Ocean.*, **117**, doi:10.1029/2011JC007746.
- Zhou, Z. Q., S. P. Xie, X. T. Zheng, Q. Liu, and H. Wang, 2014: Global warming-induced changes in El Niño teleconnections over the North Pacific and North America. *J. Clim.*, **27**, 9050–9064, doi:10.1175/JCLI-D-14-00254.1.